UNIVERSITÀ DEGLI STUDI DI GENOVA

ELECTROMAGNETIC MODELING FOR THE DEVELOPMENT AND OPTIMIZATION OF DIFFERENT DEVICES TO SUPPORT BONE REGENERATION

A thesis submitted in fulfillment of the requirements for the degree of Doctorate of Philosophy

in

Science and Technologies for Electronic and Telecommunication Engineering, and Naval Architecture

By
Dr. Reem Hanna

2019

Supervisors

Prof. Stefano Benedicenti

Prof. Mirco Raffetto

Prof.ac. Andrea Amaroli

PhD Programme Chair: *Prof. Mario Marchese*

“ Never stop learning, life never stops teaching”

Michael Josephson

“ Learn as if you were to live forever”

Mahatma Gandhi

ABSTRACT

Tissue healing is in general a complex process, which involves both local and systemic responses, and bone regeneration in particular is much slower than repair in any other human tissue. Thus, it exhibits a great challenge in clinical practice and in the field of research. Bone regeneration is comprised of a series of biological events, involving a number of cell types and intracellular and extracellular molecular-signaling pathways, with a definable temporal and spatial sequence, in an effort to optimize the skeletal repair and restore its functionality.

Photobiomodulation (PBM) therapy has been shown to be effective in modulating both local and systemic responses, by enhancing cellular activities resulting in an increase in function, especially in injured tissues, leading to optimization of tissue repair and regeneration. In bone tissue, application of the photonic energy leads to bone healing by the activation of osteoblasts, leading to proliferation and differentiation, as well as osteoclast inhibition and, consequently, neoformation of bone matrix. The process of the *in vitro* pre-osteoblasts maturation, mimicking their *in vivo* behavior, passes through three distinct stages of development: proliferation, early differentiation (maturation) and late differentiation (mineralization).

Despite the extensive research on the effects of photobiomodulation (PBM) light on bone regeneration, the current outcomes ranging from positive to negative effect remain controversial. These contradictory data are thought to be due to; incomplete knowledge and understanding of the mechanistic effects of laser light on cells, lack of standardized laser dosimetry, inefficient laser beam profile, improper study design and varied methods of investigation. The literature is hindered by a considerable heterogeneity of the irradiation parameters of PBM, as well as, the methods

utilized to evaluate the results and the type of osteoblast-like cells irradiated. This has led to a need of standardization. Moreover, heterogeneity of the current studies and their limitations could be due to study designs and inefficient beam profile, resulting in undesirable effects and accounting for negative and inconclusive outcomes. Ultimately, lack of intimate knowledge and understanding of the PBM light behavior impinging on the target tissue, as well as the optical tissue properties, can compromise optimization of the therapeutic outcomes. Thus, an evidence-based decision for definite therapeutic application of PBM in bone regeneration is required.

In this thesis, we addressed the above issues and challenges via two elements, the electromagnetic (EM) modeling experiments and the molecular and cellular impact of PBM on bone regeneration (*In vitro* studies).

The Electromagnetic models

In my PhD proposal, I intended to both create an EM model, for the first time, and examine the mechanism of interaction of the electromagnetic fields (EMFs) with cells/tissues and establish the link that can be utilized in my cellular experiments. As the project evolved, it became clear this work was breaking new grounds and was significantly more complex than initially envisaged. As it is a small part of a much larger exciting project undertaken by University of Genoa, it has meant that I need to coordinate my work with the overall timetable of this larger project. As a result, I decided to defer, the interaction of the EMF with cells of interest part, to my Post Doctorate study. We developed, for the first time, a set of simple models to examine the behavior of the local electromagnetic field (EMF), determining the PBM effects on mitochondria. This set of models was tested and crosschecked for its validity by

evaluating various variables in terms of, polarization, absorption and scattering coefficient, dissipated energy density and irradiance, as well as the refractive index. Ultimately, our model and preliminary data would be the first stepping-stone for further experiments, in order to understand the mechanism of interaction between electromagnetic fields and cells or tissues.

Our conclusions showed that when these set of models are utilized, for the phenomenon of interest, the incident field polarization had small effects on the electromagnetic field and negligible consequences on the average energy, as well as, on the dissipated power densities. The same was shown to hold true for different orientations that the mitochondria can assume.

The analogous conclusions were obtained by taking into account the possible changes in the dimensions or of the real part of the refractive index of the considered organelles. The variations of the absorption coefficient were shown to have significant effects on the average dissipated power density in the mitochondria but these effects can be predicted in a surprisingly simple way.

It was proved that the numerical analysis, of the problems of interest, could be computed by using three-dimensional models, involving only a few mitochondria in the plane, which was transverse to the direction of propagation of the illuminating light that generated a uniform distribution of the energy over $1cm^2$ area. The one-dimensional models provided significant information on the EMF, utilized to stimulate the mitochondria. Mitochondria behaved like weak scatterers. Therefore, it was not necessary to analyze large extension of such organelles to understand what happen inside one of them.

The molecular and cellular impact of 980nm PBM on osteoblast maturation: in vitro studies

Our pilot study data, on the bone marrow stromal cells (BMSCs), strongly suggested that the high fluence concept (over 60J/cm^2 in continuous emission mode (CW)) delivered by flattop beam profile device (FT) can promote BMSCs differentiation towards osteogenesis. Moreover, the results showed an increase in cytokines synthesis with potent anti-inflammatory properties and a decrease in the release of proinflammatory mediators. This provided me with a platform, demonstrating the validity of high fluence in facilitating osteoblasts differentiation through BMSCs. Based on this, I formulated three PBM protocols for 980nm to be tested on pre-osteoblast cell line in my definitive *in vitro* studies. The first phase of *in vitro* studies aimed to evaluate the 980nm bio-stimulatory effects on osteoblasts maturation, optimise the PBM effects on bone healing with various beam profiles delivery devices, and establish protocol/protocols of 980nm PBM in bone regeneration. The primary objective was to determine the optimal 980nm dosimetry, which exerts bio-stimulatory effects to accelerate and enhance the bone regenerative process. The secondary objective was to evaluate the intra-cellular pathways of the photon-cell interaction across the metabolic proliferative and differentiation changes, which ultimately lead to bone healing and repair. The results of this study validated the contribution of PBM in bone regeneration and elucidated the biochemical effects at a cellular level. Moreover, the role of different dosages of 980nm PBM irradiation delivered by FT; in comparison to the Gaussian beam profiles (Standard (ST)) on bone regeneration were highlighted. The setup of the power outputs on the laser device was 1.1Watt (W) for the ST and 1W for the FT. However, the real (the threshold) power output reaching the target, measured by power meter, was as ~0.9 W,

(Irradiance ~ 0.9W/cm^2, Exposure time 60 seconds, energy ~55 J (Joule), fluence ~55 J/cm^2) delivered with the FT beam profile in CW in comparison to the ST, on MC3T3-E1 pre-osteoblast maturation. The protocol was based on 60 seconds exposure time for two consecutive weeks, which employed for all the groups.

The laser grouping and their associated irradiated energies were as follows:

Group 1- Irradiation once per week (Total enrgy 110J).

Group 2- Irradiaiton three times per week (Alternate day) (Total enrgy 330J).

Group 3 - irradiation five- times per week (Total energy 550 J).

The control cultures were processed in identical conditions except that the laser device was kept off all the time. The total energy was 0J.

The metabolic activity and the osteoblasts maturation were analyzed by alkaline phosphatase assay, alizarin red S histological staining, immunoblot and/or double immunolabeling analysis for Bcl2, Bax, Runx-2, Osx, Dlx5, osteocalcin, and collagen Type 1. Our data, for the first time, prove that laser irradiation of 980 nm wavelength with flattop beam profile delivery system, compared to standard-Gaussian profile, has improved photobiomodulatory efficacy on pre-osteoblastic cells differentiation. Mechanistically, the irradiation enhances the pre-osteoblast differentiation through activation of Wnt signaling as well as the Smads 2/3-βcatenin pathway.

Our results indicated and valued the intra-cellular pathways of the photon-cell interaction across the metabolic, proliferative and differentiation changes in the cells. Additionally, our data showed that the cells irradiated THREE times a week (Total energy of 330 J) and ONCE a week (Total energy of 110 J) for two consecutive weeks protocols have increased the proliferation and differentiation of the osteoblasts in both ST & FT hand-pieces but the data showed increasingly statistical significant in the FT group. The only *Runx2* was detected when the cells were irradiated with the ST hand-

piece. Therefore, total energy of 110 J when either of the hand-pieces utilized, has influenced early differentiation markers. Interestingly, when the process was carried out, until the mineralization and maturation (Late osteogenesis), the ST hand-piece irradiation failed to induce an effective process, and did not lead to matrix deposition, while the FT profile showed a significant effect.

In conclusion, our data, for the first time, prove that laser irradiation of 980 nm wavelength with the FT beam profile delivery system in comparison to the ST profile has a great photobiomodulatory efficacy on pre-osteoblastic cells differentiation, which would assist in accelerating bone regeneration, due to its homogeneous energy distribution at each point of its cross-section. Moreover, the irradiation protocols of three times a week and once a week for two consecutive weeks were able to increase the pre-osteoblasts and osteoblasts transcription factors, which were strongly and statistically significantly increased when the FT hand-piece was utilized. Therefore, the 980 nm laser irradiation protocol was able to promote the MC3T3-E1 cell differentiation.

Researchers have demonstrated that the major barrier for an effective biological healing is insufficient laser photonic energy delivered to the injured site. PBM can modify the cell metabolism by increasing the mitochondria's ATP production. Currently, the challenge is to understand the target tissues optical properties and its cellular pathway when irradiated with laser phonic energy. In this way, modification of various energy exposure values can influence clinical outcomes predictability. Therefore, in the second phase of my *in vitro* study, we evaluated the effect of 980nm irradiation delivered with ST and FT beam profile hand-pieces on monolayer cell, at various power outputs; 0.8W, 0.5W and 0.25W. However, the exact power ouput values reaching the target, measured by power meter, were as follows: 0.75W, 0.45W,

and 0.20W respectively. The MC3T3-E1 cells irradiated for two consecutive weeks, according to the following protocols: once a week (Total energy 90, 54, 24 J), respectively); three times a week (total energy 270, 162, 72J, respectively); five times a week (total energy 450, 270, 120 J, respectively). Metabolic activity of viable cells evaluated as follows: Hoechst staining; Western blotting for Runx-2, Bcl2, Bax, Osx, Dlx5, β-catenin, Smads 2/3, TGFβ, p.PI3K, PI3K, p.AKt, AKt, and p.ERK.

Our data, for the first time, prove that the 980 nm irradiation at power output setting at 0.75W (0.75W/cm^2) for 60 seconds in CW stimulated the MC3T3-E1 pre-osteoblasts viability, by affecting the critical pre-survival markers such as p.PI3K, p.Akt, Bcl2 and Bclxl. Moreover, we concluded that 980nm PBM delivered with FT at 0.75W power output was comparable to results with the ST. However, 0.45W and 0.20W did not modulate the cell metabolic features. Additionally, none of the laser protocols delivered with FT or ST had any influence on the cell differentiation process.

In summary, our *in vitro* studies data, for the first time, have demonstrated the potential of utilizing the FT beam profile with our established protocols in bone regeneration, as a therapeutic tool for future pre-clinical and clinical applications. Moreover, these studies have shown the mechanistic effects of the PBM light on intracellular pathway across the metabolic and differentiation of the osteoblasts towards bone regeneration.

ACKNOWLEDGMENTS

I thoroughly enjoyed the three years journey of my doctorate at University of Genoa. There are so many eminent professors and colleagues who have made the three years of my doctorate journey possible. Without them, this thesis would not have been possible. I would like to thank you all.

First and foremost, I would like to express my most gratitude and appreciation to my valued Dean and supervisor, Professor Stefano Benedicenti, for his continuous support and direction, kind patience and inspirational encouragement, especially throughout the three years my doctorate journey. Without his help, supervision, and immense support, I doubt this research project would have got anywhere. Thank you so much for giving me the opportunity and trusting me, in such an interesting and phenomenal research project. It was an honor for me to undertake my doctorate research programme at Univerity of Genoa under Professor Benedicenti's leadership.

I would specially like to thank my esteemed Professor, Alberico Benedicenti, for his outstanding contributions in my research work. Professor Benedicenti is the "Founder of Photobiomodulation" in various disciplines of medicine, dentistry and veterinary medicine. His valued and exceptional researches in this field have setup the first stone for further developmental of laser therapy innovation to serve healthcare.

I am heartily grateful to Professor Andrea Amaroli, my supervisor and mentor, for his delication to my research porject, countless supervision and direction throughout my doctorate journey. His expertise has enriched my knowledge and enhanced my biological skills, in understanding the area of my interest in photobiomodulation. I am very appreciatative for his immense support during my research project and my

remarkable thesis. I strive to learn more from Prof. Amaroli and work with him for future reseaches.

Many thanks to Professor Mirco Raffetto, my supervisor, for his tremendous efforts and time, during my electromagnetic part of my reseach project. I am grateful for his valuable contribution, in the completion of my research project and dissertation. His mentoring is very much appreciated.

I cannot thank enough Professor Maria Giovanna Sabbieti and Professor Dimitrios Aga for their remarkable efforts and support during my research work. I appreciate your expertise in introducing me to new skills or ideas in molecular aspects of bone regeneration. I value your time and hard work with me to produce our data for the first time.

Also, many thanks to Prof. Fulvio Laus, Prof. Vincenzo Cuteri, and Professor Gianfranco Coletti, for their continuous support to my research development.

I would like to express my gratefulness to Professor Wayne Selting. Over the years, I have learned a lot from him and strive to learn more. I am very appreciative for his support and friendship.

A special thanks goes to my family. Words cannot express how grateful I am to my parents, who without them I wouldn't have made it to where I am. I cannot thank you enough for your unconditional love, support, and care you have always cherished me with. I would like to delicate this thesis to them.

Thank you God for being with me in every step I have undertaken in my life and career. I am very grateful for all the blessings that you have showered me with.

INDEX **PAGE**

LIST OF FIGURES

CHAPTER I

CHAPTER II

CHAPTER V: PART I

LIST OF TABLES

CHAPTER III

CHAPTER V: PART II, PHASE I

LIST OF ABREVIATIONS AND SYMBOLS

ABBREVIATIONS

ADSC: Adipose-derived stem cells.

α-SMA: Alpha smooth muscle actin

AKT: serine/threonine kinase

ALP: Alkaline phosphatase

ATP: Adenosine triphosphate

ANGPT2: Angiopoietin-2 precursor

BGLAP: Bone GLA protein (also known as osteocalcin)

BMD: Bone mineral density.

BMMSCs: Bone-marrow mesenchymal stem cells

BMP: Bone Morphogenetic Proteins

BMP2: Bone morphogenic protein-2

BMSCs: Bone marrow stromal cells

BSP: Bone sialoprotein

BSP I/II: Bone sialoprotein I/II

C: Velocity of light

Ca^{+2}: Calcium

cAMP: Cyclic adenosine monophosphate

CCO: cytochrome C oxidase

CDK: cyclin-dependent kinase

cm: Centimeter

cm/sec: Centimeter per second

cm^2: Centimeter squared

CO_2: Carbon dioxide

Col: Collagen

COL1A1: Collagen Type I Alpha 1 Chain

COX: Cyclooxygenase

COX-2: Cyclooxygenase-2

CTNNB1: Catenin Beta-1 ECM Extracellular matrix

CW: Continuous emission mode

Dlx5: Distal-less homeobox 5

EGF: Epithelial Growth Factor

EGFR: Epidermal Growth Factor Receptor

EM: Electromagnetic

EMF: Electromagnetic field

ELISA: Enzyme-linked immunosorbent assay

ERK: Extracellular signal-regulated kinase

ERK: Extracellular Signal-Regulated Kinases

EZ: Exclusion zone

FcRγ: Fc receptor common γ subunit

FGF10: Fibroblast Growth Factor 10

FT: Flattop hand-piece

GaeAleAs: Gallium-aluminium-arsenide

GCF: Gingival crevicular fluid

G: Grams

h: Hour/s

hADSCs: Human adipose derived stem cell

HCL: Hydrogen chloride

HBD-2: Human β-defensin 2

He-Ne: Helium neon

HGF: Hepatocyte Growth Factor

HSP90: Heat Shock Protein 90

HUVEC: Human umbilical vein endothelial cells

IGF1: Insulin like Growth Factor 1

IHC: Immunohistochemistry

IFN: Interferon

IL: Interleukin

IL-1: Interleukin 1

IL-2: Interleukin 2

IL-6: Interleukin 6

IL-11: Interleukin 11

IL12: Interleukin 12

INOS: Inducible nitric oxide synthase

IR: Infrared

JAK: Janus Kinase

JKN: Jun Amino-Terminal Kinase

J: Joule

J/cm^2: Joules per square centimeter

L: Liter

LLLT: Low-level laser therapy

LRP-5/6: lipoprotein receptor-related protein-5 or 6.

MAH: Micro array hybridization

MAP: Microtubule Associated Protein

MAPKs: Mitogen-activated protein kinases

M-CSF: Macrophage colony-stimulating factor

MSC: Mesenchymal stem cells

m: Meter

µm: micrometer

µM: Micromoles

mA: Milliamps

mJ: millijoul

mm: millimeter

mM: Millimoles

mMol/L: Millimoles per litre

min: minute

M: Moles

µl: Microliter

µg: Micrograms

mg: Milligrams

mg/ml: Milligrams per milliliter

mJ/cm^2: Millijoules per square centimeter

ml: Milliliter

mm^2: Millimeters squared

mW: Milliwatts

mW/cm^2: Milliwatts per squared centimetre

MIS: Mullerian Inhibiting Substances

mW: milliwatt

MMD: macrophage differentiation-associated gene,

MMPs: Matrix Metalloproteases

mRNA: Messenger Ribonucleic Acid

NAD: Nicotinamide adenine dinucleotide

NADH: Reduced form of NAD+

nm: Nanometer

ng/ml: Nanograms per milliliter

Nd:YAG: Neodymium-doped yttrium aluminium garnet

NFAT: Nuclear factor of activated T cells

NF-κB = nuclear factor-κB

NGPT-2: Angiopoietin 2

NIR: Near-infrared

NO: Nitric Oxide

O_2: Oxygen

OB: osteoblast

OC/OCN: Osteocalcin

OCP: Osteoclast precursor

OD: Optical density

OPG: Osteoprotegerin

OPN: Osteopontin

OSN: Osteonectin

Osx: Osterix

M/L: Mole per liter

$MgCl_2$: Magnesium chloride

MMD: Monocyte to macrophage differentiation associated

MMP: Mitochondrial membrane potential

PBM: Photobiomodulation

PBMT: Photobiomodulation therapy

PDGFA: Platelet derived growth factor subunit A.

Ph: Measure of the hydrogen ion concentration of a solution phosphoinositide-3-kinase (PI3K)/serine-threonine kinase (Akt)

PI3K: phosphoinositide-3-kinase

PPAR: Peroxisome proliferator activated receptor

PRR: Proline-rich region

PTGS-2: Prostaglandin-Endoperoxide Synthase 2.

PTH: Parathyroid hormone

RANK: Receptor activator of NF-κB

RANKL: Receptor activator of nuclear factor-κB ligand

RI: Refractive index

ROS: Reactive oxygen species

RT-PCR: Real-time polymerase chain reaction

Runx2: Runt-related transcription factor 2

Sec/s: Second/s

Smad: Homologues of the Drosophila protein, mothers against decapentaplegic (Mad) and the Caenorhabditis elegans protein Sma)

ST: Standard (Gaussian) hand-piece

STAT: Signal Transducer and Activator of Transcription.

TGF: Transforming growth factor

TGFα: Transforming Growth Factor Alpha

TGF-β: Transforming Growth Factor beta

TGFBR3: Transforming Growth Factor Beta Receptor 3

TIMP: Tissue Inhibitor of Metalloproteinases

TNF: Tumor necrosis factor

TNF-α: Tumour Necrotic Factor alpha

TRAF: TNF receptor associated factor

TRP: Transient receptor potential

TSP: Thrombospondin

TRPV: Transient receptor potential vanilloid

TRPV1: Transient receptor potential cation channel subfamily V member 1

TRPV4: Transient receptor potential vanilloid-4.

VEGF: Vascular endothelial growth factor.

VTN: Vitronectin

W: Watt

W/cm^2: Watts per squared centimeter

W: Width

WISP1: Inducible Signaling Pathway Protein 1

SYMBLOES

λ: Wavelength

π: Pie

ω: Angular frequency

|E|: Electric field

***E*:** Energy

***f*:** Frequency

***h*:** Reduced planck constant

***i*:** Intensity

***n*:** Refractive index

E_d**:** Energy density,

$\mu_{a,m}$ **:** Mitochondria absorption coefficient,

n'_m**:** Mitochondria refractive index

***r*:** Radius or distance.

λ^3_0**:** The third power of lambda sub 0 (third power of the vacuum wavelength, the volume of a cube having an edge length equal to the vacuum wavelength)

λ_0**:** Vacuum wavelength

***N*:** Complex number given the differences of the electric fields computed at points ri for different domains dimensions.

$\int_v$**:** Volume integrals

r': The real part of the relative permittivity

r'': The imaginary part of the relative permittivity

μ_0**:** vacuum permeability

E: The electric field

H: The magnetic field

ε_0**:** The vacuum permittivity

***t*:** Time

***x*:** Generic unknown

***z*:** Electrical impedance

θ: Angular displacement

μ: Coefficient of friction

μ_0**:** Vacuum permeability constant

***v*:** Frequency

Σ: Summation operator

σ: Area charge density

ϕ: Higgs field work function

Δ: Change in a variable.

ń: Imaginary refractive index

t_{ss}: Thickness of the saline solution

t_g: Thickness of glass

t_m: Thickness of mitochondria

e^{jwt}: Time-harmonic dependence

n_m: Mitochondria refractive index

n_{ss}: Saline solution refractive index

n_g: Glass refractive index

w_{3D}: 3-dimensional glass width,

h_{3D}: 3-dimensional glass height,

$t_{3D,ss}$: 3-dimentional saline solution thickness

$t_{3D,g}$: 3-dimensional glass thickness

|E|: Electromagnetic field

r^2 : Beam spot size

°C: Degrees centigrade

>: More than

<: Less than

≤: Less than or equal to

±: Plus minus

n: Sample number

rpm**:** Revolutions per minute

α: Alpha

β: Beta

RLU: Reading light units

***P*:** Function

g: Anisotropy

I_{in}: Intensity of the incident light

I_{out}**:** Intensity of light at distance

μ_a**:** Absorption coefficient

μ_s**:** Scattering coefficient

μ_E**:** Propagation coefficient

μ_i**:** Optical coefficient

η: velocity

n_1**:** Refractive index of one medium

n_2**:** Refractive index of different medium

r: Particle density

$\mu_{a,m}$**:** Mitochondria absorption coefficient

$\mu_{a,g}$**:** Glass absorption coefficient

$\mu_{a,ss}$**:** Saline solution absorption coefficient

$\in$ **:** An element in the set of

rms: Root mean square

Δ**Em:** Change in the energy of mitochondria.

E_d**:** Energy density

P_d**:** Power density

$\int$ **:** Integral sign

$\sum$**:** Summation symbol

√**:** Radical symbol

n_m**:** Mitochondria refractive index

$\mathbf{E}_s$**:** Scattering field

$\mathbf{E}_i$**:** The electric field of the incident wave

$\boldsymbol{\varepsilon}'$**:** The real part of relative permittivity of the mitochondrion

$\boldsymbol{\varepsilon}''$**:** The magnitude of the imaginary part of the relative permittivity of the mitochondrion.

V: Volatage

CHAPTER I

The electromagnetic field

1.1 INTRODUCTION

Bone regeneration has captured the interest of many scholars and investigators, in the field of medicine and dentistry. Several therapeutic strategies have been proposed to optimize the conventional treatment of bone defects. However, there are many situations in which speed and effectivenss of the healing process can have a great impact on the success of various medical or surgical conditions, as well as in metabolic diseases. Photobiomodulation (PBM) at various wavelengths of the electromagnetic (EM) spectrum appears to be an attractive therapeutic choice, as a non-invasive modality, in accelerating bone repair and regeneration in critical and non-critical bone defects without adverse effects.

The term biophotonics refers to the interaction between the light and biological tissue such as: organelles, cells, fibers, epithelial layers, and vessels. This new therapeutic modality has been rapidly growing, as a multidisciplinary field in the healthcare [1]. Many therapeutic applications require knowledge of the light flux through the tissue. Photons that enter the tissue are scattered multiple times until they either escape or are absorbed (Figure1) [2]. Computer simulations that track the movement of photons through the biological tissues are based on the absorption and scattering properties of each specific tissue. The absorption and scattering coefficients and anisotropy factors (The direction in which photons are scattered in tissue) are determined through a combination of experimental measurements and the optical theory [3]. Furthermore, knowledge of the optical properties of tissues submitted to phototherapy is also of considerable importance to the obtainment of successful clinical outcomes [4]. Once established, the light attenuation coefficient, distribution of photons, scattering pattern within the tissue, and the optimization of the effects of phototherapy become a less complicated task [5]. From basic science regarding culture plates and media to the

applications on skin, mucous membranes, bone, enamel, and dentin, the optical properties of such structures has raised interest in the academic community [6-9]. Studies have shown that the EM fields (EMFs) can promote osteoblast-like cell proliferation, or contrarily, induce differentiation and enhance bone mineralization [10]. The clinical benefits of the EMF therapy in enhancing osteogenesis have been acknowledged for decades. However, the disagreements regarding the underlying mechanisms continue to be sought [11]. Therefore, understanding the concept of EMF behavior and its attenuation in a tissue, and the optical properties of the light interaction with the matter, can assist in optimization of the therapeutic outcomes. Moreover, an understanding of light propagation in a tissue and the information content of the scattered light from tissues are mandatory for a successful realization of the potential of these optical approaches for achieving quality health

1.2 ELECTROMAGNETIC FIELD (EMF)

Light is part of the spectrum of electromagnetic radiation (ER), which ranges from radio waves to gamma rays. ER has a dual nature as both particles and waves. As a wave that is crystallized in Maxwell's equations, light has amplitude, which is the brightness of the light, wavelength, which determines the color of the light, and an angle at which it is vibrating, called polarization [12]. The wavelength (λ) of light is defined as the length of a full oscillation of the wave, such as shown in (Figure 1). In terms of the modern quantum theory, ER consists of particles called photons, which are packets (quanta) of energy, which move at the speed of light [13].

The EMF is a physical field produced by moving electrically charged objects. It influences the behavior of materials or charged particles around the field. Light is an oscillating electric and magnetic field [14]. The oscillating charge creates an electric

field, which induces a magnetic field (Figure 1) [15]. The EM radiation is described as waves (photons) of the EMF, propagating through space, carrying EM radiant energy, which influences the behavior of materials or charged particles around the field. The total amount of energy of the field is called EMF energy [16]. An EM wave is a traveling wave, which has time-varying electric and magnetic fields that are perpendicular to each other and to the direction of the propagation *z* (Figure 1) [15].

The basic properties of light are its wavelength, frequency, energy and speed. The wavelength and frequency of light determine where the light is located along the EM spectrum. Figure 2 shows the EM spectrum, which is the range of frequencies (the spectrum) of the EM radiation and their respective wavelengths and photon energy [17]. The visible wavelengths range approximately between 400–750 nm; beyond 750 nm is invisible light. While the range from 750–1500 nm, the light is defined as near infrared (NIR). The EM wave can be described by any of the following three physical properties: frequency (f), Wavelength (λ), or photon energy (E). Figure 1 shows all the possible frequencies of the EM radiation and the corresponding photonic energies [15]. The spectrum covers vast range of wavelengths from size of an atom to almost the size of the universe (over 26 orders of magnitude). The corresponding photonic energies occupy similar range from the immeasurable to the highly dangerous [15]. The photonic energy (E) of a single photon associated with the EM wave, increases with frequency and is given by the relationship shown below

$$E = h \times f \text{ or } h \times c/\lambda \qquad (1)$$

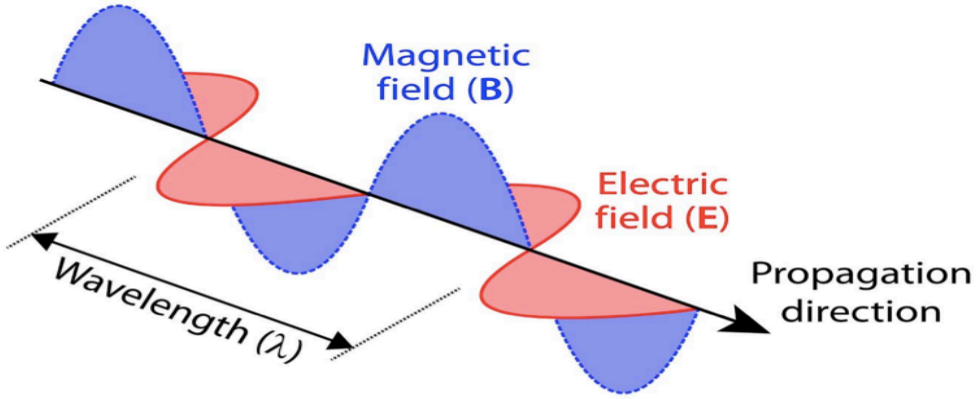

Figure 1: An electromagnetic wave consisting of electric and magnetic oscillating fields. In this example, the oscillating electric field vectors are indicated in red, while the blue lines represent the magnetic field vectors [15].

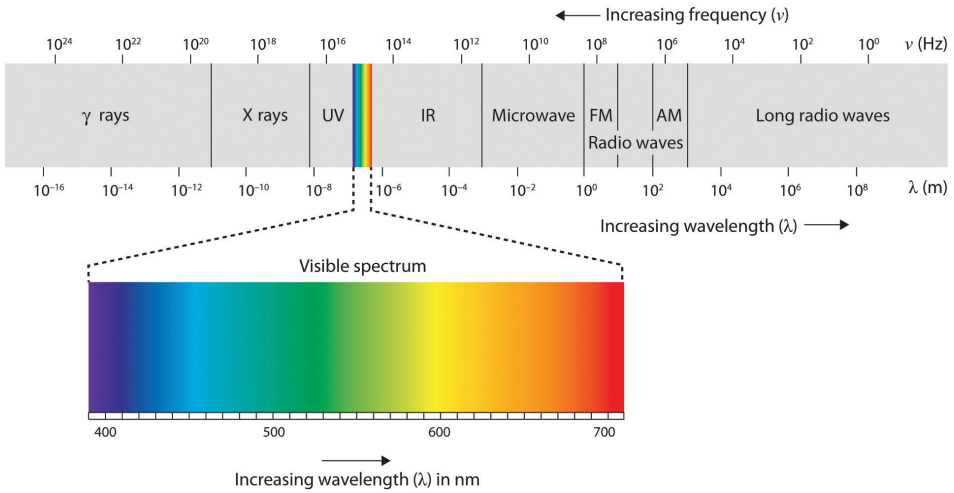

Figure 2: The electromagnetic spectrum showing the boundaries between different regions and the type of atomic or molecular transition responsible for the change in energy. The colored inset shows the visible spectrum. Source:
(www.commons.wikipedia.org) (Modified [15]).

When the EM wave of optical ray encounters a biological tissue, multiple effects of reflectance, absorption, and scattering take place, due to inhomogeneity of the matter (Figure 3). To characterize the properties of a biological tissue, four optical parameters can be derived from directed or undirected measurement of the biological tissues, which are as follows: refractive index (n), absorption coefficient (μ_a),

scattering coefficient (μ_S), and anisotropy factor (g). These parameters play a fundamental role in laser-tissue interaction. The ability of the a medium or a tissue to absorb EM radiation depends on a number of factors, mainly the electronic distribution in its atoms and molecules, the thickness of the absorbing layer, intrinsic parameters such as the concentration of the photoacceptors, and the wavelength [18]. Furthermore, it was suggested that the interaction of radiations with the tissues could depend on the number of the mitochondria in these tissues. Thus, when PBM is carried out by radiation at a very low power, photons are absorbed by the subcellular chromophores in the cell organelles, mainly mitochondria. Cells presenting higher numbers of mitochondria respond better to PBM therapy (PBMT) than those presenting with a lower number of mitochondria [19]

1. 3 LIGHT AND TISSUE OPTICAL PROPERITES

1.3.1 Propagation of Polarized Light in Tissues

Laser is an acronym for Light Amplification by Stimulated Emission of Radiation, which emits light through a process of optical amplification based on stimulated emission of photons [20]. The emitted laser light has a high degree of spatial and temporal coherence, which is unattainable using other sources. The laser beam can be focused to a very tiny spot, thereby, achieving a very high irradiance or they can be used as a beam of low divergence, in order to concentrate their power at a large distance [21]. When the light interacts with the tissue, the photons are absorbed or remain unabsorbed within the tissue. The unabsorbed light either is transmitted, emerging from other side or else it gets re-emitted (Figure 4) [2]. When light is in the tissue, it may change its direction or continue to travel in its previous path. Light is assumed as a stream of photons, and the particle theory of light explains the quantum

nature when absorption of light increases the energy of the system. The interaction of light with tissue depends on the properties of incident light and optical properties of tissue, which controls the light propagation [22].

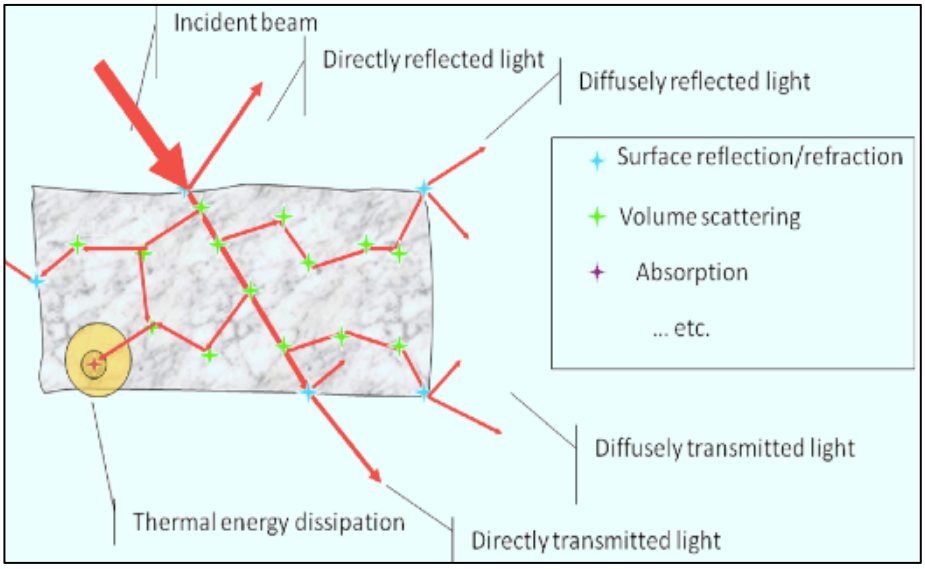

Figure 3 Schematic of light propagation in tissue (courtesy of Anna N Yaroslavsky, Wellman Center for Photomedicine).

The interaction of a material with the optical waves and photons is strongly dependent on the structure, which can then be used to control light field distribution and light propagation. This allows the development of a large range of key components for optical schemes, which is a major field of photonics [23]. Light energy propagation in biological tissue is related to the tissue optical properties. Refractive index is an essential parameter of tissue optical characteristics. The analysis of light propagation and the optical characterization of a heterogeneous medium, such as bone tissue, are very complex. Most available methods apply to a homogeneous medium or require isotropic propagation, which is not the case with bone tissue [24]. This was one of the challenges that we faced when we examined the EM behavior. Therefore, we

introduced, for the first time, an EM model to evaluate the propagation of the PBM light in illuminated mitochondrion (Chapter III).

1.3.2 Absorption and scattering phenomena

When light travels through biological tissues, multiple scattering and absorption are responsible for the decay and an enlargement of a laser beam. Light propagation within a tissue, therefore, depends on the scattering and absorption properties of its components. The wavelengths of the absorbed light are generally characteristic of the absorbing components, called chromophores. Scattering depends upon variables, such as shape, size, and refraction index of the tissue at a certain wavelength, and is mostly due to discontinuities in the refractive index on the microscopic level [25]. Futhermore, the absorption and scattering of laser light are important in predicting the extent of the tissue injury. As tissue is irradiated, the light traveling through the tissue is attenuated by the absorption and scattering phenomena [26]. The proportionality constant describing the amount of light attenuated by absorption is called the absorption coefficient (μ_a) [24]. The constant describing the attenuation of light due to scattering away from the direction of propagation is the scattering coefficient (μ_S). While the absorption coefficient (μ_a) is the probability of photon absorption in a medium per unit of path length [24]. The anisotropy coefficient (g) is a parameter, which describes the fraction of light scattered into any given direction and is equal to the average cosine of the scattering angle [27]. Effective attenuation is defined as, the sum of absorption and scattering coefficients, which is called the propagation coefficient (μ_t),

$$\mu_t = \mu_a + \mu_s \qquad (2)$$

However, the linear optical coefficient μ_i ($I \rightarrow a,s,t$) are defined, so that define the absorption, scattering, and propagation mean free paths, respectively [28].

$$I_a = \mu_a^{-1},\ I_s = \mu_s^{-1},\ I_t = \mu_t^{-1} \tag{3}$$

The function *p(s, s')* is the probability density function, giving the probability of photon scattered from an initial propagation direction s to a final direction *s'*.

The linear optical coefficients are related to the absorption and scattering cross-sections (S_a and S_S respectively) by the below equation, where r is the particle density.

$$\mu_a = r \cdot s_a\ ,\ \mu_S = r \cdot s_S \tag{4}$$

The integral of phase function or the differential cross-section may be normalized to one or more frequently to ratio $\mu_S / (\mu_a + \mu_S)$.

In general, the scattering coefficient (μ_S) and scattering anisotropy factor (g) of a tissue are dependent on the refractive index mismatch between the cellular tissue components such as; cell membrane, cytoplasm, cell nucleus, cell organelles, melanin granules, and extracellular fluid. Most of the light scattering in a tissue is believed to take place at various membrane boundaries, in both the cell membranes as well as the membranes of the various organelles inside the cell. The light attenuation in a tissue is caused by the absorption, scattering, and at a small amount by reflectance phenomenon. Chromophores such as, melanin, hemoglobin and proteins may influence the light scattering and absorption events, and the tissue surface may

produce reflectance [26].

In the NIR region of the EM spectrum, the total amount of absorption is due to the interaction with all chromophores. However, scattering is quite low. The effect of scattering is therefore much more important than absorption [29]. It is worth mentioning here that the material and tissues can be divided into two classes based on how the velocity of light of a particular wavelength varies in a material [30,31]. These classes of materials are as follows:

1- Materials, whose refractive index does not depend on the direction of the light travels, are called isotropic materials. They have a single and constant refractive index for each wavelength.
2- Materials, whose refractive index does depend on the direction of the travelled light, are called anisotropic.

1.3.3 Absorption theory

In a non-scattering homogeneous medium with an absorber present, the loss in intensity is due to the absorption, as the light travels through a medium is given by the Beer Lambert law:

$$I_{out} = \exp(-\mu_a d) \quad (5)\ I_{in}$$

where I_{in} is the intensity of the incident light, while I_{out} is the intensity at distance d (mm) from the input,. The μ_a is the absorption coefficient for that medium in mm^{-1}. The inverse of μ_a, $1/\mu_a$ can be taken to be the absorption length, which is the distance where the light has to travel, in order to be attenuated by a factor of 1/e [32,33]. The effectiveness of a compound, as an absorber, is given by its extinction coefficient also identified as a specific absorbance, ε (mm^{-1}@$Molar^{-1}$). This is equal to its absorption

coefficient per unit of concentration in Molar [32,33]. The absorption coefficient for a single compound at a given concentration c is therefore given by:

$$\mu_a = c\varepsilon \quad (6)$$

Another quantity that is often found in the literature is referred as an absorbance or an optical density (OD):

$$\text{OD} = \log_{10} \; I_{out} / I_{in} \quad (7)$$

This is normally expressed in units of log base 10. Some authors also used units of log base 10 for μ_a and ε and often the log base used is not specified, leading to considerable confusion. In biological tissues there are in general many different absorbing compounds present [32,33].

1.3.4 Refractive index

Refractive Index (Index of refraction) is a value calculated from the ratio of the speed of light in a vacuum to that in a second medium of greater density. The refractive index variable is most commonly symbolized by the letter n or n' in descriptive text and mathematical equations. Snell's law was originally defined by the relationship between the incident angles and the ratio of the velocities of light in the two media [34]. The refractive index is the ratio between the velocity of light (c) in free space (For all practical purposes, either air or a vacuum) and its velocity η in a particular medium:

$$n = c/\eta \quad (8)$$

As the refractive index of a material increases, the greater the extent to which a light beam is deflected (or refracted) upon entering or leaving the material. The refractive

index of a medium is dependent (to some extent) upon the frequency of light passing through, with the highest frequencies having the highest values of *n*.

It is worth mentionaing here, that the reflection is a phenomenon that occurs when an EM wave of a given wavelength moves from a medium with of a refractive index n_1 to a different medium with a refractive index n_2 (Figure 4) [2]. In the case of normal incidence (90° between incident light and target medium), a portion of the light is back reflected [35]. The tissue components that contribute most to the local refractive index variations are the connective tissue fibers (Either collagen or elastin), which form part of the non-cellular tissue matrix around and among cells; cell membrane, cytoplasmic organelles (Mitochondria, lysosomes, and peroxisomes), cell nuclei, and melanin granules [36]. While refraction is another light property, which describes how the light bends when it passes through a substance. In addition, the light exhibits a property called dispersion, in which the light breaks down into individual wavelengths, such as in a prism.

1.3.5 Optical tissue interaction

The interaction of the radiation with the matter can be considered the most important process in medicine and dentistry. The ability of light to penetrate the tissue and deposit energy via the optical absorption properties of the tissue is the key to the therapeutic applications. The second step is to use the optical properties in a light transport model to predict the light distribution and energy deposition. Moreover, the absorption and scattering coefficients, anisotropy factor of the tissue, and the thickness of the target tissue layers need to be taken into consideration [26]. Thus, it is crucial to examine first the optical properties of the biological tissue, focusing on the interaction of the light with the tissue. This importance is due to the dependency of

light penetration inside the biological tissues on the laser parameters and the optical properties of the target tissue [37]. Therefore, each biological tissue has its specific functional response when irradiated by light [38].

Evidence-based research has tabulated the optical properties (Absorption, scattering, anisotropy, reduced scattering, refractive index) of various tissues measured at some or many wavelengths [39-42]. However, the tabulated values are only an approximation of actual optical properties of a particular tissue *in vivo*. Firstly, the tabulated values may not be accurate due to the measurement artifacts. Secondly, the living tissue of a particular person is subject to variations in blood, water, and collagen contents as well as fiber development. These variations are significant from one person to anothere, one site to another of the same person or even from one time point to another at the same site [39-42]. The tabulated values may not include the wavelength of interest.

Perhaps it is more useful to understand the expected standard behavior of optical properties, and to anticipate the variation in tissue constitution that yields the tissue optical properties at any desired wavelength (Figure 4) [2]. Many biological tissues are optically anisotropic including bone. The ability of a medium or a tissue to absorb the EM radiation depends on number of factors; mainly the electronic distribution in its atoms and molecules, the thickness of the absorbing layer, and the intrinsic parameters such as; the concentration of the photoacceptors and the wavelength [43]. So, when PBM is carried out by radiation at a very low power, photons are absorbed by the subcellular chromophores in the cell organelles, mainly mitochondria, such as cells presenting with higher numbers of mitochondria would respond better to PBMT than those presenting with a lower number of mitochondria [19]. The absorption and the scattering phenomena become significantly low, as the radiation wavelength gets

longer, such as the penetration depth of NIR. Moreover, at longer wavelengths, water becomes an important absorber and penetration depth of radiation gets lower again [44]. So, it is crucial to have knowledge of the tissue properties and the light interaction, for the development of a novel optical technology, especially in the field of photobiomodulation therapy (PBMT). Many investigations related to tissue optical properties determination are available in literature. However, the optical properties of many tissues have not been studied in the scope of a wide range of wavelengths.

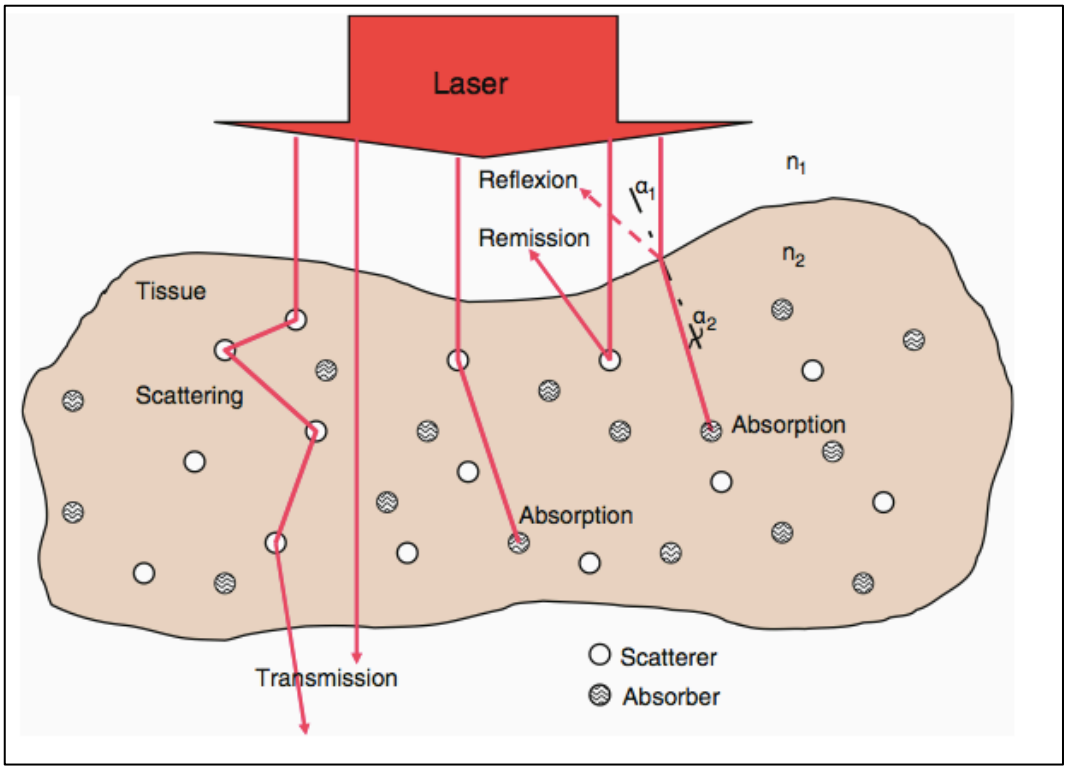

Figure 4: The optical behavior of tissue layer during irradiation with laser light [2]

Measurement of tissue optical properties and determination of light propagation parameters in a tissue may offer several clinical applications. For any phototherapy application, the induced effect will depend on the chromophores concentration and

the light flux at the target site. The determination of these parameters is, therefore, crucial for the success of any phototherapy. Equally, a change in biochemical composition or morphology of tissue results in a change in the spectral dependence and magnitude of μ_a and μ_s, respectively. Therefore, the absorption and the scattering of laser light are important in predicting the extent of tissue injury or therapeutic benefit.

It is important to mention here, that the optical window of wavelengths ranging between 600-1100nm exerts several therapeutic outcomes (Figure 5). Most of the biological tissues are characterized by a strong optical scattering in this region. The photons both diffuse and attenuate in the biological tissues. Scattering of laser light by cells, nuclei, mitochondria, lysosome, macromolecules, membranes and other components, results in diffusion of light in the biological tissues. The optical scattering originates from light interaction with the biological structures, ranging from cell membranes to whole cells. The size of these scatterers varies from 10 nm to 10 microns [36]. These scatterers are distributed randomly in a biological tissue; photons usually encounter multiple scattering events. As the scattering coefficient (μ_s) is the probability of photon scattering in a medium per unit path length, while the scattering mean free path (Spatial interval between two adjacent scatterings) is the reciprocal of scattering coefficient.

The scattering coefficient of biological tissues depends on the wavelength of the laser. In most biological tissues, the majority of scattered light travels in forward direction. So, these biological tissues have anisotropy, which is convenient to define a phase function p (θ) of a photon to be scattered by an angle θ. If p (θ) is a constant and not dependent on θ, the media is called isotropic, otherwise, it is called anisotropic

medium [45]. The scattering of light arises because of the density variation. The effect is due to the presence of different types of molecules in a tissue [45]. For most tissues, over the wavelength range of interest (500-1000nm), the scattering coefficient is considerably larger than the absorption coefficient with one exception, which is the liver tissue whose is highly light absorber. Scattering of light in a biological tissue is highly anisotropic. It tends to be strongly forward peaked, representative of large particle scattering.

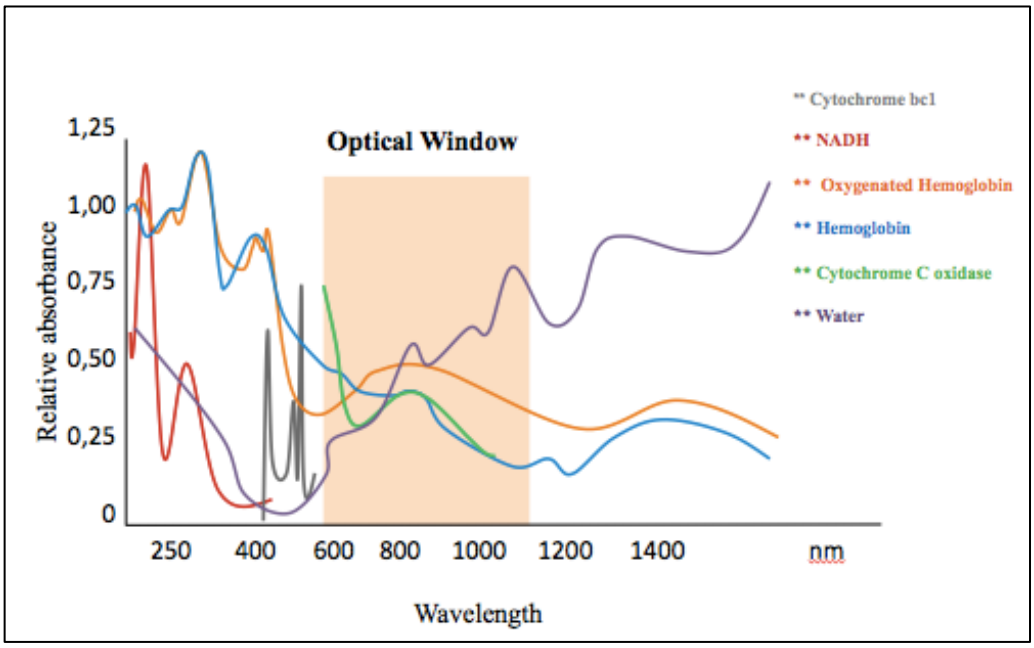

Figure 5: Absorption spectra of the main chromophores in living tissue on a log scale showing the optical window where visible and NIR light can penetrate deepest into tissue. [Modified 44].

1.4 CONTRIBUTIONS OF THE MITOCHONDRIAL CHROMOPHORES FOR RED AND NEAR INFRARED (NIR) LIGHT

The mitochondrion is an extremely interesting and important organelle in the eukaryotic cells. It is the only organelle (other than the nucleus, of course) that has its

own DNA independent of the cell's chomosomal DNA; because of this and the fact that the organelle divides independent of the cell (Figure 6) [46].

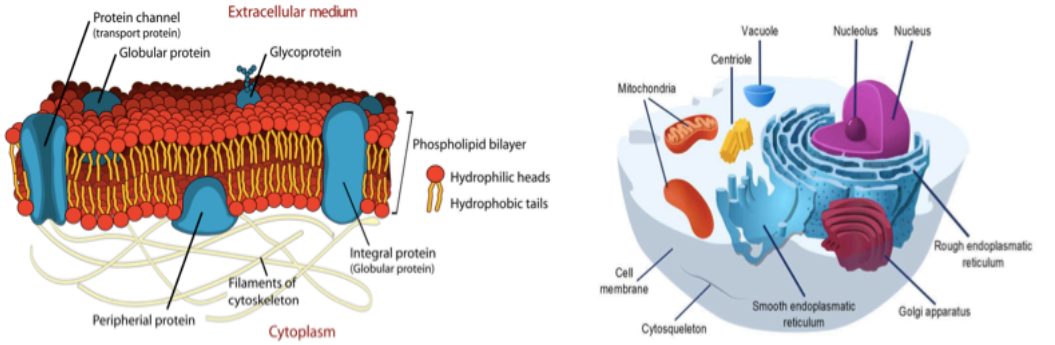

The phospholipid bilayered cell membrane. The biological cell with its main organelles.

Figure 6: The biological cell and its cell membrane.
Modified from http://commons.wikimedia.org/

Among other things, it performs cellular respiration, has an electron transport system that occurs across membranes, and produces ATP. The mitochondrion has four compartments: an outer membrane, an inner membrane (Made of cardiolipin), an intermembrane space (between outer and inner membranes), and a matrix (Inside inner membrane) (Figure 6) [47]. The processes that happen in the mitochondrion are pyruvate oxidation, the Krebs cycle, the metabolism of amino acids, fatty acids, and steroids, as well as, generation of the adenosine triphosphate (ATP). The ATP is used for energy, which is through the electron-transport chain and the oxidative-phosphorylation system (respiratory chain) in the inner mitochondrial membrane (Figure 7) [48].

Mitochondria are generated by the expression of genes on both nuclear and mitochondrial genomes. Mitochondrial biogenesis is highly responsive to the cellular demands for energy and environmental stimuli (Figure 6) [46]. Since the beginning

of the 20th century, the idea of the EMFs could interact with cells, tissues and organisms presented, as it was known that cells have and are surrounded by electrical charges. Subsequently, the ions have an important role in cell physiology (Figure 7) [48].

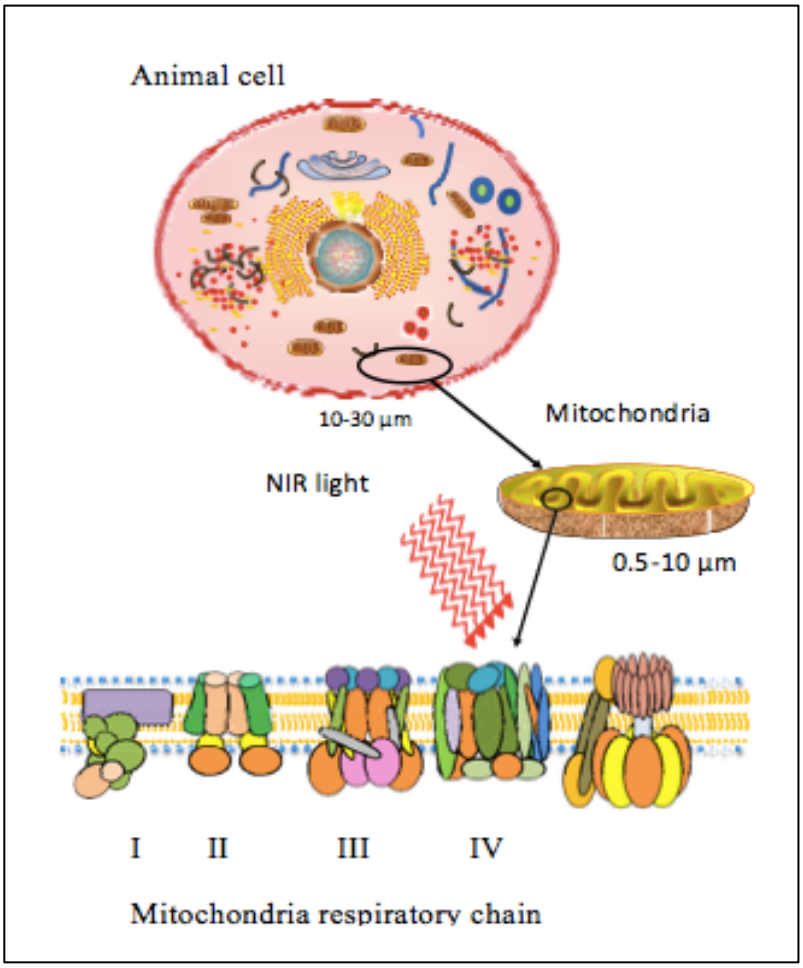

Figure 7: The role of IV mitochondrial respiratory chain in the mechanism of PBM [48].

Phototherapy is involved in the transformation of light energy to chemical, kinetic or heat energy, in order to achieve desired physiological results. As stated by the "*First Law of Photobiology*", the light energy must be absorbed by an atom or molecule in order to initiate a physical or chemical process [49]. Therefore, the light that is used

for therapeutic applications must be absorbed by specific chromophores in the biological tissue. These chromophores may be endogenous (naturally occurring in cells or tissue), which is related to PBM, or exogenous (deliberately added to cells or tissue for a therapeutic purpose).

The wavelength of the light consists of packets of EM energy that also has a wave-like property. It is expressed in nanometres (nm). Wavelengths in the range of red light and NIR are able to induce significant physiological changes inside the tissue. According to modern knowledge, the red light inside the cells activates the mitochondrial enzyme (Cytochrome c oxidase), improving the mitochondrial respiration, and oxygen consumption [50,51]. This shift in the cellular metabolism leads to other changes in cell function, e.g. gene expression and growth factor production [52]. As the principle chromophores for PBM are located inside the mitochondria, it follows that the cells with a large number of mitochondria and a high metabolic activity are particularly responsive to light [19], as it is the case in bone cells [53]. One of the most frequently observed changes when PBM experiments are conducted *in vitro* was modulation of levels of reactive oxygen species (ROS) [54]. The production of modest amounts of ROS by red/NIR light being absorbed in the mitochondria is reasonably well established [55]. It is known that the mitochondria are one of the most important sources of ROS in mammalian cells [56].

The structure of chromophores and their redox state determine which wavelengths will be absorbed. PBM devices are typically within the range of 600-1100 nm because there are many absorption peaks for cytochrome c oxidase in that range; they penetrate tissues better than other wavelengths [44]. However, there is a range between 700-770nm, where broadly speaking, the results are likely to be

disappointing [57]. Since the biological effects of light continue to be observed, as the wavelength increases in the infra-red region (>1000 nm), beyond those known to be absorbed by CCO. It is now thought likely that an alternative chromophore must be responsible. The obvious candidate for this latter is water molecules whose absorption spectrum has peaks at 980 nm and in most wavelengths longer than 1200 nm. Moreover, water is by far the most prevalent molecule in a biological tissue (particularly considering its low molecule weight = 18). Wavelengths longer than 900 nm are also absorbed by water and not only by CCO. It is speculated that these longer wavelengths are as well absorbed in phospholipid bilayers and cause molecular vibration sufficient to perturb ion channels and alter the cellular function. For various reasons, it has been proposed that PBM can have a biological effect on the ion channels [57]. These reasons include the biological effectiveness of wavelengths that are much longer than those absorbed by CCO, the rapid influx of calcium into cells exposed to PBM irradiation, and certain applications of PBM to relieve pain that cannot be explained by overstimulation of mitochondria. Recent studies have revealed that the existence of a large group or family of ion channels called transient receptor potential (TRP) channels (Figure 8) [58,59]. So, NIR light in the region of 980nm may directly disturb the conformational structure of the transient receptor potential cation channel subfamily V (TRPV) channels via absorption by nanostructured water [60]. It is essential to mention the importance of the penetration depth, which is defined, as the depth at which there is a sufficient power density to be above the threshold required for a therapeutic benefit. It is accepted that the penetration of the light into a tissue is governed by both the absorption and scattering, as well as by the composition and thickness of the tissue [61].

EM fields (EMFs) are reported to have some beneficial effects on bone and it has been suggested that they stimulate the bone formation and inhibit the bone resorption [62]. Subsequently, it has a great effect on bone metabolism. Therefore, EMFs have been successfully utilized in clinical applications of bone regeneration. However, the cellular mechanism (s) by which EMF can enhance bone remodeling and repair are still elusive. Our cellular *in vitro* studies have shed a light on the mechanism of the intracellular interaction of the photonic energy of 980nm on osteoblast proliferation and differentiation (Chapter V).

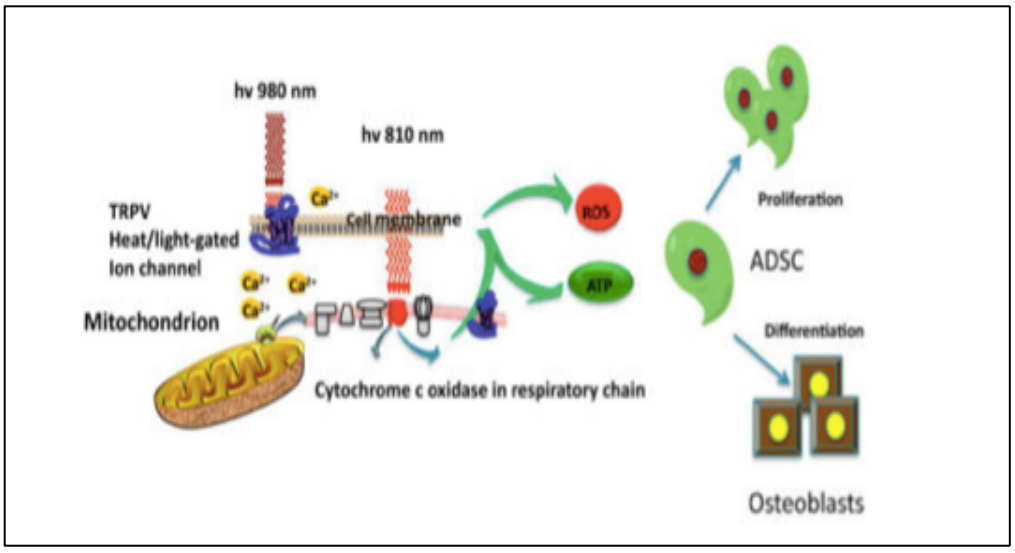

Figure 8: Photobiomodulation mechanism of action of 810 nm, versus 980nm,via cytochrome c oxidase; heat-gated ion channels respectively [58]. Abbreviation: TRPV Transient receptor potential cation channel subfamily V, ADSC: Adipose-derived stem cells.

1.5 WAVELENGTH-DEPENDENT PENETRATION DEPTH OF LIGHT

The use of PBM in patients almost exclusively involves red and near-infrared light (600– 1100 nm) [63]. The absorption and scattering of light in the tissue are both much higher in the blue region of the EM spectrum than the red light. The principal

tissue chromophores (hemoglobin and melanin) have high absorption bands at shorter wavelengths, tissue scattering of light is higher at shorter wavelengths and water strongly absorbs infrared light at wavelengths >1100.

Wavelength has a great impact on the tissue penetration. The shorter wavelengths ranging from 600 to 700 nm are considered the best to treat superficial tissues, and those between 780 and 950 nm are chosen for deeper-seated tissues, due to longer optical penetration distances through tissue with the latter group [64]. Moreover, the NIR wavelengths require substantial doses of light to achieve an optimal outcome [64]. Beam coherence is maintained as the laser beam penetrates the tissue along with polarization, which may be an important factor in allowing the laser light to effectively treat deeper-seated tissues.

The infrared wavelengths show better effects on bone repair compared to red wavelengths. Hudson et al., 2013 *ex vivo* study showed that the 808nm at 1mW/cm^2 can penetrate at 3.4 cm in bovin tissue (Figure 9), when irriadaited with top-hat beam profile (A near-uniform fluence at 1cm^2 area) [65]. However, when the 980nm irradiated the tissue at 1mW/cm^2 fleucne with the same beam profile showed a 2.2cm penetration depth in bovin tissue (Figure 10) [65]. Thus, I have chosen the 980nm wavelength for my *in vitro* experiments to demonstrate its effects in bone regeneration with two different beam profiles (Chapter V). The optical properties of a tissue affect the therapeutic applications of the light. Hence, the ability of light to penetrate a tissue, interrogate the tissue components, and deposit energy, via the optical absorption properties of the tissue, is the key of the therapeutic applications. Furthermore, complete knowledge of the light penetration depth and its distribution inside the biological tissue is difficult to obtain, due to the absorption and scattering,

which are depending on the wavelength, tissue biochemistry and anatomy [26]. Hence, specifying the optical properties of a tissue is the first step towards properly developed devices, and planning therapeutic protocols. While the second step is to use the optical properties in a light transport model to predict the light distribution and energy deposition. These issues have been addressed in our *in vitro* experimental setup.

Development of phototherapy has stimulated the investigation of optical properties of various biological tissues, since the efficacy of laser treatment depends on the photon propagation and fluence rate distribution within the irradiated tissues. Numerous investigations related to determination of tissue optical properties are available. However, the optical properties of many tissues have not been well studied in a wide wavelength range. This has led us to introduce EM models, for the first time, to understand the behavior of the NIR light attenuation in the mitochondrial biological aspect (Chapter III).

1.6 SUMMARY

The development of an optical method in modern medicine in the areas of diagnostics, therapy and surgery has stimulated the investigation of the optical properties of several biological tissues, since the efficacy of laser treatment depends on the photon propagation and on the distribution of the fluence rate within the irradiated tissues. Intimate knowledge of tissue optical properties is crucial for the development of the novel optical technologies of PBM therapy. Many investigations related to tissue optical properties determination are available in literature. However, the optical properties of many tissues have not been studied in the scope of a wide

wavelengths range. Therefore, the electromagnetic modeling that we developed in our studies has shed a light on this (Chapter III).

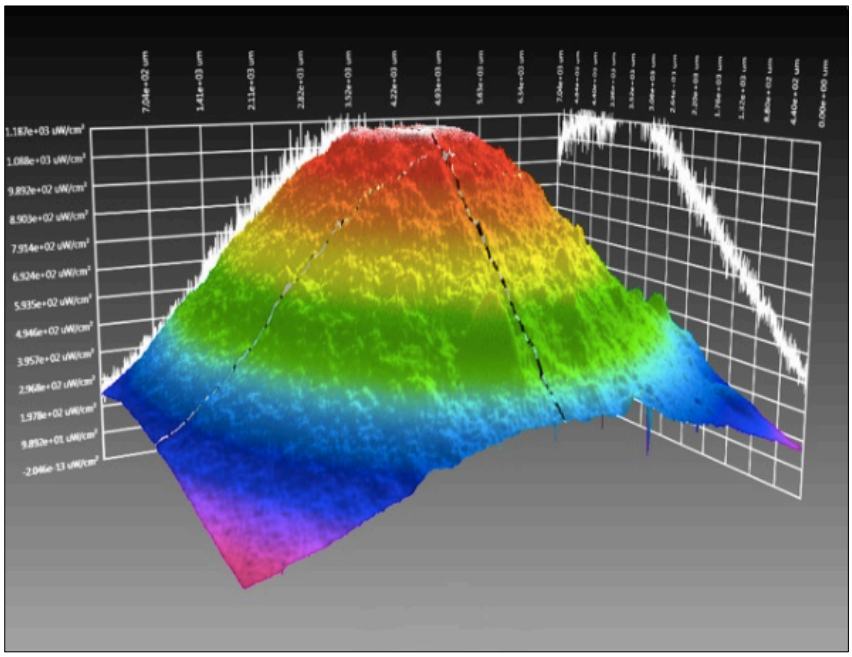

Figure 9: A Laser light pattern 808nm at 3.3cm tissue depth [65].

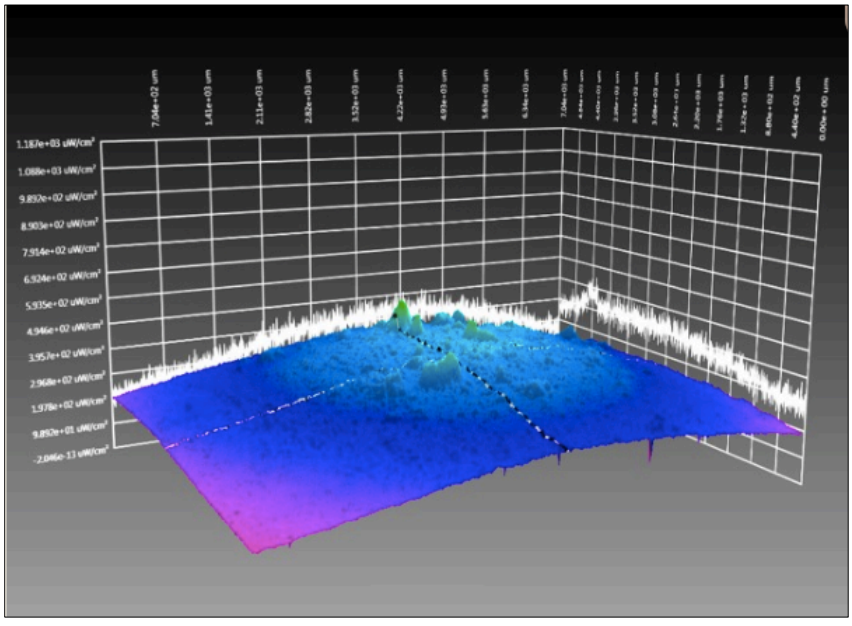

Figure 10: A Laser light pattern 980nm at 2.2cm tissue depth [65].

1.7 REFERENCES

1. Serafetinides AA, Makropoulou M, Drakaki E. Biophotonics in diagnosis and modelling of tissue pathologies. Biophysics of laser and tissue interaction. Proc. of SPIE 2008;7027:702715-2
2. Steiner R. Laser-Tissue Interactions. In: Raulin C., Karsai S. (eds) Laser and IPL Technology in Dermatology and Aesthetic Medicine. Berlin, Heidelberg: Springer; 2011.
3. Benaron, DA, Stevenson DK. Optical time-of- flight and absorbance imaging of biologic media. Science.1993;259:1463-1466.
4. Y. Kang, A.B. Rabie, R.W. Wong, A review of laser applications in orthodontics, Int. J. Orthod. Milwaukee.2014;25:47-56.
5. Genina EA, Bashkatov AN, Tuchin VV, Optical clearing of cranial bone, Adv. Opt. Technol. 2008;2008:1-8.
6. V.G. Peters, D.R. Wyman, M.S. Patterson, G.L. Frank, Optical-properties of normal and diseased human breast tissues in the visible and near-infrared, Phys. Med. Biol.1990;35:1317-1334.
7. Prince S, Malarvizhi S. Monte Carlo simulation of NIR diffuse reflectance in the normal and diseased human breast tissues, Biofactors.2007;30:255-263.
8. Silva DFT, Mesquita-Ferrari RA, Fernandes KPS, Raele MP, Wetter NU, Deana AM. Effective transmission of light for media culture, plates and tubes, Photochem. Photobiol.2012;88:1211-1216.
9. Wang LV, Jacques SL. Methods Source of error in calculation of optical diffuse reflectance from turbid media using diffusion theory, Comput. Programs Biomed. 2000;61:63-170.

10. Bique AM, Kaivosoja E, Mikkonen M, Paulasto-Kröckel M. Choice of osteoblast model critical for studying the effects of electromagnetic stimulation on osteogenesis *in vitro*, Electromagnetic Biology and Medicine, 2016;35(4) 353-364.
11. Panagopoulos DJ, Karabarbounis A, Margaritisa LH. Mechanism for action of electromagnetic fields on cells. Biochem Biophys Res Commun. 2002;298:95-102.
12. Hall G. Maxwell's electromagnetic theory and special relativity dynamical theory of the electromagnetic field". Philosophical Transactions of the Royal Society. 2008;336(1871):459-512.
13. Mullingan Joseph F. Heinrich Hertz and the development of Physics. Physics Today. 1989;42(3):50-57.
14. Feynman R. A field is any physical quantity, which takes on different values at different points in space. The Feynman Lectures on Physics Vol. II: Addison Wesley Longman; 1970.
15. Verhoeven GJJ. The reflection of two fields - Electromagnetic radiation and its role in (aerial) imaging. AARGnews.2017;55(12):13-18
16. Gamow G. The Great Physicists from Galileo to Einstein. Dover Publications; 1988.
17. Glenn E. The Electromagnetic Spectrum. The Physics Hyper textbook: Hypertextbook.com; 2010.
18. Niemz MH. Laser-tissue interactions: Fundamentals and applications. New York: Springer-Verlag; 2007.
19. Zein R, Selting W, Hamblin MR. Review of light parameters and photobiomodulation efficacy: dive into complexity. J Biomed Opt. 2018;23(12):1-17.

20. Choudhury AKR. Principles of Colour and Appearance Measurement, Object appearance, colour instrumental measurement. Woodhead Publishing; 2014
21. Benaron DA, Cheong WF & Stevenson DK. Tissue optics. Science, 1997;276:2002-3.
22. Welch AJ, Van Gemert MJC. Optical-Thermal response of laser-Irradiated Tissue. USA: Springer, second edition; 2011.
23. Welch AJ, Van Gemert MJ. Optical-Thermal response of Laser-Irradiated Tissue. Second edition. USA: Springer;1995.
24. Ansari MA, Mohajerani E. Mechanisms of Laser-Tissue Interaction: I. Optical Properties of Tissue. J Lasers in Med Sci. 2011;2(3):119-125.
25. Jacques SJ, Pogue BW. Tutorial on diffuse light transport, J. Biomed. Opt. 2008;13:041302.
26. Jacques S. Optical properties of biological tissues: a review. Phys. Med. Bio. 2013;58:R37-61.
27. Wilson BC. Measurement of Tissue Optical Properties: Methods and Theories. In: Welch AJ, Van Gemert MJC. Optical-Thermal Response of Laser-Irradiated Tissue. Lasers, Photonics, and Electro-Optics. Boston MA: Spinger; 1995.
28. Baschir L, Dontu S, Miclos S, Savastru D, Tautan M, Tenciu D, Ciucu C. Modeling of laser light transport in tissue. Proc. of SPIE. 2008;7027:702718-6.
29. Flock ST, Wilson BC, Patterson M. Total attenuation coefficients and scattering phase functions of tissues and phantom materials at 633nm. Medical Physics. 1987:14:835-841.
30. Ashcroft NW, Mermin ND. Solid State Physics. USA: Cengage Learning; 1976. ISBN 9780030839931.

31. Newnham RE. Properties of Materials: Anisotropy, Symmetry, Structure. UK: Oxford University Press; 2005. ISBN 9780198520764.
32. Bickel, W.S., Davidson, J.F., Huffman, D.R., Kilkson, R. Application of polarization effects in light scattering: A new biophysical tool, Proceedings of the USA:National Academy of Science;1976
33. Bohren CF, Huffman DR. Absorption and Scattering by small particles. NY: John Wiley & Sons; 1983.
34. Ben-Benjamin JS, Cohen L. Equations of motion for rays in a Snell's law medium. J Acoust Soc Am. 2015;137(2):EL171-177.
35. Hecht E. Optics. Third edition. New York: Addison-Wesley; 1997.
36. Cheong W, Prahl S. A review of the optical properties of biological tissues. IEEE J Quantum Elec. 1990;26(12):2166-2185.
37. Ansari MA, Massudi R, Hejazi M. Experimental and numerical study on simultaneous effects of scattering and absorption on fluorescence spectroscopy of a breast phantom. Opt Laser Technol 2009;41(6):746-750.
38. Vo-Dinh T. Biomedical Photonics Handbook. CRC Press; 2003.
39. Cheong W F. Summary of optical properties Optical-Thermal Response of Laser-Irradiated Tissue 1st edn. New York: Springer;1995.
40. Kim A, Wilson BC. Measurement of *ex vivo* and *in vivo* tissue optical properties: methods and theories Optical-Thermal Response of Laser-Irradiated Tissue 2nd edn. Welch AJ, van Gemert MJC. Berlin: Springer; 2011.
41. Sandell JL, Zhu TC. A review of in-vivo optical properties of human tissues and its impact on PDT J. Biophotonics. 2011;4:773-87
42. Bashkatov AN, Genina EA and Tuchin VV. Optical properties of skin, subcutaneous, and muscle tissues: a review J. Innovative Opt. Health Sci. 2011;4:

9-38.

43. Niemz MH. Laser-tissue interactions: Fundamentals and applications. New York: Springer-Verlag; 2007.
44. Huang YY, Aaron CH, Chen Carroll JD, Hamblin MR. BIPHASIC DOSE RESPONSE IN LOW LEVEL LIGHT THERAPY. Dose-Response.2009;7:358-383
45. Wang LV, Wu HI. Biomedical optics: principles and imaging. New Jersey: Wiley-Interscience; 2007.
46. Valero T. Mitochondrial biogenesis: Pharmacological approaches. Curr. Pharm. 2014;20:5507-09.
47. Alberts B, Johnson A, Lewis J, Raff M, Roberts K, Walter P. Molecular Biology of the Cell. New York: Garland Publishing Inc;1994. ISBN 978-0-8153-3218-3.
48. Cifra M, Fields JZ, Farhadi A. Electromagnetic cellular interactions. Prog Biophys Mol Biol. 2011;105: 223-46.
49. Karu T. Photobiology of low-power laser effects. Health Physics.1989;56:691-704.
50. de Freitas LF, Hamblin MR. Proposed Mechanisms of Photobiomodulation or Low-Level Light Therapy. IEEE J Sel Top Quantum Electron. 2016; 22(3):7000417.
51. Wang Y, Huang YY, Wang Y, Lyu P, Hamblin MR. Photobiomodulation of human adipose-derived stem cells using 810nm and 980nm lasers operates via different mechanisms of action. Biochim Biophys Acta Gen Subj. 2017;1861:441-9.
52. Prindeze NJ, Moffatt Lt, Shupp JW. Mechanisms of action of light therapy: A review of molecular interactions. Experimental Biology and Medicine.

2012;237(11):1241-1248.

53. Tonna EA, Pillsbury N. Changes in the osteoblastic and mitochondrial population of aging periosteum. Nature.1959;183:337-338.
54. Chen AC, Huang YY, Arany PR, Hamblin MR. Role of reactive oxygen species in low level light therapy. Proc. SPIE. 2009;7165:716502-11.
55. Chen, AC, Arany PR, Huang YY, Tomkinson EM, Sharma SK, Kharkwal GB, Saleem T, Mooney D, Yull EF, Blackwell TS, Hamblin MR. Low-level laser therapy activates NF-kB via generation of reactive oxygen species in mouse embryonic fibroblasts. PLoS ONE. 2011;6(7):1-8.
56. Murphy MP. How mitochondria produce oxygen species. Biochem J. 2009;417:1-13.
57. Hamblin MR. Mechanisms and applications of the anti-inflammatory effects of photobiomodulation. AMIS Biopysics. 2017;4(3):337-361.
58. Wang Y, Huang YY, Wang Y, Lyu P, Hamblin MR. Photobiomodulation of human adipose-derived stem cells using 810nm and 980nm lasers operates via different mechanisms of action. Biochim Biophys Acta. 2017;1861(2):441-449.
59. Yaneko Y, Szallasi A. Transient receptor potential (TRP) channels: a clinical perspective, Br J Pharmacol. 2014;171:2474-2507.
60. Hamblin MR. Mechanisms and Mitochondrial Redox Signaling in Photobiomodulation. Photochemistry and Photobiology.2018;94:199-212.
61. Wang L, Jacques SL, Zheng L. MCML-Monte Carlo modeling of light transport in multi-layered tissues. Comput Meth Prog Bio.1995;47:131-46.
62. Sert C. The effects of EMF (ELECTROMAGNETIC FIELDS) on the Bone and Cartilage Tissue. Nov Physiother Rehabil. 2017;1:054-055.
63. Karu TI, Afanas'eva NI. Cytochrome c oxidase as the primary photo-acceptor

upon laser exposure of cultured cells to visible and near IR-range light. Dokl Akad Nauk.1995;342:693-5.

64. Chung H, Dai T, Sharma SK, et al. The nuts and bolts of low-level laser (light) therapy. Ann Biomed Eng. 2012;40:516-33.

65. Hudson DE, Hudson DO, Wininger JM, Richardson BD, Penetration of Laser Light at 808 and 980 nm in Bovine Tissue Samples. Photomedicine and Laser Surgery. 2013;31(4):163-68

CHAPTER II

Photobiomodulation:

Current proposed mechanisms of action

2.1 INTRODUCTION

Photobiomodulation (PBM) delivered at low doses tends to produce a better effect than the same wavelength delivered at high levels, which is the concept of biphasic dose response or hormesis [1]. However, the notion has changed when a high dose of 60J/cm^2 was shown to have an optimized effect on cell proliferation and differentiation of various cells and organelles [2]. Hamblin et al., 2018 [3] and Amaroli et al., 2019 [2] suggested that the negative effect of higher fluences observed to date are not unequivocally, due to high fluence *per se* but might be a consequence of the irradiation carried by a Gaussian profile beam.

Moreover, the *in vitro* studies of this thesis, for the first time, prove the optimal effects of 980nm irradiation delivered with flattop beam profile, at high fluence of 60J/cm^2 on osteoblast maturation, in comparison to the Guassion beam profil delivery device. Moreover, we demonstrated the mechanism, affecting the intracellular and molecular activities of PBM light on osteoblasts proliferation and differentiation.
In this chapter, the proposed molecular and cellular mechanisms PBM are presented.

2.2 PHOTOBIOMODULATION (PBM) PROPOSED MECHANIMS OF ACTION

Karu et al., 2010 was the first to attribute the effects of red and near-infrared light to photon absorption, by the electron transport chain in mitochondria and by unit IV CCO in particular [4]. Since CCO has absorption peaks in the red (600-700nm) and near-infrared (NIR) (760-900nm) regions of the electromagnetic spectrum (depending on its precise oxidation state), red and NIR light have been the most often employed wavelengths for PBM [5,6]. In recent years, it has become apparent that there are other chromophores operating in different regions of the EM spectrum [7]. The most

important alternative chromophore appears to be transient receptor potential (TRP) ion channels that can be activated by light or heat [8]. An example is TRPV1 that can be activated by blue or green light [9,10] and by longer wavelength NIR light (980 nm) [11], which targets water in the form of nanostructured exclusion zone water clusters [12]. Wang et al., 2017 and co-workers study [11] showed evidence that the mechanisms of action of 810 nm and 980 nm laser appear to have significant differences. A reasonable hypothesis to explain the mechanism of action of 980 nm relies on the activation of heat (or light)-gated ion channels. However, activation of CCO in the mitochondria by 810 nm continues to be the most important and generally accepted mechanism. However, the authors of of the latter study [11] suggested further investigations to have a better understanding of the mechanism. Regardless of whether CCO is activated by red/ NIR light, or by TRP ion channels activated by blue/green/980 nm light, the cellular results have some aspects in common, while also displaying some differences. Both pathways give rise to increased ATP and a brief burst of reactive oxygen species (ROS) [13]. However, the CCO pathway is more likely to lead to a release of nitric oxide (NO), while the TRP pathway is more likely to give rise to changes in cytosolic and mitochondrial calcium levels. The secondary effects of PBM can be a short term in nature, such as increased in the blood flow, greater oxygen consumption, and improved tissue ATP production. They can also be more a long term in nature such as; increased antioxidant defenses, activation of transcription factors, and alteration of the expression pattern of cytokines and growth factors.

The proposed PBM mechanisms of action are as follows (Figure 1) [14]: one of the most important chromophores is CCO (Unit IV in the mitochondrial respiratory chain), which contains both heme and copper centers and absorbs light into the NIR

region. The leading hypothesis is that the photons dissociate inhibitory NO from the enzyme, leading to an increase in electron transport, mitochondrial membrane potential (MMP), and ATP production. Another hypothesis concerns the light-sensitive ion channels that can be activated, allowing calcium (Ca^{2+}) to enter the cell. After the initial photon absorption events, numerous signaling pathways are activated via ROS, cyclic adenosine monophosphate (cAMP), NO, and Ca^{2+}, leading to activation of transcription factors. The latter can lead to increased expression of genes related to protein synthesis, cell migration and proliferation, anti-inflammatory signaling, anti-apoptotic proteins, and antioxidant enzymes. The stem cells and progenitor cells appear to be particularly susceptible to PBM light. The relevant chromophores can be identified by matching the action spectra for the biological response to the light in the NIR range and the absorption spectra of the four membrane bound-complexes identified in the mitochondria [15]. Complex IV is also called the CCO, which is a crucial chromophore in the cellular response to photobiomodulaion. The CCO is a large transmembrane protein complex, consisting of two copper centers and two heme-iron centers, which is a component of the respiratory transport electron chain [16].

The precise mechanism by which light affects CCO is not yet known. The release of NO from cells during PBM has led to speculation, that CCO and NO release are linked via two possible pathways. Figure 2 shows the two possible sources of NO release, as follows: the first path shows the CCO can act, as a nitrate redutase enzyme; the second path shows possible dissociation of NO from CCO [14,17].

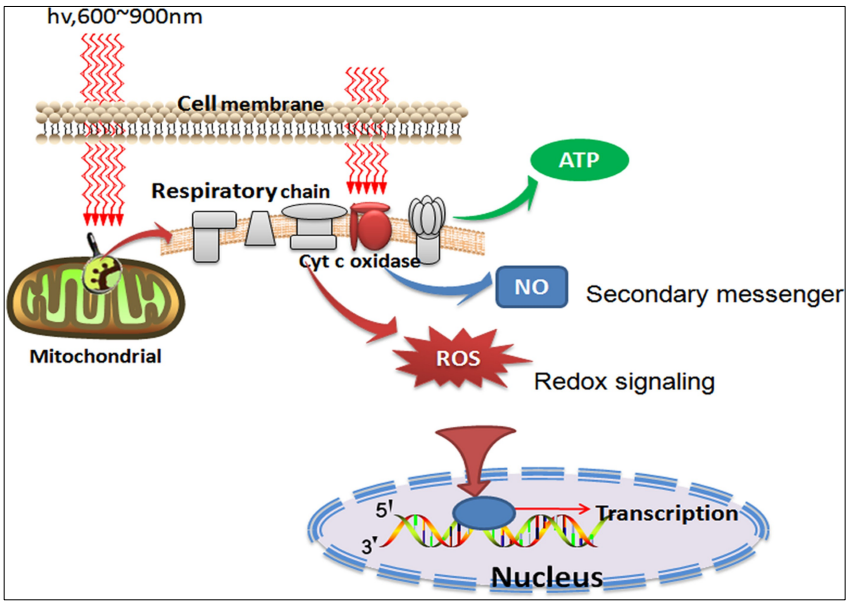

Figure: 1: Schematic description of the cellular signaling pathways triggered by PBMT. After photons are absorbed by chromophores in the mitochondria, respiration and ATP is increased but in addition signaling molecules such as reactive oxygen species (ROS) and nitric oxide (NO) are also produced. [14]

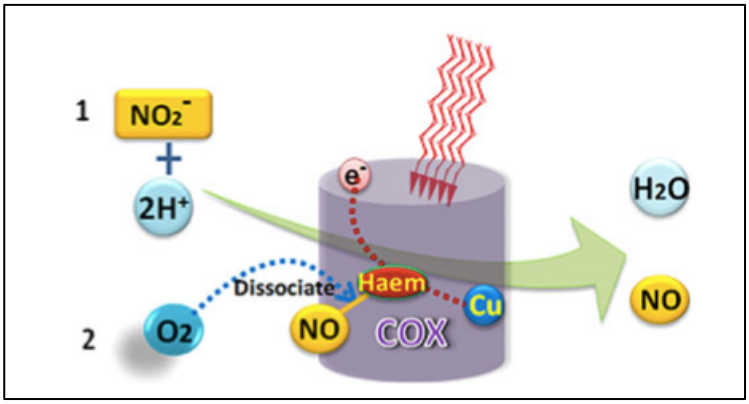

Figure 2: Schematic description of the two possible pathways of NO release. One possible theory that can explain the simultaneous increase in respiration and production of nitric oxide (NO) is the photodissociation of bound NO that is inhibiting cytochrome c oxidase (CCO) by displacing oxygen [14].

Cyclooxygenase (COX) is the terminal enzyme of the electron transport chain of the mitochondria, mediating the electron transfer from cytochrome c to molecular oxygen. Several lines of evidence show that COX acts as a photoacceptor and transducer of photo-signals in the red and NIR regions of the light spectrum [4]. It seems that PBM increases the availability of electrons for the reduction of molecular oxygen in the catalytic center of COX, increasing the MMP, ATP, and cAMP levels, as well as and ROS [18].

It is important to report that the precise biochemistry mechanism underlying the therapeutic effects of PBM is not yet well established. Studies have shown that PBM have a great impact on the cellular, molecular and tissue levels. The mode of action varies among various applications. There is a strong evidence to suggest that PBM acts on the mitochondria within the cell [19].

2.3 CONTRIBUTION OF THE MITOCHONDRIA TO RED AND NEAR INFRARED (NIR) LIGHT.

In PBM, three mechanisms at discrete cellular sites have been identified for their interactions with photoreceptive targets. While an individual mechanism appears to dominate specific therapeutic applications related to performance and analgesic versus regenerative responses. It is increasingly evident that there is a significant crosstalk amongst them, in the individual clinical situations (Figure 3). These mechanisms have been described-mainly, inside the cell (CCO within the mitochondria), at the cell membrane (photosensitive receptors and ion transporters like Opsins, TRPV1), and extracellular matrix (activation of latent TGF-β1) [11, 20-23]

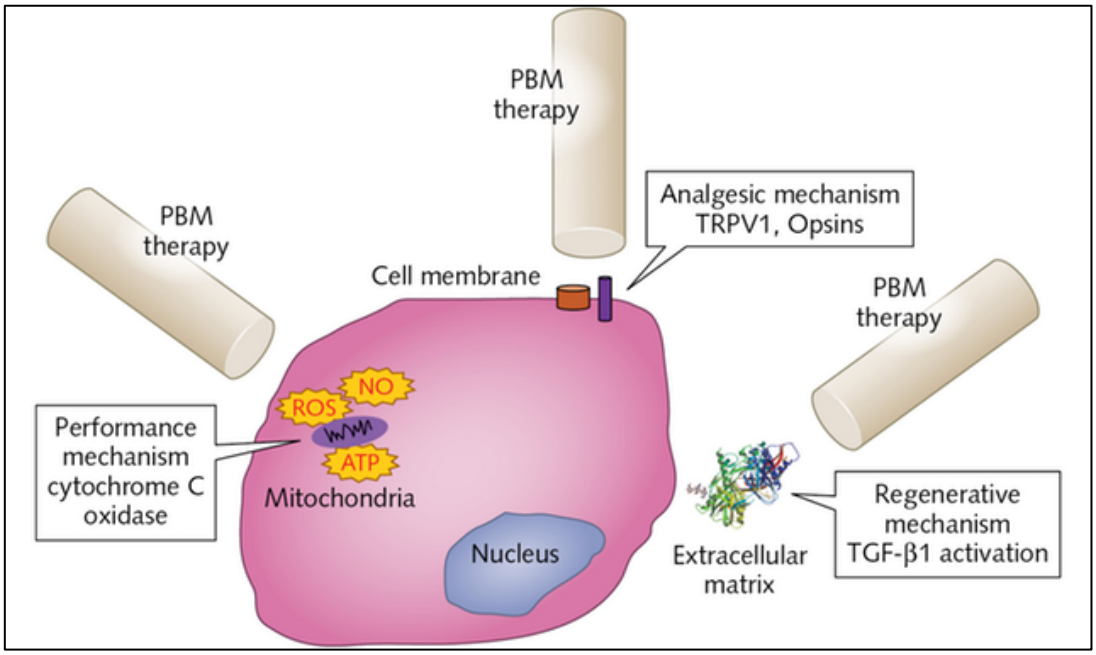

Figure 3: The three discrete PBM mechanisms of action.
(www.laserfocusworld.com/lasers-sources/article/14037967)
Abbreviations: TRPV1: Transient receptor potential cation channel subfamily V member1, TGF-β: Transforming Growth Factor beta, PBM: photobiomodulation, ROS: Reactive oxygen species, NO: Nitric oxide, ATP: Adenosine triphosphate

2.3.1 PBM effect on mitochondria and gene transcript

The mitochondrial response, at the beneficial range of light dosages, involves increase of electron transport, oxygen consumption, mitochondrial membrane potential and synthesis of ATP. Excessively large doses of light can have quite the opposite effects on these mitochondrial measurements. While increased mitochondrial activity and more ATP can benefit tissues that are hypoxic and stressed. Modern biological research suggests that the signaling and activation of transcription factors are needed to have a long-lasting effect on healing and tissue repair after the light has been switched off (Figure 4) [24]. One important factor that is often involved in the signaling pathways observed after PBM is a brief burst of ROS. These ROS appear to

be generated in the mitochondria after activation of the electron transport chain. Figure 5 summarizes the signaling pathways activated after PBM [17]. When NO is released from its binding to heme iron and copper centers in CCO by the action of light, oxygen is allowed to rebind to these sites and respiration is restored to its former level, leading to an increase in the ATP synthesis [17].

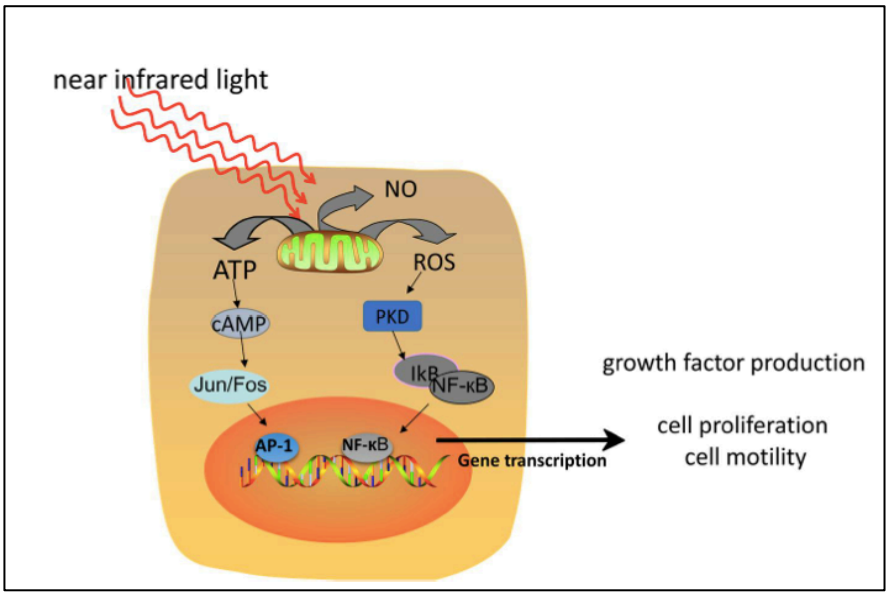

Figure 4: The PBM mechanism of action and gene transcripts [24].

2.3.2 Cellular responses to light

After light absorption by CCO, changes in the energy homeostasis inside the mitochondria and cell occur. One consequence is the retrograde signaling between the mitochondria and cellular nuclei. Thus, the retrograde signaling monitors the cellular energy homeostasis by a constant communication from the mitochondria to the nuclei reporting the mitochondria.

The growth factor response within cells and tissues may be seen, as a result of an increase in the ATP and protein syntheses [25], change in the cell membrane permeability to Ca^{+2} uptake and in the cell proliferation. Ultimately, the overall cascade of metabolic effects results in physiological changes, leading to an

improvement in the tissue repair, faster resolution of the inflammatory response and a reduction in pain [26]. The results of laser-tissue interaction that promote PBM can be seen within three clinical areas of benefit; anti-inflammatory effects [27], analgesic and pain suppression effects [28] and enhancing and accelerating tissue repair [29], which was investigated in this thesis (Chapter V, Phase I &II).

The photochemistry of CCO has been extensively characterized by Karu et al., 1995 [30] specifically, it contains four redox metal centers: CuA, CuB, Hem a, and Hem a3 as shown in figure 2. These Cu elements are able to absorb the light in the red to NIR spectrum [17], in particular reference to 670 nm, which increases the oxidation of cytochrome *c*, boosts the transfer of electrons, increases the oxygen consumption and mitochondrial membrane potential. It is highly correlated with peaks in COX catalytic activity and ATP content observed *in vivo* study [31]. The secondary effects occur, as a consequence of the primary effect described above. These include a cascade of downstream biochemical reactions, which change the cellular homeostasis. While the secondary effects are pleiotropic and can occur hours or days after laser light exposure. The initial phase of the secondary mechanisms, after light exposure, is characterized by an increase in the NAD^+/NADH ratio and mitochondrial membrane potential, dissociation of nitric oxide from cytochrome *c* oxidase complex and an increase in the ATP pool [22]. The change in the latter significantly alters the cellular metabolism. Finally, all these secondary effects activate the retrograde signaling between the mitochondria and nuclei [31,32].

It is important to mention, changes that occur in the tissues in response to the light absorption by the above chromophores. These may take place in a relatively short period of time (minutes and hours) or in a long term (days and weeks). Examples of

short-term effects are due to NO release (Vasodilation), an increase in the blood flow, an improvement in the oxygenation, and analgesic effects. While the examples of long-term effects are wound healing, reduction in inflammation, regeneration and repair of damaged or degraded tissues, and stimulation of stem cells. One hypothesis to explain these long terms beneficial effects, suggests that, they are part of the protective response, which is switched on by the cell's perception of the mitochondrial effects and upregulating of the cell survival and repair pathways [33].

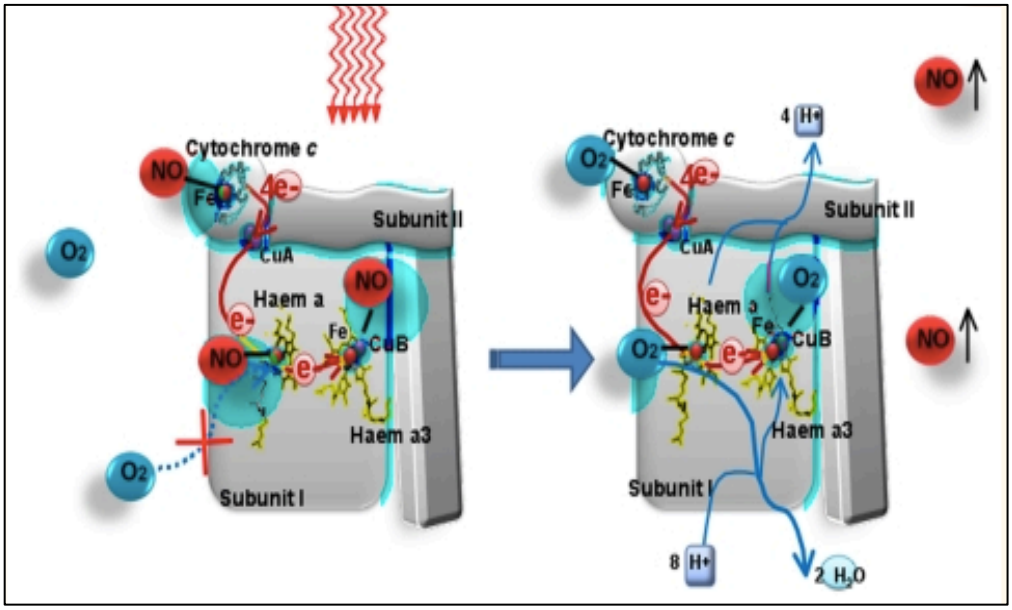

Figure 5: The release of NO binding to the heme iron and copper centers in CCO though the action of PBM [17].

2.4 CRTICAL FACTORS INFLUENCING THE PBM THERAPEUTIC EFFECTS

The influencing factors that have a great impact on optimization of the PBM therapeutic outcomes are related to both biological and clinical considerations [34], which are summarized in figure 6.

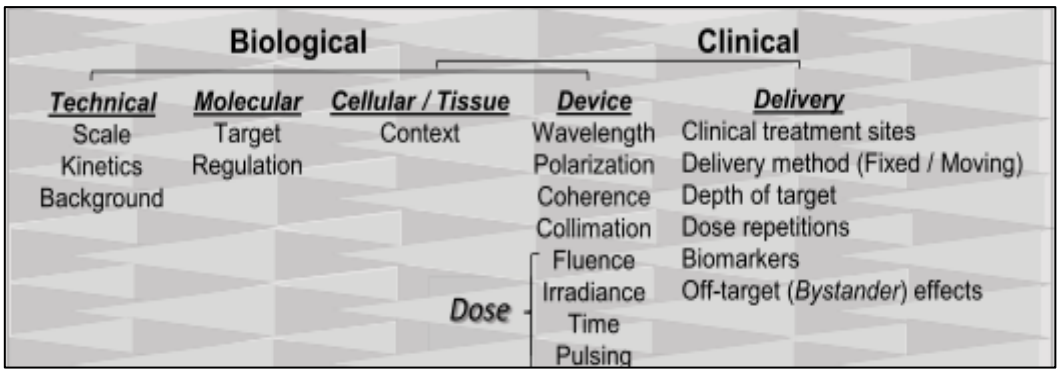

Figure 6: The critical issues that required consideration in PBMT [34]

2.4.1 Dose response

The exact mechanism of biphasic dose-response is not known, but it might be related to excessive formation of ROS. Huang et al., 2011 [14] suggested that the *"nature of ROS may act as a beneficial signaling molecule, at low concentrations and a harmful cytotoxic agent at high concentrations, may partly explain the observed responses in vivo studies".* In some cases, very high dosages can even have a negative effect, which is sometimes said to be on the inhibitory side of the Arndt-Schulz curve (Figure 7) for the biphasic dose response [35]. The biological responses of PBM classically evoke a nonlinear biphasic response referred to as the Arndt-Schulz law. These responses demonstrate a linear optimal threshold that, on continued stimuli, results in negative or inhibitory effects (Figure 8). This phenomenon potentially arises due to several factors, such as the nonlinear physical process of multi-photons interactions and the inelastic scattering or presence of tightly regulated biological feedback regulation. These nonlinear responses are well documented in the biological phenomenon by the term *"hormesis"* (Figure 8) [36].

It is well established that if the light applied is not of sufficient irradiance or the irradiation time is too short, then there is no response. If the irradiance is too high or irradiation time is too long, then the response may be inhibited [37,38]. Indeed, the

existence of the biphasic dose response has been held responsible for the publication of a number of negative studies, where it is highly likely that the results would have been positive if different parameters had been employed [39].

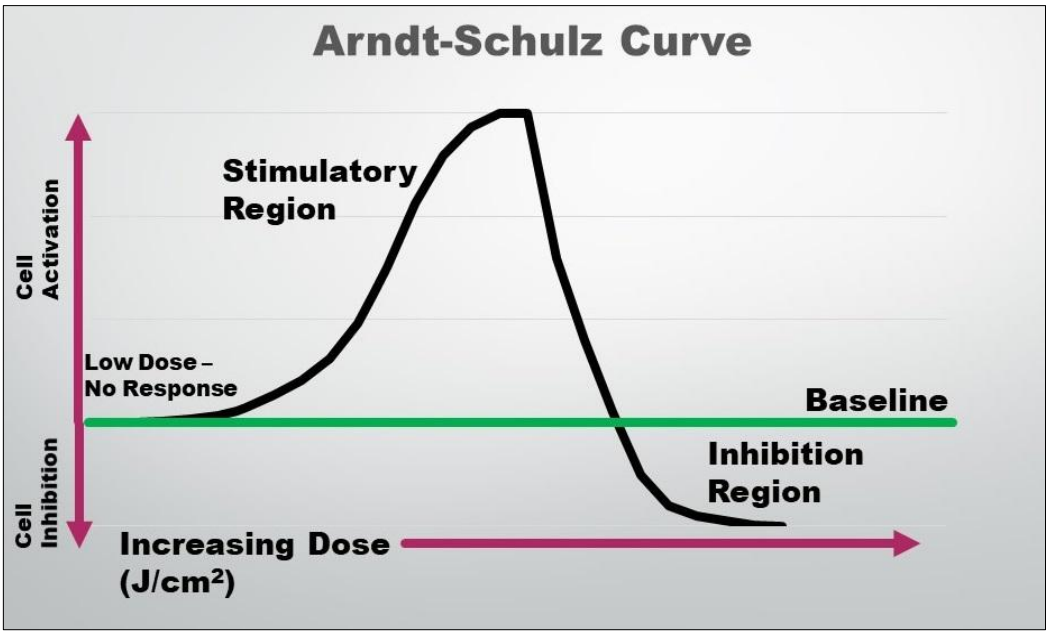

Figure 7: The Arndt-Schulz law curve (Biphasic dose response curve) [14]

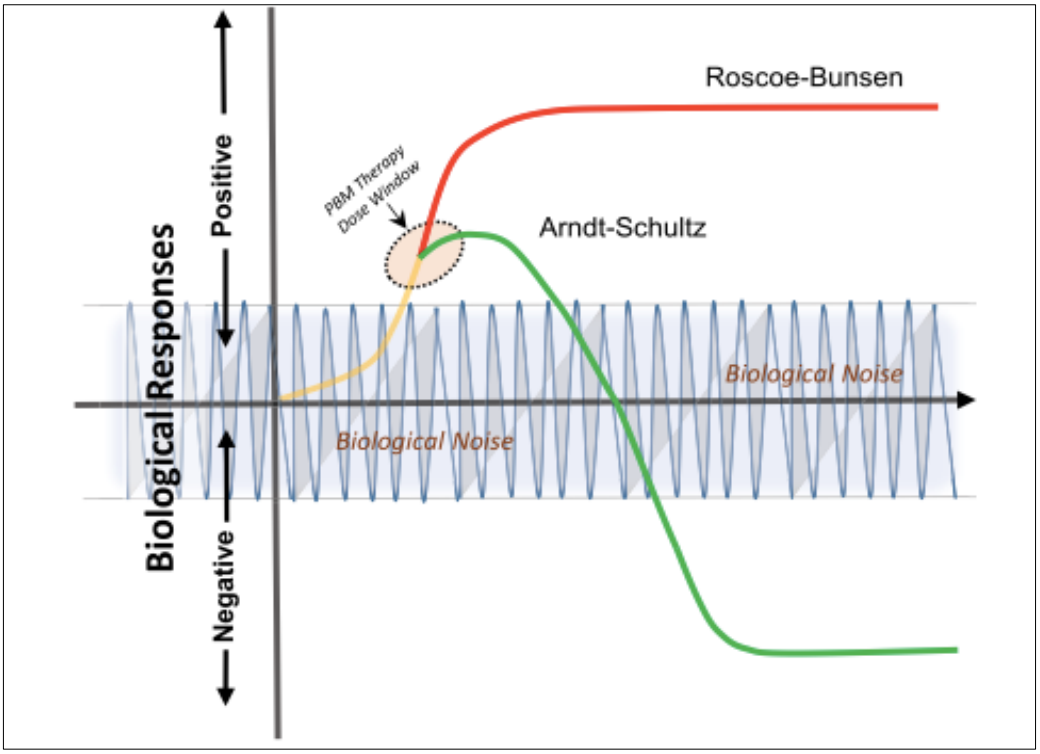

Figure 8: Dose-response curves of classical (linear) versus hormetic (non-linear) photobiological responses [34].

The ineffectiveness of overdosing has also been demonstrated, especially in many experimental studies [14]. Thus, biphasic dose-response appears to be a very significant factor in PBM. However, the mechanistic sequence of secondary events of the PBM mechanism of action (Hour-days) is to date contradictory and confused, as there is a lack of standardisation of the experimental studies and the focus was on the macroscopic phenomenological effects [33]. This has been demonstrated in the Deana et al., 2018 systematic review, which has shown that the osteoblasts-like cells were responsive to the effects of the PBM. However, different authors have varied most of the laser parameters utilised in this literature review's studies. This has led to little to none influence on proliferation of the cells, whilst the high irradiance has demonstrated deleterious effects on the proliferation of the cells [40]. Equally,

Arany et al., 2016 highlighted the heterogeneity in the current PBM studies on enhancing osteogenesis, due to inappropriate utilization of the laser device, unsuitable methods of investigations, and inefficient laser beam profile, can essentially result in undesirable effects, perhaps accounting for many negative results and inconclusive results outcome (Figure 8). Amaroli et al., 2016 and 2019 studies [2,41-42 respectively] have shown that reconsideration for a higher-fluence with a higher-energy should be addressed, due to the advances in the field of the biophotonic technologies, in utilizing the flattop (FT) profile delivery system [43] (Figure 9), instead of the Gaussian profile (Standard (ST) hand-piece) (Figure 10) [44].

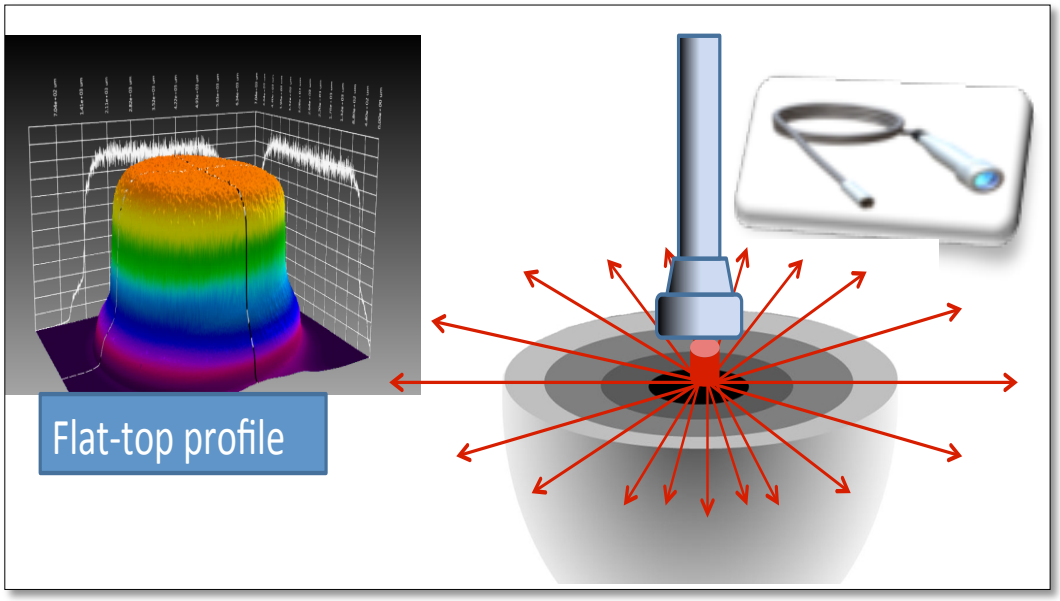

Figure 9: The flattop beam profile delivery device (Top right photo: AB2799FT flattop beam device). The red arrows in the schematic diagram, bottom right show the uniform distribution of the phonic energy, delivered by flattop beam profile, across an area of 1cm^2 [43].

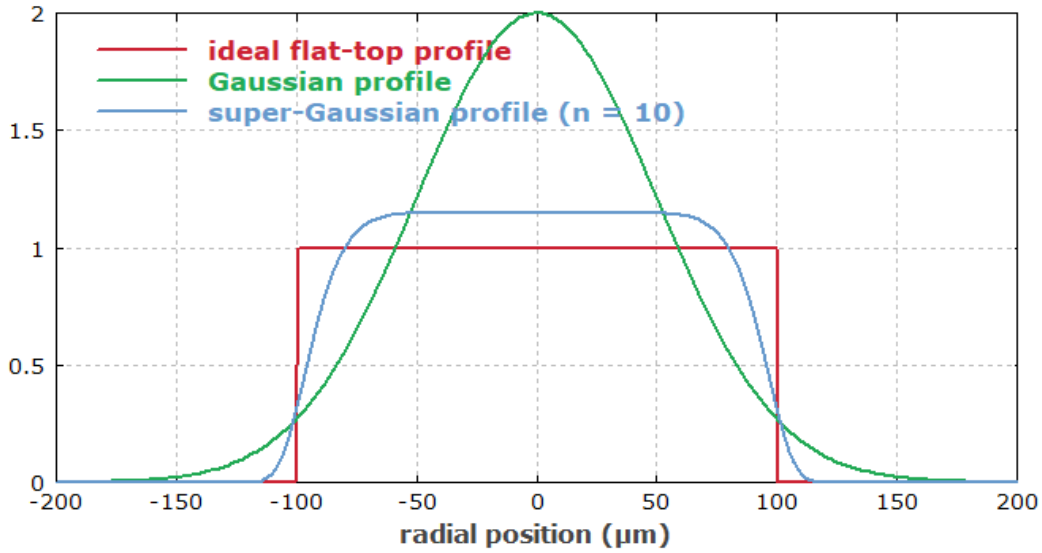

Figure 10: A flattop beam profile (red) in comparison to a Gaussian (green) and super-Gaussian (blue) intensity profile. All three beams have the same optical power and the same effective mode area [44].

As a matter of fact, studies have shown that unicellular model irradiation, *Paramecium primaurelia,* with 808 nm wavelength, using a FT profile delivery system (AB2799 FT) (Figure 9) at a power output setting of 1 W over an area of 1 cm^2 for 60 seconds (s) exposure time (Irradaince 1W/cm^2, fluence 60 J/cm^2) in continuous wave (CW) mode, has positive effects on the cell and tissue metabolism [45]. This occurred by stimulating the mitochondria's activities such as; oxygen consumption, ATP production [46], calcium fluxes [47], and nitric oxide production. Additionally, the cell proliferation in *Paramecium primaurelia* observed [48].

Amaroli et al., 2019 [2] and Hamblin et al., 2018 [3] suggested that the negative effect of higher fluences observed to date are not unequivocally due to high fluence *per se* but might be a consequence of the irradiation carried by ST profile of the hand-piece.

The *in vitro* studies of this thesis, confirmed the great effects of the FT profile irradiation at a higher fluence on osteoblast maturation, in comparison to the ST

profile. In the context of the dose, it is important to point out that utilization of therapeutic irradiance is crucial to optimize the clinical outcome. In literature, there are several conflicting results of various *in vitro* and *in vivo* studies in bone regeneration, due to lack of standardized protocols or poorly laser parameter documentation and whether power meter was utilized to measure the threshold power, arriving at the target or not. In this context, a consideration to the absorption and scattering phenomena is required, as they are crucial in achieving the optimal therapeutic outcome of PBM [49]. In this thesis, the electromagnetic study (Chapter III) showed that the biomolecular interactions with the EM radiation is a challenge, due to the complexity of the tissue on multiscale level, and the presence of different types of molecules in the tissue, leading to the difficulty in examining the behavior of the light attenuation. However, our simple EM model, for the first time, has managed to increase the knowledge and explain the 980nm light behavior on the mitochondrion. Moreover, in our *in vitro* studies (Chapter V), we have employed the power meter to measure the threshold power arriving at the cells delivered by two beam profiles (Gaussian and flattop). The other factors that play a major role in optimizing the effects of PBM are exposure time, time interval (frequency) and treatment duration.

2.4.2 Wavelength

Choosing the correct wavelength for the target cells/chromophores must be employed, to ensure the therapeutic results, otherwise the optimum absorption of the photonic energy does not occur. According to the first law of photobiology, light absorption requires the presence of a specific photoacceptor, which could induce the activation of downstream signaling pathways after excitation. Photobiomodulation operates in the red/NIR of the EM spectrum, induces biostimulatory effects in several therapeutic

applications [50]. This range of wavelengths can penetrate deeper-seated tissues [51,52]. The wavelength of a therapeutic source, therefore, has a double importance, explicitly to ensure absorption of the incident photons in the target chromophores and to be able to do so, at the depths at which these chromophores exist.

2.4.3 Laser beam properties

The ideal laser beam profile needs to be monochromatic, temporally coherent, and with uniform spatial power or energy distribution [53]. Many studies, *in-vitro* and *in-vivo*, investigated this concept, using the Gaussian beam profile when the photonic energy of various wavelengths was delivered to the target tissue. Gaussian beam profile (Figure 11) that has specification, in delivering the maximum energy density (J/cm^2) in the center, and decreases dramatically towards the periphery of target site area (Figures10,11) [43,54]. This can contribute drastically to the outcome discrepancy. Therefore, in this thesis research project, for the first time, we utilized another device, which has a flattop beam profile delivering a homogenous distribution of the energy density over 1 cm^2 surface area of the target tissue (Figures 9,12) [43,54]. Coherent light produces speckles, which has been postulated to play an important role in the PBM interaction with the cells and subcellular organelles. The size of the speckle patterns coincides with the size of the dimensions of the organelles such as mitochondria. Moreover, it has been speculated that the intensity produced by the speckles may help to improve the clinical outcome especially in deep-seated tissues, where irradiance is low. However, no definitive trials have been published to date to confirm or disapprove this claim [55,56].

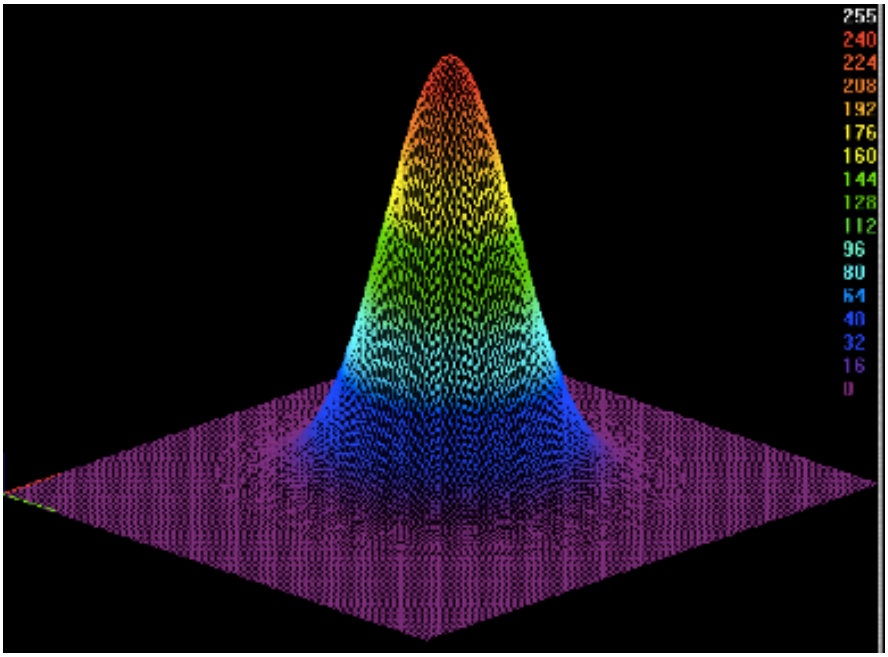

Figure 11: Gaussian beam profile for highest energy concentration [54]

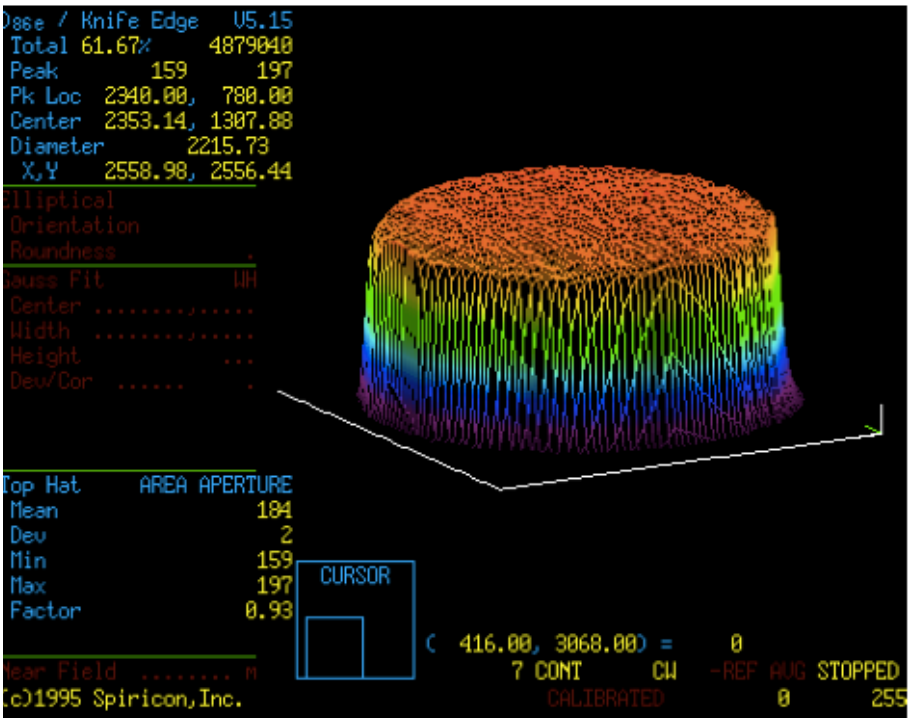

Figure 12: Flattop beam profile for uniform laser illumination [54]

2.5 REFERNCES

1. Calabrese EJ. The future of hormesis: where do we go from here? Crit Rev Toxicol. 2001b;31:637-48
2. Amaroli A, Ferrando S, Benedicenti S. Photobiomodulation affects key cellular pathways of all life-forms: considerations on old and new laser light-targets and the calcium issue. Photochem. Photobiol. 2019;95:455-9.
3. Hamblin MR, Huang YY, Heiskanen V. Non-mammalian hosts and photobiomodulation: do all life-forms respond to light? Photochem Photobiol. 2018;95:126-39
4. Karu TI. Multiple roles of cytochrome c oxidase in mammalian cells under action of red and IR-A radiation. IUBMB Life. 2010;62:607-610.
5. Chung H, Dai T, Sharma SK, Huang YY, Carroll JD, Hamblin MR. The nuts and bolts of low-level laser (light) therapy. Ann. Biomed. Eng. 2012;40:516-533.
6. de Freitas, LF, Hamblin MR Proposed mechanisms of photobiomodulation or low-level light therapy. IEEE J. Sel. Top. Quantum Electron.2016;22:1-37.
7. Hamblin MR. Mechanisms and mitochondrial Redox signaling in photobiomodulation. Photochem. Photobiol. 2017;94:199-212.
8. Jeronimo R, Moraes MN, de Assis LVM, Ramos BC, Rocha T, Castrucci AML. Thermal stress in Daniorerio: A link between temperature, light, thermo-TRP channels, and clock genes. J. Therm. Biol.2017;68:128-138.
9. Wang Y, Huang YY, Wang Y, Lyu P, Hamblin MR. Photobiomodulation (blue and green light) encourages osteoblastic-differentiation of human adipose-derived stem cells: Role of intracellular calcium and light-gated ion channels. Sci. Rep. 2016;6:1-9.

10. Wang Y, Huang YY, Wang Y, Lyu P, Hamblin MR. Red (660 nm) or near-infrared (810nm) photobiomodulation stimulates, while blue (415 nm), green (540 nm) light inhibits proliferation in human adipose-derived stem cells. Sci. Rep. 2017;7(1):1-10.
11. Wang Y, Huang YY, Wang Y, Lyu P, Hamblin MR. Photobiomodulation of human adipose-derived stem cells using 810 nm and 980 nm lasers operates via different mechanisms of action. Biochim. Biophys. Acta 2016;1861(2):441-449.
12. Chai B, Yoo H, Pollack GH. Effect of radiant energy on near-surface water. J. Phys. Chem. B. 2009;113;13953–13958.
13. Hamblin MR. Mechanisms and mitochondrial Redox signaling in photobiomodulation. J. Photochem. Photobiol. 2017;94:199-212
14. Huang YY, Sharma SK, Carroll JD, Hamblin MR. Biphasic dose response in low level light therapy-an update. Dose Response. 2011:9:602–618
15. Karu TI. Photobiological fundamentals of low power laser therapy. IEEE J. Quantum Electron. 1987;23:1703-1717.
16. Capaldi RA, Malatesta F, Darley-Usmar VM. Structure of cytochrome c oxidase. Biochim. Biophys. Acta.1983;726:135-148 .
17. Huang YY, Sharma SK, Carroll JD, Hamblin MR. BIPHASIC DOSE RESPONSE IN LOW LEVEL LIGHT THERAPY. Dose-Response.2009;7:358-383
18. Wu S, Zhou F, Wei Y, Chen WR, Chen Q, Xing D, "Cancer phototherapy via selective photoinactivation of respiratory chain oxidase to trigger a fatal superoxide anion burst," Antioxid. Redox Signal. 2014; 20(5):733-746.

19. Greco M, Guida G, Perlino E, Marra E, Quagliariello E. Increase in RNA and protein synthesis by mitochondria irradiated with helium-neon laser. Biochem. Biophys. Res. Commun.1989;163:1428-1434.
20. Arany PR, Cho A, Hunt TD, Sidhu G, Shin K, Hahm E, Huang GX, Weaver J. Photoactivation of endogenous latent transforming growth factor-beta1 directs dental stem cell differentiation for regeneration. Sci. Transl. Med.2014;6:ra238-269
21. Buscone S, Mardaryev AN, Raafs B, Bikker JW, Sticht C, Gretz N, Farjo N, Uzunbajakava NE. A new path in defining light parameters for hair growth: Discovery and modulation of photoreceptors in human hair follicle. Lasers Surg. Med. 2017;49(7):705-718
22. Karu TI, Kolyakov SF. Exact action spectra for cellular responses relevant to phototherapy. Photomed. Laser Surg. 2005;23(4):355–361
23. Yim PD, Gallos G, Perez-Zoghbi JF, Zhang Y, Xu D, Wu A, Berkowitz DE, Emala CW. Airway smooth muscle photorelaxation via opsin receptor activation. Am J Physiol Lung Cell Mo.l Physiol. 2019;316(1):L82-L93
24. Hamblin MR, de Sousa MVP; Arany, Carroll JD, Patthoff D. "Low level laser (light) therapy and photobiomodulation: the path forward", Proc. SPIE 2015; 9309(930902):1-11
25. Amaroli A, Parker S, Dorigo G, Benedicenti A, Benedicenti S. Paramecium: a promising non-animal bioassay to study the effect of 808 nm infrared diode laser photobiomodulation. Photomed Laser Surg. 2015;33(1):35–40.
26. Matic M, Lazetic B, Poljacki M. Low level laser irradiation and its effect on repair processes in the skin. Med Pregl. 2003;6:137-41.

27. Carroll J, Milward M. Developments in low level light therapy (LLLT) for dentistry. Dent Mater. 2014;30(5):465–75
28. Pohlhaus S. Dental laser utility expanding as research supports innovation. Compend Contin Educ Dent. 2015;36(1):68–9
29. Sperandio F, Simões A, Corrêa L, Aranha A, et al. Low-level laser irradiation promotes the proliferation and maturation of keratinocytes during epithelial wound repair. J Biophotonics. 2015;8(10):795–803.
30. Karu TI, and Afanas'eva NI. Cytochrome c oxidase as the primary photoacceptor upon laser exposure of cultured cells to visible and near IR-range light. Dokl. Akad. Nauk.1995;342:693–695.
31. Karu, TI. Primary and secondary mechanisms of action of visible to near-IR radiation on cells. J. Photochem. Photobiol. B.1999;49:1-17.
32. Karu TI, Pyatibrat VL, Kalendo GS. Irradiation with He-Ne laser increases ATP level in cells cultivated in vitro. J. Photochem. Photobiol. B 1995;27:219-223.
33. Agrawal T. Pre-conditioning with low-level laser (light) therapy: light before the strom, "Dose Response. 2014;12:619-649
34. Arany PR. Craniofacial Healing with Photobiomodulation Therapy: Insights and Current Challenges. Journal of Dental Research 2016;95(9):1-8
35. Sommer AP, Pinheiro AL, Mester AR, Franke PR, Whelan HT. Biostimulatory windows in low-intensity laser activation: lasers, scanners, and NASA's light-emitting diode array system. J. Clin. Laser Med. Surg. 2001;19:29-33.
36. Calabrese EJ, Bachmann KA, Bailer AJ, Bolger PM, Borak J, Cai L, Cedergreen N, Cherian MG, Chiueh CC, Clarkson TW. Biological stress response terminology: integrating the concepts of adaptive response and preconditioning stress within a hormetic dose-response framework. Toxicol Appl Pharmacol.

2007;222(1):122-128.

37. Haxsen V, Schikora D, Sommer U, Remppis A, Greten J, Kasperk C. Relevance of laser irradiance threshold in the induction of alkaline phosphatase in human osteoblast cultures. Lasers Med. Sci. 2008;23:381-384.
38. Lanzafame RJ, Stadler I, Kurtz AF, Connelly R, Peter TA,. Brondon P, Olson D. Reciprocity of exposure time and irradiance on energy density during photoradiation on wound healing in a murine pressure ulcer model. Lasers Surg. Med. 2007;39:534-542.
39. Tunér J1, Hode L. It's all in the parameters: a critical analysis of some well-known negative studies on low-level laser therapy. J Clin Laser Med Surg.1998;16(5):245-8.
40. Deana AM, de Souza AM, Teixeira VP, Mesquita-Ferrari RA, Bussadori SK, Fernandes KPS. The impact of photobiomodulation on osteoblast-like cell: a review. Lasers Med Sci. 2018;33(5):1147-1158.
41. Amaroli, A., S. Ravera, S. Parker, I. Panfoli, A. Benedicenti and S. Benedicenti 808-nm laser therapy with a flat-top handpiece photobiomodulates mitochondria activities of Paramecium primaurelia (Protozoa). Lasers Med. Sci.2016;31:741-747.
42. Amaroli A, Ravera S, Parker S, Panfoli I, Benedicenti A, Benedicenti S. An 808-nm diode laser with a flat-top handpiece positively photobiomodulates mitochondria activities. Photomed Laser Surg.2016;34:564-71.
43. Benedicenti S and Benedicenti A. An Atlas of laser therapy. Fourth edition, (State of art). Italy: Peter Asselmann; 2016. ISBN 88-89626-02-X.

44. Paschotta R. Flat-top beams. Encyclopedia of Laser Physics and Technology. First edition. New Jersey, USA: Wiley-VCH; 2008. ISBN 978-3-527-40828-3.
45. Amaroli, A, Ravera S, Parker S, Panfoli I, Benedicenti A, Benedicenti S. The protozoan, Paramecium primaurelia, as a non-sentient model to test laser light irradiation: The effects of an 808 nm infrared laser diode on cellular respiration. Altern. Lab. Anim. 2015;43:155-162.
46. Amaroli A, Ravera S, Parker S, Panfoli I, Benedicenti A, Benedicenti S. An 808-nm diode laser with a flat-top handpiece positively photobiomodulates mitochondria activities. Photomedicine and Laser Surgery. 2016;34(11):1-8.
47. Amaroli A, Benedicenti A, Ferrando S, Parker S, Selting W, Gallus L, Benedicenti S. Photobiomodulation by infrared diode laser: Effects on intracellular calcium concentration and nitric oxide production of paramecium. Photochem. Photobiol. 2016;92:854-862.
48. Amaroli, A, Parker S, Dorigo G, A. Benedicenti A, Benedicenti S. *Paramecium*: A promising non-animal bioassay to study the effect of 808 nm infrared diode laser photobiomodulation. Photomed. Laser Surg. 2015;33:35-40.
49. Hecth E. Opitcs. 4th edition. Boston, USA: Addison-Wesley;2002
50. Migliario M, Sabbatini M, Mortellaro C, Renò F. Near infrared low-level laser therapy and cell proliferation: The emerging role of redox sensitive signal transduction pathways. J Biophotonics. 2018;11(11):1-7.
51. Niemz MH. Laser-Tissue Interactions: Fundamental and Applications.2004
52. Hudson D, Hudson DO, Wininger J, Richardon BD. Penetration of Laser Light at 808 and 980 nm in Bovine Tissue Samples. Photomedicine and Laser Surgery 2013;32(4):163-168.

53. Shealy DL, Hoffnagle JA. Laser beam shaping profiles and propagation. Applied Optics. 2006;45(21):5118-31.

54. Rosenzweig JB. Fundamentals of Beam Physics. UK: Oxford University Press; 2003. ISBN:9780198525547

55. CorazzaAV. Photobiomodualtion on angiogenesis of skin wounds in rats using different light sources". Photomed Laser Surgery 2007;25(2):102-06.

56. Zalevsky Z, Belkin M. Coherence and spekle in photomedicien and photobiology. Photomed and Laser Surgry. 2011;29(10):655-56.

CHAPTER III

Electromagnetic models

(Experimental setup)

3. 1 INTRODUCTION

3.1.1 Electromagnetic modeling

Mathematical modeling creates a mathematical representation of reality that attempts to explain the behavior of some aspect of it, based on simplifying assumptions (hypotheses). The mathematical representation usually resides in a set of variables and equations, in order to establish relationships between these variables. The mathematical model can serve several purposes: answer a variety of what-if questions, understand the relationships between variables, and extrapolate past data to derive meaning. Models are typically utilized when it is either; impossible or impractical to create experimental conditions for scientists to measure directly the outcomes. However, even when experiments are possible, obtaining a good mathematical model is usually very useful, as it can provide insights into the internal workings of a system. In electromagnetic (EM) field research, large efforts have been invested to construct mathematical models. Recently, researchers have been trying to extend such models to compute EM fields inside living organisms. Such models of the human body cannot usually be solved, using a *"pencil and paper"* approach: they require computer programs to breakdown the body into many simple geometrical shapes (for example little cubes), in which mathematical equations can be solved.

The analysis of light propagation and the EM characterization of a heterogeneous medium, such as bone tissue, are very complex. A number of simple available methods can be applied to a homogeneous, linear and isotropic medium, which is not the case with bone tissue. Therefore, the model that we adopted in our experiments would be the first time to understand the propagation of an EM field (EMF) in such biological tissue. The distribution of EMF in the biological tissues depends on its absorption and scattering, which in turn depends significantly on the employed

wavelength and properties of the tissue (Power, energy and time do not affect distribution. While they affect intensity at any specific point in the tissue, that can only be calculated after distribution is known). An exact assessment of laser propagation in a tissue requires a model that characterizes the spatial distribution of photons in the tissue structure, their absorbing properties, and refractive indices. The refractive index (RI) of a biological tissue is a key parameter for characterizing the light-tissue interactions [1,2]. Knowledge of the tissue RI plays an important role in many biomedical applications.

An understanding of light propagation in a tissue and the information content of the elastically or in-elastically scattered light from tissues is mandatory for a successful realization of the potential of these optical approaches, and in achieving quality health care. It is pertinent to note here, that for modeling light propagation in tissue usually a homogenous tissue is assumed. However, many tissues of interest, especially bone, cannot be considered homogeneous and are in fact multilayered [3]. Therefore, it can be appreciated that developing a model, in order examine the optical properties of complex, non-homogenous, anisotropic tissues such as bone [4], is quite challenging. Moreover, the literature provides some information on the homogeneous single layer model, but more of the demanding clinical applications require multilayered photon propagation models. Therefore, for the time, we examined the behavior of light propagation on illuminated mitochondrion. The latter is the main photoaccpetor of the photonic energy of photobiomodulation light, to generate a cascade of biological and molecular activities, which optimize tissue regeneration.

3.1.2 Photobiomodulation (PBM) and EM simulations

PBM was initially developed 50 years ago, as a very promising therapeutic procedure and nowadays its importance is well established. This due to its beneficial effects in inflammation reduction, promote wound healing and tissue repair [5,6]. Despite extensive studies on the benefits of PBM therapy [7], the mechanism of interaction [8], between the features of the field emitted by the light source, and the description of the measurement for various cells in vitro studies, and in vivo animal experiments, remain scattered [6,9]. It has been observed that in order to understand what is going on inside the cells, showing PBM effects as a consequence of NIR illumination, it is necessary to have a better knowledge of the EMF inducing biological reactions [8]. This is a challenging problem, due to some experimental evidence [9,10] related to specific multi-protein complexes inside the mitochondria [11] of eukaryotic cells [12] where the molecular activation take place. Therefore, the problem is considered as a multi-scale one, extending over dimensions of a few millimeters or centimeters for *in vitro* studies [13], or even on a larger scale for *in vivo* experiments [14]. Equally, understanding the EMF interacting with the multi-protein complexes (biological effect of interest), which is linear in dimensions, ranging from one to some tens of nanometers [11,15] is a challenge.

At present, an EM simulation of any realistic problem, even the simplest ones, related to *in vitro* experiments, would involve billions of unknowns and overwhelm the capabilities of current state-of-the-art simulators and computers. This concept is likely to be true also for the next few years. Nevertheless, the only solution to solve this problem of estimating the EMF, where the biological reaction takes place, is to search for the simplest experiments. The latter needs to allow retaining the biological effects of interest on one hand, and importantly to simplify the corresponding EM model in

order to be managed numerically on the other hand.

The simplest experiments where PBM effects take place, are those involved either mitochondria [10,16] or single layered of epithelial cells [17,12]. In the first class of experiments, we needed to deal with small organelles [11,12] of linear dimensions of the order of one micrometer, getting a rather random multilayer disposition. It is well known that it is possible to isolate the mitochonderia and retain their functionality and capabilities to react to photostimulation [18,16,19]. While in the second class of relatively simple experiments, where epithelial cells involved, one can consider simple dispositions (single layer) of large eukaryotic cells [12], which have diameters of a few tens of micrometers. In terms of EM problem complexity, the former class is made up of problems, which are by far simpler, as a result of the significant difference, in terms of dimensions (order of one micrometer versus order of tens of micrometers) and of internal structure. This is why we worked on this type of problems in our experiments.

Another aspect affecting the complexity of our experimental setups was related to the illuminating device, which delivers the photonic energy to biological matter. The majority of the clinical laser devices can generate a Gaussian beam profile, where the intensity of the irradiance is in the center of the target area and become less in transverse direction at the periphery [20]. Therefore, the cells directly in the center of the beam are irradiated at a high fluence, while those on the periphery of the incident beam receive very low dose. As a result, the cells at the beam center may be over stimulated or inhibited while those on the periphery receive insufficient cellar energy to produce any effect. Another crucial factor that plays a role in determining the intensity of the energy density reaching the biological target is the distance of the incident beam profile beam from the target area. In our experimental setting, we

managed to overcome these influencing factors by utilizing a flattop beam profile (FT) hand-piece, which allows to irradiate an area of $1cm^2$ with a uniform irradiance and able to retain the same beam width up to 105cm of distance from the target [9,12]. The latter helps to eliminate the beam divergence issue, whether in contact or at distance, as it generates a uniform homogenous distribution of the energy density (fluence) at an area of $1cm^2$ [9,12]. Under these circumstances, we considered, in our experimental setup, a monochromatic incident wave generated by a laser device, which assimilated to a monochromatic uniform plane wave [21].

Despite of the indicated simplifications considered in our experimental setups, the corresponding EM models still remain a complex matter. Furthermore, the electromagnetic analyses have to face the fact that, in practice, the dispositions of the mitochondria in the experiments are rather random, as well as it is true for their dimensions. Moreover, their internal features may change, in a partially unknown way, from one mitochondrion to another. Therefore, to solve the above problems, different classes of models were employed, and for each class, several parameters were considered, as variable quantities.

The simplest class of models was obtained by replacing the mitochondria by an effective homogeneous plane layer. Each of these models solved in an analytical way. Models of this class differed in relation to various thickness and values of the complex refractive index (n) of the plane layer.

All other classes were referred to three-dimensional models. Several studies focused on the determination of the dielectric features of mitochondria in the NIR band, considering them as made up of a homogeneous effective medium [18,22]. Therefore, we adopted the same approach in our three-dimensional models. Consequently, all

mitochondria involved in our models were simulated by a homogeneous ellipsoid, having the same dimensions and refractive index (*n*) value. However, these dimensions and values can change from one model to another [18]. Therefore, in our case, we did not consider different values of the parameters in the same simulation.

In our three-dimensional models, we considered the usual practical deposition of the mitochondria shown in the results of the fluorescent mitochondria in *ex-vivo* experiments. Based on this, we employed a single layer and triple layers of homogeneous mitochondria in these models. For each of them, sufficient extension of the layers considered or periodic boundary conditions were adopted. With the current technology and best of our knowledge, it is impossible to isolate a single mitochondrion and still retains its functionality. In our three-dimensional model setup, we considered an isolated homogeneous ellipsoid illuminated with NIR field, as our target, in order to have an additional term of comparison of our results and to simplify the analysis of our outcomes' stability.

It shows clearly that studying the EM fields in a biological matter (Cells/tissues) is a complex practice with several challenges. So, according to our approach, in which all the mitochondria were considered homogeneous. Our results presented in terms of, the EMF behavior inside these homogeneous ellipsoids and of quantities like the averages (In space and time) of the power density dissipated by them or of the energy density of the field inside them. Therefore, this approach enabled us to create a validated EM model, for the first time, which examined and provided information on the local EM field, determining PBM effects on isolated homogenous mitochondria instead of the cell of interest.

3.1.3 Aim and objectives of the experimental study

Our study aimed to introduce an electromagnetic (EM) model to have a better understanding of the EM field (EMF), inducing biological reactions.

The objectives were as follows:

1- To examine the behavior of the PBM light attenuation and the properties of EMF in illuminated mitochondria (Main photoacceptors of PBM light in Eukaryotic cells);
2- To analyze the contribution of the mitochondria to the optical properties.
3- To compute the EM data, which might provide a scope, prior to proceeding with the molecular in vitro studies of PBM therapy on bone regeneration.

3. 2 METHODOLOGY

3.2.1 The simple experimental setup

The simple experimental setup of reference for this study showed in figure 1. A flattop hand-piece is hosted in the incubation chamber made up of glass. It generates a beam of uniformed width, which illuminates with a rather uniform intensity the media below it (Figure 1) [16]. In order to operate under the above conditions, the incubation chamber have to be cylindrical, with a circular cross section of an area $\simeq$ $1cm^2$ [16], which corresponds to the diameter of the $w_{ss} \simeq 1.13$ cm. The reasons for considering these dimensions were as follows: firstly to avoid much larger diameters, taking the flattop device generates irradiation over an area of ~$1cm^2$ to illuminate the mitochondria at the floor of the chamber uniformly and secondly to use a smaller cross-section to fully exploit the capabilities of a flattop hand-piece and to avoid a very strong effect of the vertical walls of the incubation chamber.

Figure 1 shows the incubation chamber contents, which are ordered from the top to

the base of the chamber as follows, air, a saline solution, and a set of mitochondria. Below the chamber's glass, there is air.

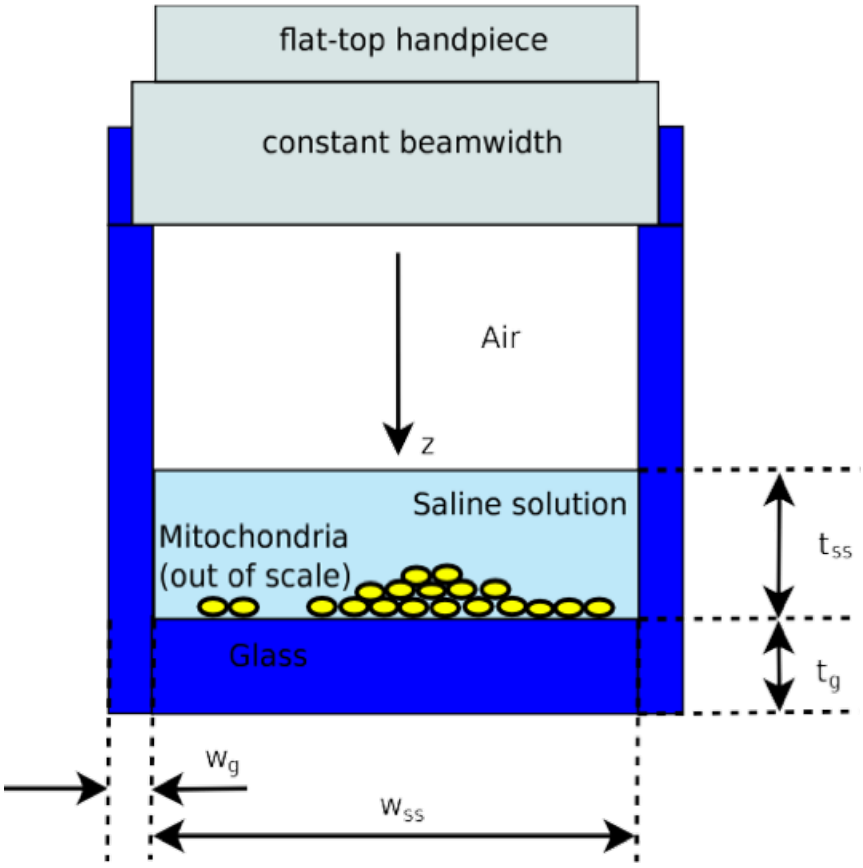

Figure 1: Simple experimental setup with reference to the flattop beam hand-piece used to generate a beam, which illuminates with a uniform intensity, a set of mitochondria on the bottom of a glass-incubated chamber. Abbreviations: W_{ss}: saline solution width, W_g: glass width, t_g: glass thickness, t_{ss}: saline solution thickness.

In our experimental setup, we avoided any significant reflection of the wave transmitted through the last glass-air interface by constituting the buffer solution as follows: 0.1M (Mole per liter) Tris-HCl (pH 7.4), 0.1M KCl, 5mM $MgCl_2$, 0.2mM P1, P5-Di (adenosine-5') pentaphosphate, 0.6mM ouabain, and 5mM KH_2PO_4. As the molarity of this solution is so small at the wavelengths of interest, 808, 980 and

1064 nm, its complex refractive index can be assumed to be the same of that of simple water [23, 24].

3.2.2 Mitochondria isolation *in vivo* experiment

Mitochondria were isolated from bovine liver by a standard differential centrifugation technique [19] and then suspended in the solution. After a few seconds they deposited themselves on the bottom of the incubation chamber but, unfortunately, their final disposition on the floor of the chamber is not at all regular. With 50µg of mitochondria we can get a few small empty regions, all the rest being covered by mitochondria. The mitochondria can get clustered arrangements or form single or multiple layers. It can be expected that the number of superimposed mitochondria is not larger than five. All these data can be extrapolated from figure 2, showing the disposition of mitochondria on a small part of about 22.5 µm × 22.5 µm of a flat floor. The mitochondria were stained by a red-fluorescent dye for illustration purposes [25].

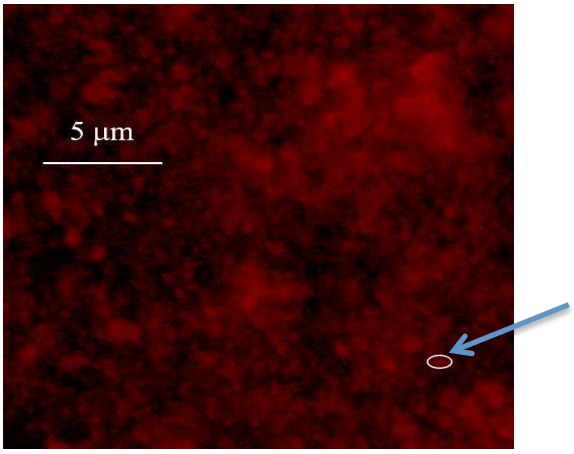

Figure 2: A red-fluorescent dye stains mitochondria, providing deducing information on the typical disposition of the mitochondria on a flat floor. The white ellipse indicates a typical mitochondrion (blue arrow).

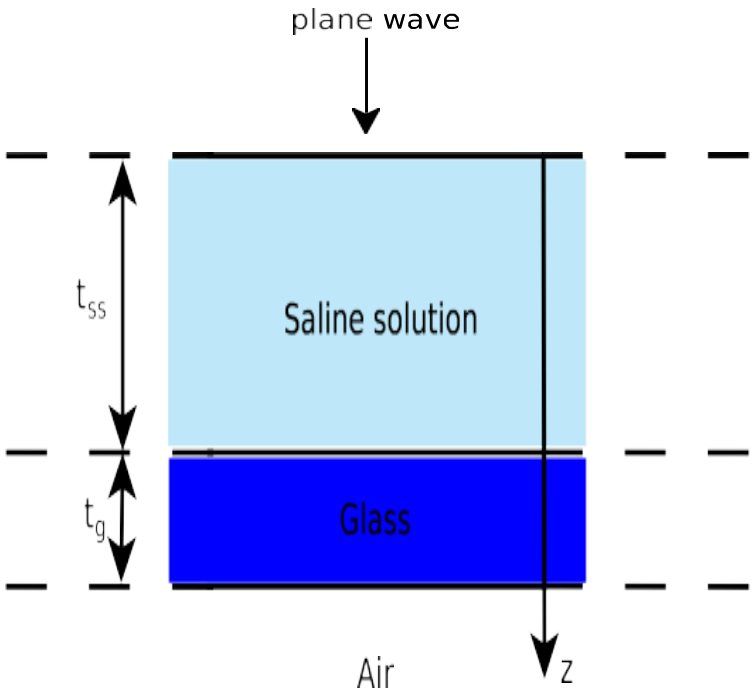

Figure 3: Shows no mitochondria present in the incubation chamber. The electromagnetic field can be calculated by using a simple one-dimensional model.

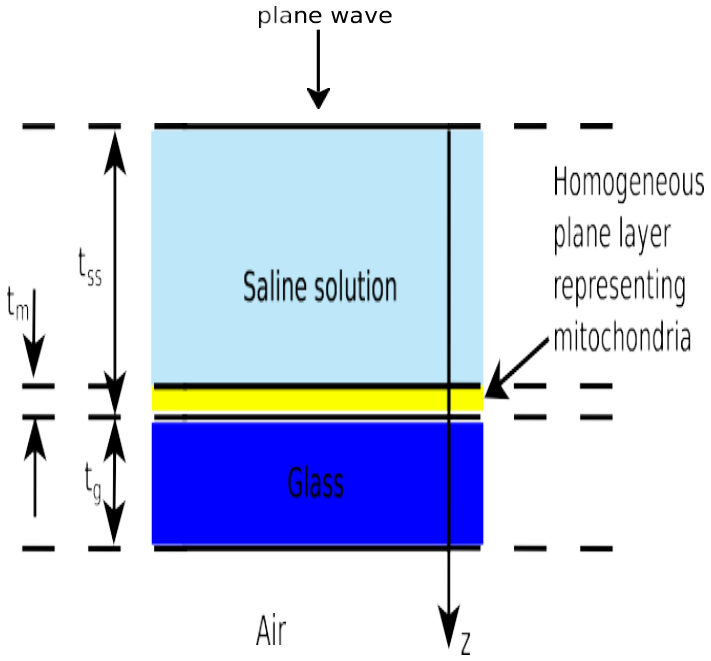

Figure 4: A rough one-dimensional model of our experimental setup where the mitochondria replaced with an effective homogeneous plane layer.

3.2.3 Different classes of electromagnetic models

We mentioned, in our simple experimental setup, that the illuminating field generated by a laser light delivered with flattop hand-piece, guarantees a uniform and homogenous distribution of the energy over an area of $1cm^2$, regardless the distance of the light-target up to 105cm. Therefore, we considered this device with a very good approximation, where the contents of the incubation chamber illuminated with a monochromatic uniform plane wave, propagating along the z direction (Figure 1). Such a monochromatic uniform plane wave, whose time-harmonic dependence e^{jwt} assumed and suppressed throughout, and propagated inside the incubation chamber (If we avoid considering the regions very close to its vertical walls, when there was no mitochondria present) interacted with a multilayered structure of plane layers, which was made up of air, saline solution, glass and air ordered from the top to the base of the chamber respectively. This model illustrated in figure 3 can be easily solved with a semi-analytical simulator.

The same tool can obviously be used to solve a one-dimensional model of the problem of interest, in which the mitochondria are inserted in an effective homogeneous plane layer (Figure 4). Such a model was a rough approximation of the experimental setup that we considered (Figure 1). Moreover, this can be exploited only to give preliminary indications on the magnitudes of the quantities of interest. Interestingly, the approximate results deduced with this model were rather significant, as fully described in results section. The thicknesses of the saline solution, t_{SS}, and glass, t_g, together with their refractive indices, n_{ss}, n_g are of known quantities for all the wavelengths of interest. On the contrary, the thickness t_m and the refractive index n_m, of the plane layer representing the mitochondria have to be considered as variable quantities, in order to analyze different situations of potential interest. For a generic

complex refractive index n, we used the convention $n = n' - jn''$, $n' > 0$, $n'' \geq 0$. Very often, we can define n'' by using the corresponding absorption coefficient μ_a (m^{-1}), since $\mu_a = 4 \pi n''/ \lambda_0$ [26], λ_0 is the vauum wavelength.

The best models, of our experimental setup of interest, were of course the three-dimensional. Unfortunately, the corresponding domains of numerical investigations were in any case huge with respect to λ^3_0. Actually, the usual values of t_g and t_{ss} are of the order of a few millimeters. The flattop hand-piece placed close to the air-saline solution interface. However, taking into account the entire horizontal interfaces, we needed to consider the domain height of several millimeters. Moreover, the cross section of the incubation chamber was of about 1 cm^2. Thus, even neglecting the vertical walls of the chamber, we needed to deal with a domain of investigation of about $1cm^3$. Considering we are interested in λ_0 values of 808, 980 or 1064 nm, obviously the domain of investigation can be, as large as, one thousand billion cubic wavelengths (In vacuum). Since in any discretization procedure, a cubic wavelength requires approximately one thousand degrees of freedom. Therefore, we determined that any realistic three-dimensional simulation should be able to deal with about 10^{15} unknowns, which is by far too large a number for present day computers and simulators to compute. Fortunately, one can avoid such a brute force approach by observing that mitochondria, independently of our knowledge of the detailed mitochondria internal structure, are in any case weak scatterers. This is because the mitochondria have dimensions of the same order of magnitude of the vacuum wavelength of interest for PBM [11]. Moreover, in terms of EM scattering, they behaved as homogeneous [18,22] ellipsoids, having an estimated effective refractive index n_m [27,18,22], which is really close to the refractive indices of the saline

solution and glass. As a matter of fact, for the saline solution [28] and glass [29] we considered

- At λ_0 = 808nm: n'_{ss} = 1.331, $\mu_{a,ss}$ = 1.95m^{-1} (n''_{ss} = 1.25 10^{-7}), n'_g = 1.511, $\mu_{a,g}$ = 0.170m^{-1} (n''_{ss} =1.09 10^{-8}).
- At λ_0 = 980nm: n'_{ss} = 1.328, $\mu_{a,ss}$ = 50.2m^{-1} (n''_{ss} = 3.91 10^{-6}), n'_g = 1.508, $\mu_{a,g}$ = 0.122m^{-1} (n''_{ss} =9.50 10^{-9}).
- At λ_0 = 1064nm: n'_{ss} = 1.328, $\mu_{a,ss}$ = 16.2m^{-1} (n''_{ss} = 1.37 10^{-6}), n'_g = 1.507, $\mu_{a,g}$ = 0.099m^{-1} (n''_{ss} = 8.37 10^{-9}).

However, for the mitochondria, n'm and μa,m are expected to be respectively in the ranges [1.35, 1.45] and [20, 150] m-1 (n"m ∈ [1.28 10-6, 9.61 10-6]) at λ = 800 nm [22, 18, 27] and the same ranges for n'm and μa,m are retained at 980 and 1064 nm. This consideration allowed us to avoid considering many weakly interacting mitochondria in our models. They were all models of EM scattering, in which the incident field was provided by the solution of the one-dimensional model of figure 3. Such a field can be used to determine the boundary conditions for the scattering problems formulated on bounded three-dimensional domains (Parallelepiped was chosen) of appropriate dimensions, including a small number of mitochondria.

The main difficulty in the formulation of these scattering problems is related to the chaotic arrangements of the mitochondria. In order to get a representative set of cases, we were forced to consider a few three-dimensional models. Figure 5 model shows a mitochondrion surrounded by six mitochondria in a horizontal disposition of such organelles, which in particular provided the strongest interaction. By the same token, figure 6 shows where a group of seven mitochondria stacked in vertical position. These first two three-dimensional models can give indications on what happens when the mitochondria assume a single layer configuration. Unfortunately, we knew that the mitochondria can group in clusters and, for this reason, we

considered the model represented in figure 7. In such a model, the mitochondria of the middle layer can have the same orientation, as those of the other layers or rotated by a 90-degree angle (No other angle values considered, in order to avoid considering too many models).

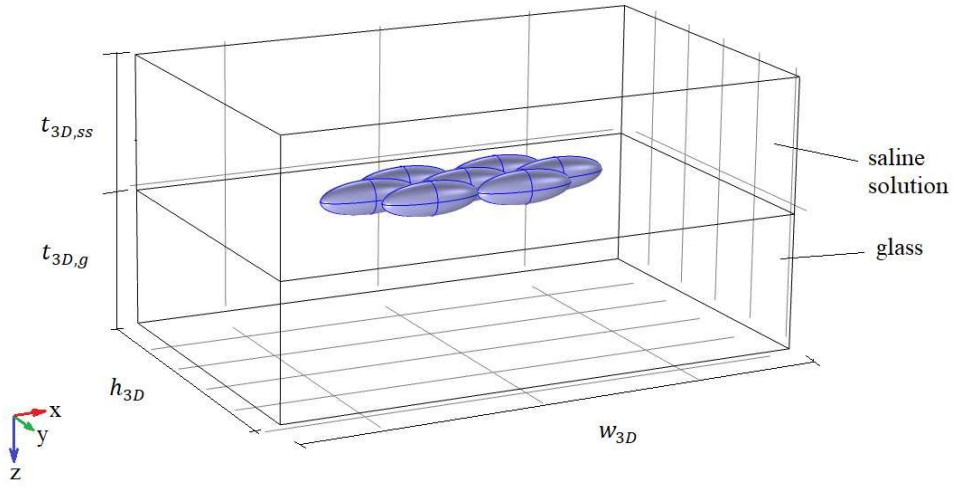

Figure 5: A three-dimensional model with seven mitochondria arranged in a single layer in horizontal position.

Abbreviation: $w_{3D:}$ 3 dimensional width of the glass, $h_{3D:}$ 3-dimensional glass height, $t_{3D,ss}$: 3-dimentional saline solution thickness , $t_{3D,g}$: 3-dimensional glass thickness.

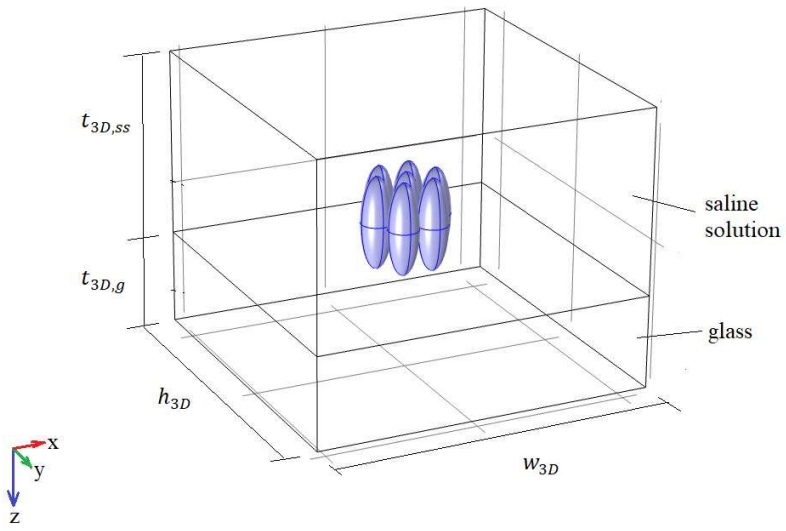

Figure 6: A three-dimensional model with seven mitochondria arranged in a single layer in vertical position.

Abbreviation: w_{3D}: 3-dimensional width of the glass, $h_{3D:}$ 3-dimensional glass height, $t_{3D,ss}$: 3-dimentional saline solution thickness, $t_{3D,g}$: 3-dimensional glass thickness.

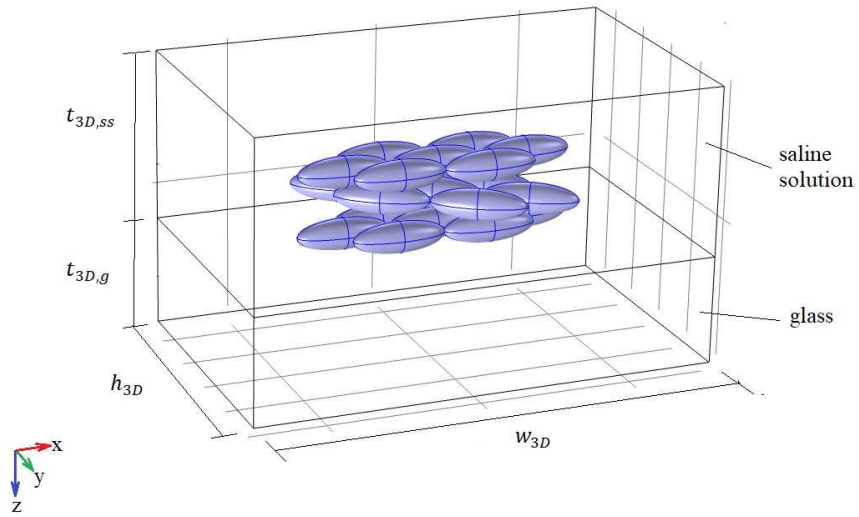

Figure 7: A three-dimensional model with twenty-one mitochondria arranged in three layers in horizontal position.

Abbreviation: w_{3D}: 3-dimensional width of the glass, $h_{3D:}$ 3-dimensional glass height, $t_{3D,ss}$: 3-dimentional saline solution thickness, $t_{3D,g}$: 3-dimensional glass thickness.

In order to understand the effects of more mitochondria present per layer, we considered the similar periodic arrangement of such organelles. Such a model can be easily simulated by considering the periodic boundary conditions on the lateral walls of a small domain, including a single mitochondrion as shown in figure 8. The boundary conditions obtained by the one-dimensional model (Figure 3) are known to be incorrect, unless we place the boundary at sufficient distance from the mitochondria. Taking in account that the scatterers are weak, we should be able to limit such a distance to few wavelengths. In order to determine the appropriate values of w_{3D}, h_{3D}, $t_{3D,ss}$ *and* $t_{3D,g}$ (Figures 5, 6 and 7), we repeated our simulations by considering slightly different values from the above-indicated parameters. However, this type of analysis performed, by considering the simpler model shown in figure 9, in which just one mitochondrion was involved. As pointed out in the introduction section, this is a rather unrealistic model and only to be used to have an additional term of comparison to our results.

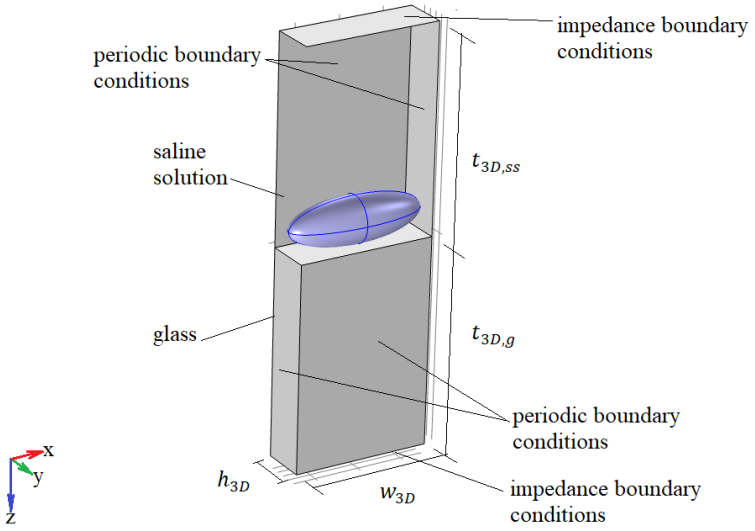

Figure 8: Simple three-dimensional model involved a single mitochondrion, as an element of a periodic arrangement (Single layer configuration of horizontal mitochondria). Abbreviation: w_{3D}: 3-dimensional width of the glass, h_{3D}: 3-dimensional glass height, $t_{3D,ss}$: 3-dimentional saline solution thickness, $t_{3D,g}$: 3-dimensional glass thickness.

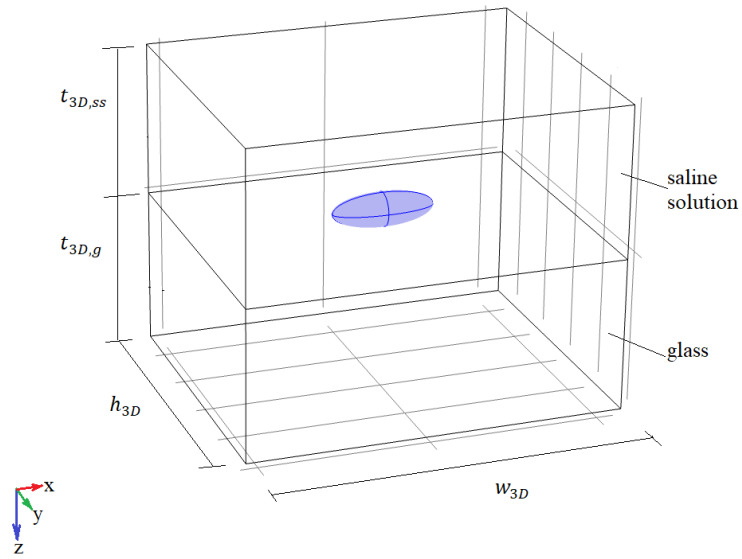

Figure 9: A simple three-dimensional model involved a single mitochondrion in horizontal position. Abbreviation: w_{3D}: 3-dimensional width of the glass, h_{3D}: 3-dimensional glass height, $t_{3D,ss}$: 3-dimentional saline solution thickness, $t_{3D,g}$: 3-dimensional glass thickness.

3.3 RESULTS AND DISCUSSION

In the following sub-headings, different considerations related to the numerical results presented.

3.3.1 Stability of the three-dimensional results

As already mentioned, we used the model of figure 9, to determine the appropriate distance of the boundary from the mitochondrion. Such a value should be found by balancing the need to consider small volumes of the domains of numerical investigations, resulting in simulations with fewer unknowns, and a large separation between the boundary and the scatterer, which was needed to reduce the error of the boundary conditions. For this analysis, it was not necessary to consider many different values of the wavelength of the geometrical quantities and of the constitutive parameters. We simply chose the intermediate wavelength (980 nm) and the values of the parameters of the mitochondrion, giving the largest scattering effect, in order to consider the worst-case scenario [Diameter (dm), and length (Im) of the mitochondrion respectively equal to 1 and 3 micrometers, n'_m =1.45, $\mu_{a,m}$ =150m^{-1}]. Since it is known that the minimal distance should be at least a few wavelengths, we considered such a distance equal to 1, 1.5, 2, . ., .,5 micrometers (correspondingly, the domain dimension w_{3D} will be equal to 5, 6, 7, . . . , 13 micrometers while h_{3D} and $t_{3D,ss}$ + $t_{3D,g}$, with $t_{3D,ss}$ − 1 = $t_{3D,g}$, will be 3, 4, 5, . . . , 11 micrometers). Next, we considered a grid of N = 49011 points uniformly distributed (A point every 0.1 micrometers) in the smallest of the numerical domains considered and, if we denoted by El (r_i), l = 1, 2, 3,..., 9, the electric field computed at point r_i by the numerical simulator when, respectively, w_{3D} = 5,6,7,...,13, we computed the so-called root mean square of the difference field $E_{m+1} - E_m$:

$$rms(\Delta E_m) = \sqrt{\frac{1}{N}\sum_{i=1}^{N} |\mathbf{E}_{m+1}(\mathbf{r}_i) - \mathbf{E}_m(\mathbf{r}_i)|^2}, \quad m = 1, 2, 3, \ldots, 8. \qquad (1)$$

In all simulations we have always considered an impinging monochromatic plane wave at power density of 1 [W cm^{-2}] (corresponding to |**E**| = 2744.9 [V m^{-1}]). For these simulations, we considered, in particular, a linear polarization of the incident field along the y-axis.

In figure 10, we showed the results of *rms* (ΔE_m) versus *m*, considering that the magnitude of the electric field was of the same order of the magnitude of the electric field of the incident wave. We observed that the root mean square of the difference assumed a stable negligible value for $m \geq 2$. For this reason, we can confirm that our results did not change in a significant way, if the minimal distance of the boundary from the scatterer was larger than or equal to 1.5 micrometers. In order to have some margin of safety, we considered such a distance to be at least 2.5 micrometers. However, we have verified this, for the model of figure 5, in the presence of mitochondria having the same features as above, the solutions obtained, considering the minimum distance of mitochondria from the boundary equal to 2 or 3 micrometers, which were almost exactly the same. By extrapolating the previous result, we used a distance of at least 2.5 λ_0 for other wavelength values.

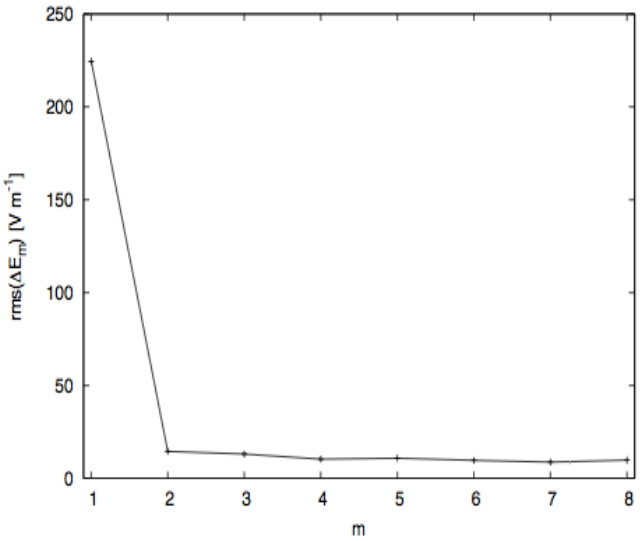

Figure 10: Behavior of the root mean square of the difference field $\mathbf{E}_{m+1}$ - $\mathbf{E}_{m}$ versus m

3.3.2 Effects of the incident field polarization

The previous analysis provided the necessary information to define the appropriate values of w_{3D}, h_{3D}, $t_{3D,ss}$ and $t_{3D,g}$,in order to obtain reliable results from our three-dimensional models. We utilized such models to analyze the effect of the polarization of the incident field on the results of interest. In figure 11, we showed the magnitude of the electric field along the z-axis in the presence of one mitochondrion or a layer of mitochondria (Figures 9 and 5). Also in this case, the wavelength and the amplitude of the incident field were the same as before. The dimensions of the mitochondria were the same as well. However, for these simulations, we considered n'_m (Refractive index mitochondrion) = 1.4 and $\mu_{a,m}$ (Absorption coefficient of mitochondrion) = 85 m^{-1}. The interface between the saline solution and the glass was set at z = 5 millimeters and the mitochondria in these models were in the range [4.999,5] millimeters. The *z*-axis considered passing through the center of gravity of the central mitochondrion of the models.

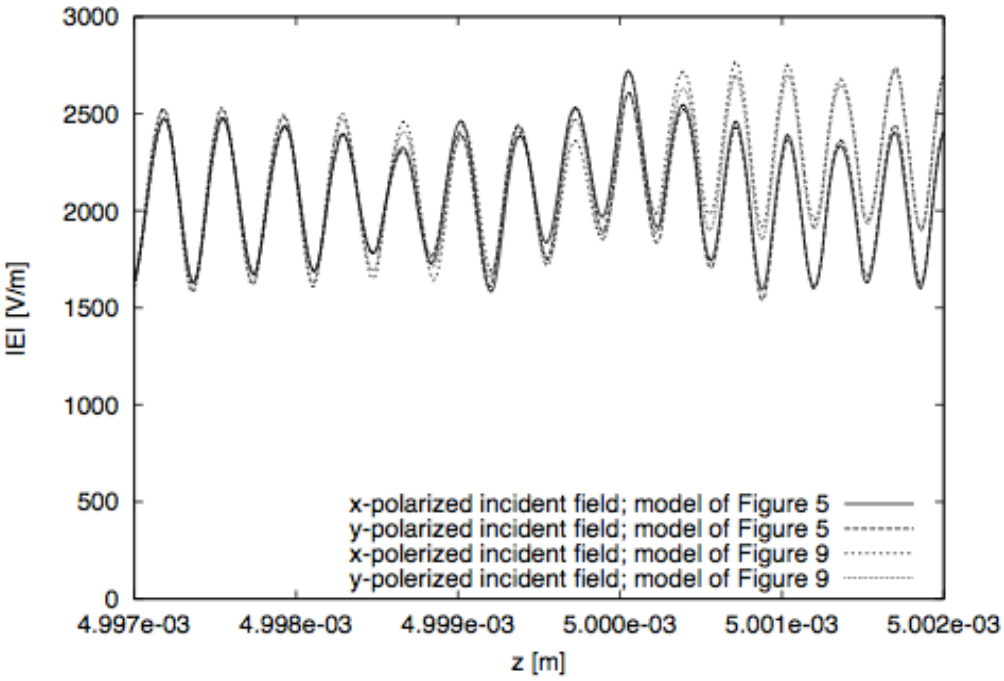

Figure 11: Behavior of |**E**| along the *z*-axis. The results are computed by using the models of figures 9 and 5.

The solutions can present some differences, which were not large in respect to the average values of the magnitudes of the fields. However, if we focused, in particular, on |**E**| in the central mitochondrion, we observed that the effects due to different polarizations of the incident field were negligible.

The very small differences in terms of fields in the mitochondria resulted in negligible differences in terms of the average (In space and time) energy density (E_d) of the electromagnetic field,

$$E_d = \frac{\int_V \frac{1}{4}\left(\varepsilon_0 \varepsilon'_{r,m} |\mathbf{E}(\mathbf{r})|^2 + \mu_0 |\mathbf{H}(\mathbf{r})|^2\right)}{\text{volume of the central mitochondrion}}, \qquad (2)$$

and of average (in space and time) dissipated power density (P_d) in the central mitochondria (Occupying the region V in the formulas)

$$P_d = \frac{\int_V \frac{1}{2}\omega\varepsilon_0\varepsilon''_{r,m}|\mathbf{E}(\mathbf{r})|^2}{\text{volume of the central mitochondrion}}, \quad (3)$$

where $\varepsilon'_{r,m}$ and $\varepsilon''_{r,m}$ are respectively the real part and the magnitude of the imaginary part of the relative permittivity of the mitochondrion, $\varepsilon_{r,m}$, being $\varepsilon_{r,m} = \varepsilon'_{rm} - j\,\varepsilon''_{r,m} = n^2_{m.}$ In order to generalize this conclusion, we computed E_d and P_d by using different polarizations and models and the results are shown in tables 1 and 2. For all the models, the results obtained, by using x or y polarization of the incident field, were almost the same with a maximum difference of less than 2.7%. The subsection 3.3.4, we showed that the dimensions and the constitutive parameters of the mitochondria had no affect on this result in a significant way. Therefore, in general, we concluded that polarization has negligible effects in our PBM studies. In this context, all the following results were calculated by using the y polarization of the incident field.

	Model Figure 9	**Model Figure 5**	**Model Figure 7**	**Model Figure 6**	**Model Figure 8**
x-polarized	$3.824\ 10^{-5}$	$3.731\ 10^{-5}$	$3.798\ 10^{-5}$	$3.427\ 10^{-5}$	$3.759\ 10^{-5}$
***y*-polarized**	3.776 10-^{5}	$3.687\ 10^{-5}$	$3.758\ 10^{-5}$	$3.431\ 10^{-5}$	$3.716\ 10^{-5}$
Difference %	1.254	1.211	1.053	$-1.063\ 10^{-1}$	1.166

Table 1: Values of E_d [Jm^{-1}] computed by using different linear polarizations of the incident field and different models.

3.3.3 Comparison of one-dimensional (1D) versus three-dimensional (3D) results

The previous considerations did not exclude the possibility of obtaining good approximations from one-dimensional models. For this reason, at this stage, we compared the outcomes of the one-dimensional model of figure 4 with those of the more detailed three-dimensional models. In this approach, we can draw some conclusions related to the quality of the results provided by the simplest model.

	Model Figure 9	**Model Figure 5**	**Model Figure 7**	**Model Figure 6**	**Model Figure 8**
x-polarized	$6.957\ 10^{-5}$	$6.788\ 10^{-5}$	$6.941\ 10^{-5}$	$6.236\ 10^{-5}$	$6.837\ 10^{-5}$
***y*-polarized**	6.785 10-^{5}	$6.626\ 10^{-5}$	$6.760\ 10^{-5}$	$6.242\ 10^{-5}$	$6.673\ 10^{-5}$
Difference %	2.543	2.445	2.679	$-1.079\ 10^{-1}$	2.451

Table 2: Values of P_d [W m^{-3}] computed by using different linear polarizations of the incident field and different models.

To illustrate the principle, we fixed the value of the parameters by considering again mitochondria with d_m = 1 micrometer, n'_m = 1.4 and $\mu_{a,m}$ = 85m^{-1}. Correspondingly, we fixed t_m=1 micrometer for the one-dimensional model. In figure 12, the magnitudes of the total electric fields were plotted along a line parallel to the *x*-axis, and passed through the center of the mitochondrion. The one-dimensional approximation was very close to the results obtained from the models of figures 5, 8 and 9. In particular, the maximum difference between the fields of the three-dimensional models with respect to the one-dimensional was less than 6.3% of the incident field magnitude.

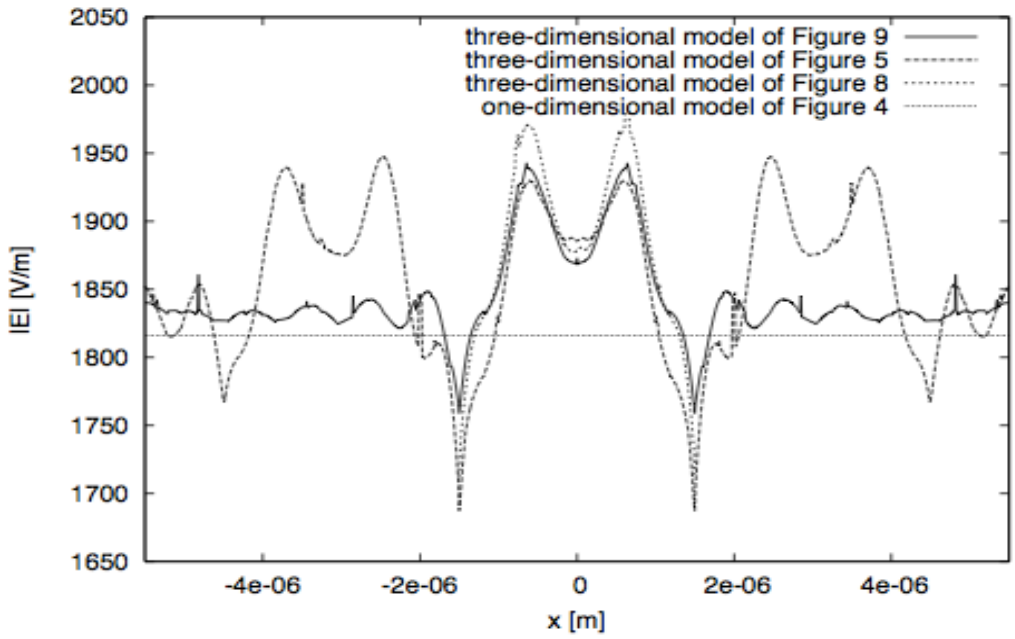

Figure 12: Behavior of |**E**| (Electromagnetic field) along a line parallel to the x-axis, and passing through the center of the gravity of the mitochondria. The results are computed by using different one-dimensional and three-dimensional models.

Similarly, in figure 13, the fields for different models were compared to the line parallel to the *y*-axis, which passed through the center of the mitochondrion. The result of the one-dimensional model was close to all three three-dimensional solutions, giving a maximum difference of less than 5.2% of the incident field. We did not plot the fields along the *z* -axis because the results were very similar to those shown in figure 11. Again, in this case, the fields were similar, despite there was a maximum difference of approximately 12.6% in the glass. However, in water and inside the mitochondria, the difference was not more than 3.7% of the incident field. As before, these considerations can be extended to the energy and dissipated power densities. The E_d *value* given by the one-dimensional models differed from that obtained by the three-dimensional models of figures 9 and 5 at approximately 4.94% and 2.63% respectively. Likewise, the P_d value differed by approximately 4.08% and

1.78% in the two cases respectively.

It was possible to draw a similar comparison between the one-dimensional model with t_m=3 micrometers and the three-dimensional models of figures 7 and 6. For example, for the same n'_m and $\mu_{a,m}$ considered above, the difference between the Ed values obtained from the one-dimensional model and the three-dimensional of figure 7 was just about 1.61% and the corresponding P_d difference was 1.72%. The same differences, but evaluated in the regions occupied by the center of the mitochondrion from the top and bottom layers, were 1.05% and 2.68% respectively for the average energy density and 0.49% and 1.73% respectively for the average dissipated power density. The values of energy and power densities of the one-dimensional model in comparison to those of the three-dimensional model of figure 6 differed at approximately 7.77% and 7.78% respectively.

In summary, the accuracy of the one-dimensional model results was confirmed for all three-dimensional models. Moreover, the results in 3.3.4 subheading showed the same results, which held true for all values of the parameters. Hence, we can state that the solution given by the one-dimensional model was quite meaningful for the kind of problems at hand. This idea was strengthened by the fact that, in practical experiments, the stability of the power emitted by the laser source can vary by ±20% [30].

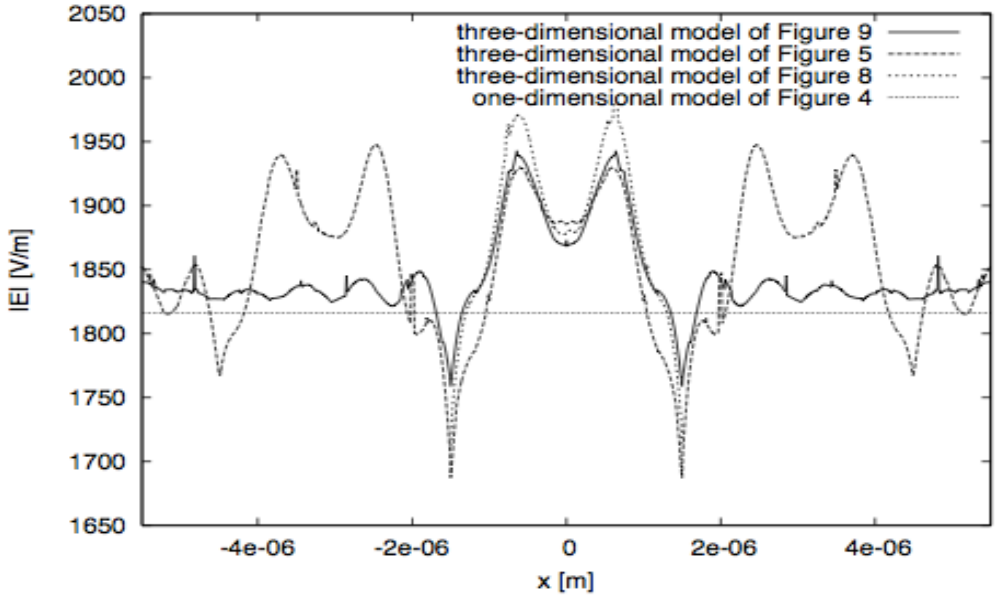

Figure 13: Behavior of |**E**| along a line parallel to the y-axis, and passing through the center of the gravity of the mitochondria. The results are computed by using different one-dimensional and three-dimensional models.

3.3.4 Effects of geometrical and constitutive parameters

A couple of the above deductions referred to the effects of the parameters d_m, n'_m and $\mu_{a,m}$ on our results. Figure 14 showed that the E_d values were calculated by using the three-dimensional models of figures 9, 5 and 7. They were calculated by considering n''_m and $\mu_{a,m}$, as fixed quantities (n'_m= 1.4, $\mu_{a,m}$ = 85 m^{-1}) while d_m was free to change in the set $\{0.510^{-6}, 0.7510^{-6}, 1.010^{-6}\}$ m [7]. Figure 15 reported that the analogous behavior of P_d. One can observe that d_m did not affect the values of E_d and P_d in a significant way. The largest value of these effects was smaller than 5%. Even though we did not show the results, we have verified that in the conclusion, which held true for all of the considered n'_m and $\mu_{a,m}$ values. As this stage, we analyzed the effects of n'_m and $\mu_{a,m}$ on E_d and P_d by fixing d_m = 1 micrometer. The results are summarized in tables 3 and 4.

As expected from our former considerations, the differences of the values computed by using different models were negligible. Moreover, as a consequence of equations (2) and (3) and the relation between n_m and $\varepsilon_{r,m}$, the E_d results to be totally independent of $\mu_{a,m}$ and increased with n'_m, while P_d was largely independent of n'_m and it was directly proportional to $\mu_{a,m}$. This occurred because the indicated changes of the constitutive parameters were not able to modify the average value of |**E**| in the central mitochondrion in a significant way.

	Model Figure 9	**Model Figure 5**	**Model Figure 7**
$n'_m = 1.35, \mu_{a,m} = 20\text{m}^{-1}$	$3.555\ 10^{-5}$	$3.523\ 10^{-5}$	$3.541\ 10^{-5}$
$n'_m = 1.35, \mu_{a,m} = 85\text{m}^{-1}$	$3.555\ 10^{-5}$	$3.523\ 10^{-5}$	$3.541\ 10^{-5}$
$n'_m = 1.35, \mu_{a,m} = 150\text{m}^{-1}$	$3.555\ 10^{-5}$	$3.523\ 10^{-5}$	$3.540\ 10^{-5}$
$n'_m = 1.40, \mu_{a,m} = 20\text{m}^{-1}$	$3.776\ 10^{-5}$	$3.687\ 10^{-5}$	$3.758\ 10^{-5}$
$n'_m = 1.40, \mu_{a,m} = 85\text{m}^{-1}$	$3.776\ 10^{-5}$	$3.687\ 10^{-5}$	$3.758\ 10^{-5}$
$n'_m = 1.40, \mu_{a,m} = 150\text{m}^{-1}$	$3.776\ 10^{-5}$	$3.687\ 10^{-5}$	$3.758\ 10^{-5}$
$n'_m = 1.45, \mu_{a,m} = 20\text{m}^{-1}$	$3.776\ 10^{-5}$	$3.687\ 10^{-5}$	$3.758\ 10^{-5}$
$n'_m = 1.45, \mu_{a,m} = 85\text{m}^{-1}$	$4.013\ 10^{-5}$	$3.866\ 10^{-5}$	$4.052\ 10^{-5}$
$n'_m = 1.45, \mu_{a,m} = 150\text{m}^{-1}$	$4.013\ 10^{-5}$	$3.866\ 10^{-5}$	$4.052\ 10^{-5}$

Table 3: Values of E_d (J m^{-3}) computed by using different values of n'_m and $\mu_{a,m}$ and different three-dimensional models. Abbreviations: E_d: Energy density, $\mu_{a,m}$: Mitochondria absorption coefficient, n'_m: Mitochondria refractive index

	Model Figure 9	Model Figure 5	Model Figure 7
$n'_m = 1.35,\ \mu_{a,m} = 20\text{m}^{-1}$	$1.564\ 10^5$	$1.551\ 10^5$	$1.558\ 10^5$
$n'_m = 1.35,\ \mu_{a,m} = 85\text{m}^{-1}$	$6.648\ 10^5$	$6.591\ 10^5$	$6.619\ 10^5$
$n'_m = 1.45,\ \mu_{a,m} = 150\text{m}^{-1}$	$1.173\ 10^6$	$1.163\ 10^6$	$1.168\ 10^6$
$n'_m = 1.40,\ \mu_{a,m} = 20\text{m}^{-1}$	$1.596\ 10^5$	$1.559\ 10^5$	$1.591\ 10^5$
$n'_m = 1.40,\ \mu_{a,m} = 85\text{m}^{-1}$	$6.785\ 10^5$	$6.626\ 10^5$	$6.760\ 10^5$
$n'_m = 1.40,\ \mu_{a,m} = 150\text{m}^{-1}$	$1.197\ 10^6$	$1.169\ 10^6$	$1.193\ 10^6$
$n'_m = 1.45,\ \mu_{a,m} = 20\text{m}^{-1}$	$1.633\ 10^5$	$1.574\ 10^5$	$1.659\ 10^5$
$n'_m = 1.45,\ \mu_{a,m} = 85\text{m}^{-1}$	$6.941\ 10^5$	$6.687\ 10^5$	$7.049\ 10^5$
$n'_m = 1.45,\ \mu_{a,m} = 150\text{m}^{-1}$	$1.225\ 10^6$	$1.180\ 10^6$	$1.244\ 10^6$

Table 4: Values of P_d (Wm^{-3}) computed by using different values of n'_m and $\mu_{a,m}$ and different three-dimensional models. Abbreviations: P_d: Power density, $\mu_{a,m}$: Mitochondria absorption coefficient, n'_m: Mitochondria refractive index

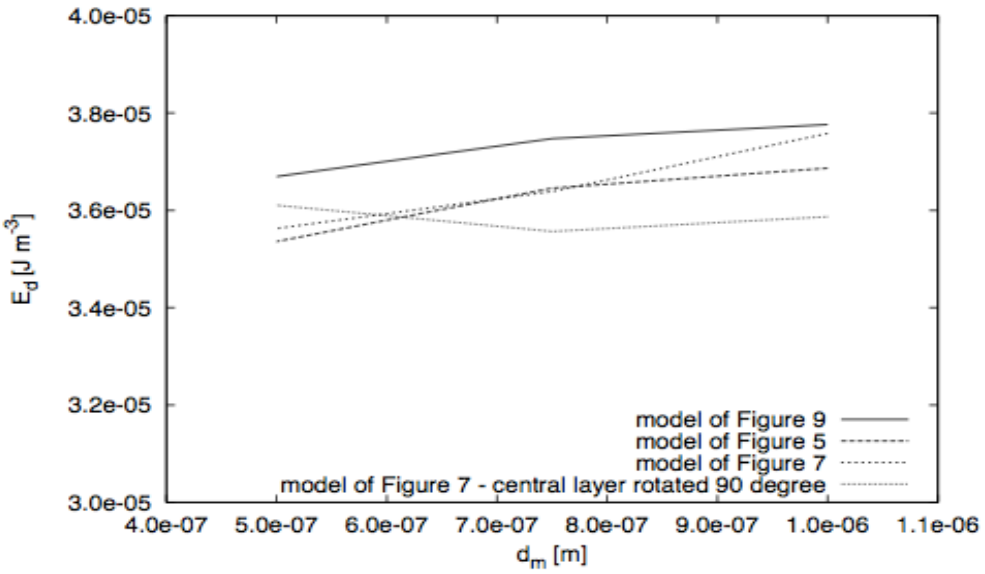

Figure 14: Behavior of E_d for $d_m \in \{0.5\ 10^{-6}, 0.75\ 10^{-6}, 1.0\ 10^{-6}\}$ m^{-1}

The constitutive parameters of the mitochondria are fixed (n'_m = 1.4, $\mu_{a,m}$ = 85m^{-1}) but different three-dimensional models were considered to compute E_d.

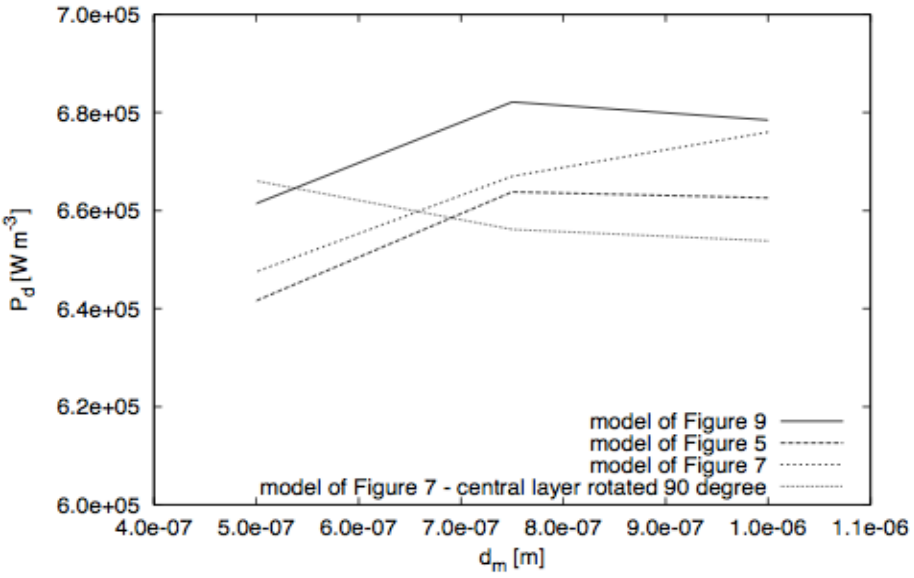

Figure 15: Behavior of P_d for $d_m \in \{0.5\ 10^{-6}, 0.75\ 10^{-6}, 1.0\ 10^{-6}\}\text{m}^{-1}$. The constitutive parameters of the mitochondria are fixed ($n'_m = 1.4$, $\mu_{a,m} = 85\text{m}^{-1}$) but different three- dimensional models were considered to compute P_d.

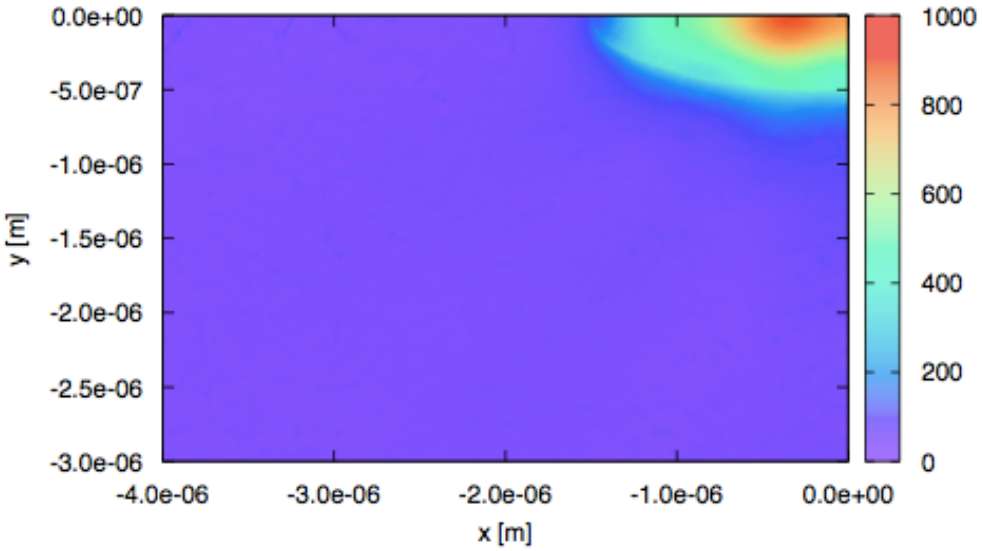

Figure 16: A color image of $|\mathbf{E}_s|$ on the plane z = 4999.5 10-^{6} m passing through the center of gravity of the mitochondrion. The field is computed for the model of figure 9 by using dm = 10-^{6} m, n'_m = 1.45 and $\mu_{a,m}$ = 150 m^{-1}

3.3.5 Analysis of the scattered field

In defining most of our three-dimensional models, we assumed that the mitochondria were weak scatterers and that it was not necessary to consider the organelles, which were far away, in the planes orthogonal to the direction of propagation of the incident field, from the ones under investigation. In this subheading, we provided some justifications for this assumption. We considered E_i to be the electric field of the incident wave, which was obtained when no mitochondrion was present (Figure 3 model). We defined, as usual, the scattered field, E_S, as the difference between the electric field in the presence of mitochondria and E_i. Figures 16 and 17 showed that the colored images of $|E_S|$ on the plane z = 4999.5 10^{-6} m, passing through the center of gravity of the central mitochondria (Just a quarter of the plane showed for all the figures of this type). The fields computed, respectively, by using the models of figure 9 and 5 and all the organelles characterized by d_m = 10^{-6}m, n'_m = 1.45 and $\mu_{a,m}$ = 150 m^{-1}, in order to get the largest scattering effect.

If we focus on the scatted field, which was presented in the central of the mitochondria, we can observe, by comparison, that the neighboring mitochondria were not strongly influencing it. Hence, we can conclude here that the lateral interaction was weak and our models, which considered a small number of mitochondria in the same place, were correct. Moreover, in the indicated plane, the $|\mathbf{E}_s|$ was not negligible just inside the mitochondria. From this consideration, we can understand why it was not necessary to place the lateral boundaries far away from the organelles.

In figure 18, we showed that the $|\mathbf{E}_s|$ on the (x,z) plane for the model of figure 7, and as before, the same values of d_m, n'_m and $\mu_{a,m}$ were used. Since $\mathbf{E}_s$ did not present a

significant standing wave pattern in the *z* direction, we can understand that the top and bottom walls of the boundary were able to absorb such a field. Moreover, figure 18 showed that the presence of three layers affected the field. This was confirmed by the behavior of |**E**| along the *z*-axis, which was reported in figure 19. However, in our study, it is important to observe that |**E**| in the central mitochondrion of the top layer of figure 7 model was similar to the same quantity, in the corresponding mitochondria of the other models considered in the figure. However, the results were not so similar, when the central and bottom layers of the figure 7 model were considered. Thus, in any case, the difference was not of too large value. In terms of the average energy and the dissipated power densities in the central mitochondrion of the different layers, the results were almost identical. In particular, the average energy density (J m^{-3}) in the central mitochondrion was equal to the following values: 3.7810^{-5} for the figure 9 model, 3.6910^{-5} for figure 5 model, and 3.6610^{-5}, 3.7610^{-5} and 3.8010^{-5} for the top, central and bottom layer of figure 7 model respectively. In terms of the average dissipated power density (W m^{-3}), the corresponding numbers were as follows: 6.78 10^5, 6.63 10^5, 6.68 10^5, 6.76 10^5 and 6.82 10^5, respectively.

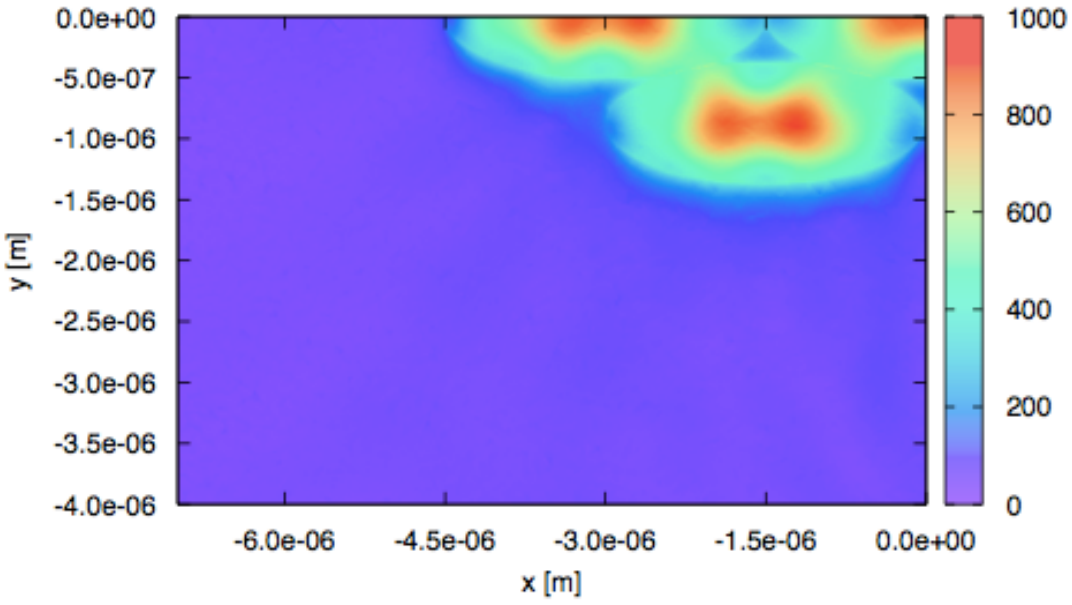

Figure 17: A color image of $|\mathbf{E_S}|$ on the plane z = 4999.5 10^{-6} m passing through the center of gravity of the mitochondria. The field is computed for the model of figure 5 by using $d_m = 10^{-6}$ m, $n'_m = 1.45$ and $\mu_{a,m} = 150\ m^{-1}$.

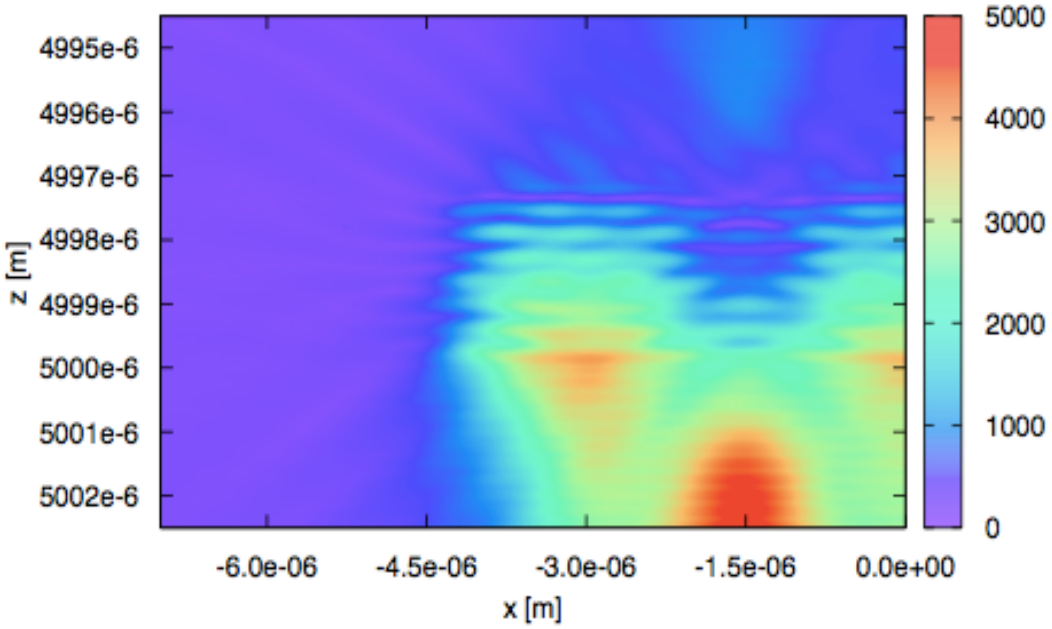

Figure 18: A color image of $|\mathbf{E_S}|$ on the (x,z) plane (passing through the center of gravity of the central mitochondrion of each layer). The field is computed for the model of figure 7 by using $d_m = 10^{-6}$ m, $n'_m = 1.45$ and $\mu_{a,m} = 150 m^{-1}$.

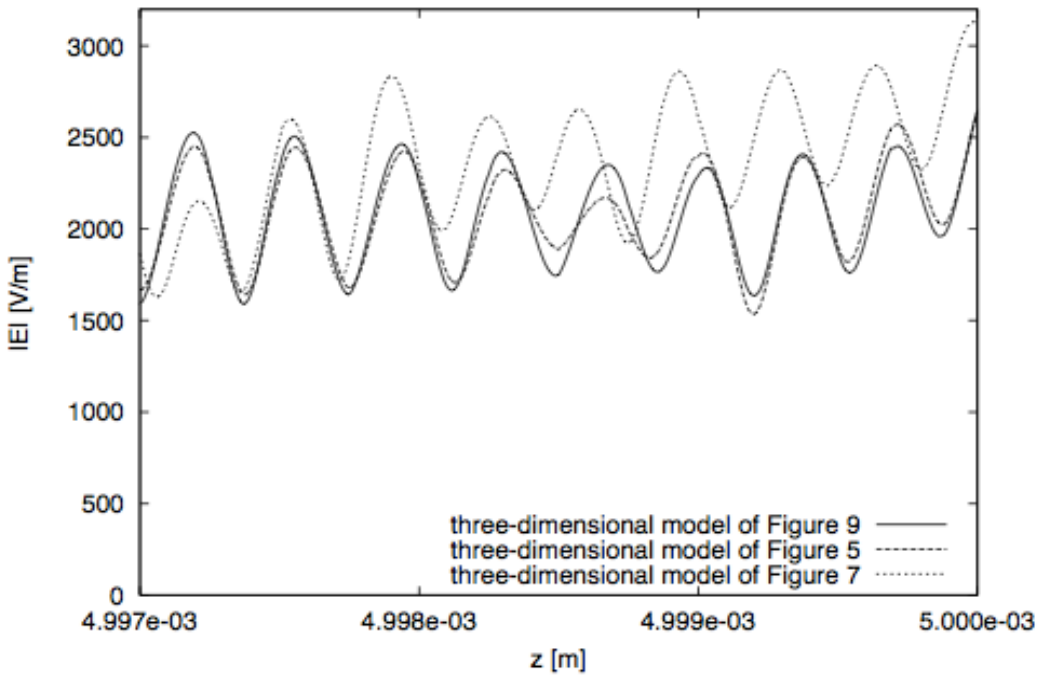

Figure 19: Behavior of |**E**| along the z-axis. The results computed by using the models of figures 9, 5 and 7.

3.3.6 Different λ_0 values

All the above results were computed by using λ_0 = 980 nm. However, all the conclusions of the previous subsections held true for λ_0 equal to 808 and 1064 nm. To support this conclusion, we reported in table 5 and 6 that the P_d values for λ_0 = 808nm and λ_0 = 1064nm respectively. The results were computed by using different models and different geometrical or constitutive parameters. These data confirmed the accuracy of the results of the one-dimensional model (the difference in the P_d values were in any case smaller than 20%), according to the conclusions of Subsection 3.3.3, and that P_d was largely independent from n'_m and it was directly proportional to $\mu_{a,m}$, as reported in subheading 3.3.4.

	Model figure 4 $t_m = 10^{-6}$ m	**Model figure 4 $t_m = 310^{-6}$ m**	**Model figure 9**	**Model figure 5**	**Model figure 7**
$n'_m = 1.35$ $\mu_{a,m} = 20\text{m}^{-1}$	$2.117\ 10^5$	$2.013\ 10^5$	$2.170\ 10^5$	$2.155\ 10^5$	$2.155\ 10^5$
$n'_m = 1.35$ $\mu_{a,m} = 85\text{m}^{-1}$	$8.997\ 10^5$	$8.555\ 10^5$	$9.221\ 10^5$	$9.158\ 10^5$	$9.176\ 10^5$
$n'_m = 1.45$ $\mu_{a,m} = 150\text{m}^{-1}$	$1.588\ 10^6$	$1.509\ 10^6$	$1.627\ 10^6$	$1.616\ 10^6$	$1.619\ 10^6$
$n'_m = 1.40$ $\mu_{a,m} = 20\text{m}^{-1}$	$2.027\ 10^5$	$1.936\ 10^5$	$2.203\ 10^5$	$2.159\ 10^5$	$2.249\ 10^5$
$n'_m = 1.40$ $\mu_{a,m} = 85\text{m}^{-1}$	$8.615\ 10^5$	$8.225\ 10^5$	$9.363\ 10^5$	$9.174\ 10^5$	$9.559\ 10^5$
$n'_m = 1.40$ $\mu_{a,m} = 150\text{m}^{-1}$	$1.520\ 10^6$	$1.451\ 10^6$	$1.652\ 10^6$	$1.619\ 10^6$	$1.687\ 10^6$
$n'_m = 1.45$ $\mu_{a,m} = 20\text{m}^{-1}$	$1.979\ 10^5$	$2.164\ 10^5$	$2.224\ 10^5$	$2.172\ 10^5$	$1.960\ 10^5$
$n'_m = 1.45$ $\mu_{a,m} = 85\text{m}^{-1}$	$8.411\ 10^5$	$9.196\ 10^5$	$9.538\ 10^5$	$9.229\ 10^5$	1.00310^6
$n'_m = 1.45$ $\mu_{a,m} = 150\text{m}^{-1}$	$1.225\ 10^6$	$1.180\ 10^6$	$1.244\ 10^6$	$1.629\ 10^6$	$1.771\ 10^6$

Table 5: Values of P_d (W m^{-3}) computed by using $\lambda_0 = 808$ nm, different models and different geometrical or constitutive parameters.

	Model Figure 4 $t_m = 10^{-6}$ m	**Model Figure 4 $t_m = 310^{-6}$ m**	**Model figure 9**	**Model figure 5**	**Model figure 7**
$n'_m = 1.35$ $\mu_{a,m} = 20\text{m}^{-1}$	$1.831\ 10^5$	$1.805\ 10^5$	$1.867\ 10^5$	$1.854\ 10^5$	$1.870\ 10^5$
$n'_m = 1.35$ $\mu_{a,m} = 85\text{m}^{-1}$	$7.783\ 10^5$	$7.670\ 10^5$	$7.933\ 10^5$	$7.878\ 10^5$	$7.946\ 10^5$
$n'_m = 1.45$ $\mu_{a,m} = 150\text{m}^{-1}$	$1.373\ 10^6$	$1.353\ 10^6$	$1.400\ 10^6$	$1.390\ 10^6$	$1.402\ 10^6$
$n'_m = 1.40$ $\mu_{a,m} = 20\text{m}^{-1}$	$1.792\ 10^5$	$1.835\ 10^5$	$1.912\ 10^5$	$1.875\ 10^5$	$1.933\ 10^5$
$n'_m = 1.40$ $\mu_{a,m} = 85\text{m}^{-1}$	$7.615\ 10^5$	$7.798\ 10^5$	$8.125\ 10^5$	$7.967\ 10^5$	$8.217\ 10^5$
$n'_m = 1.40$ $\mu_{a,m} = 150\text{m}^{-1}$	$1.344\ 10^6$	$1.376\ 10^6$	$1.434\ 10^6$	$1.406\ 10^6$	$1.450\ 10^6$
$n'_m = 1.45$ $\mu_{a,m} = 20\text{m}^{-1}$	$1.773\ 10^5$	$1.976\ 10^5$	$1.963\ 10^5$	$1.903\ 10^5$	$2.021\ 10^5$
$n'_m = 1.45$ $\mu_{a,m} = 85\text{m}^{-1}$	$7.536\ 10^5$	$8.396\ 10^5$	$8.342\ 10^5$	$8.089\ 10^5$	$8.588\ 10^6$
$n'_m = 1.45$ $\mu_{a,m} = 150\text{m}^{-1}$	$1.330\ 10^6$	$1.481\ 10^6$	$1.472\ 10^6$	$1.427\ 10^6$	$1.515\ 10^6$

Table 6: Values of P_d (Wm^{-3}) computed by using $\lambda_0 = 1064$ nm, different models and different geometrical or constitutive parameters.

3.4 CONCLUSION

Our experiments, for the first, introduced a set of simple models to study the photobiomodualtion of mitochondria. Utilization of these models showed, for the phenomenon of interest, that the incident field polarization has small effects on the EM field and negligible consequences on the average energy and dissipated power

densities. The same was shown to hold true for the different dispositions that the mitochondria can assume.

The analogous conclusions were obtained by taking into account the possible changes in the dimensions or of the real part of the refractive index of the considered organelles. The variations of the absorption coefficient were shown to have significant effects on the average dissipated power density in the mitochondria but these effects can be predicted in a surprisingly simple way. Moreover, it was shown that the numerical analysis, of the problems of interest, could be computed by using three-dimensional models, involving only a few mitochondria in the plane, which was transverse to the direction of propagation of the illuminating light. Finally, the results surprisingly showed that trivial one-dimensional models provide significant information on the electromagnetic field, which stimulated the mitochondria in the handled problems.

3.5 STUDY LIMITATION AND FUTURE PRESEPECTIVES

Our results have provided information on attenuation behavior of the electrical field of the 980nm photobiomodulation, delivered with a flattop beam profile device on the mitochondrion. However, within the limitation of our research that was carried out to provide information on the local EMF, we suggest further studies need to be conducted, to analyze further the EM field behavior and to increase further the knowledge on the PBM light attenuation on bone cells. An introduction of our simple one-dimensional model, for the first, would be the first stepping-stone for future EM experimental studies.

3.6 REFERENCES

1. Tearney GJ, Brezinski ME, Southern JF, Bouma BE, Hee MR, Fujimoto JG, Determination of the refractive index of highly scattering human tissue by optical coherence tomography. Opt. Lett.1995;20(21):2258-60.
2. Wilson BC, "Modeling and measurement of light propagation in tissue for diagnostic and therapeutic applications," Laser Syst. Photobiol. Photomed. 1991;252:13-27.
3. Baxter CD: Therapeutic lasers. Theory and practice. 1994. Churchill Livingstone)
4. Motamedi M, Rastegar S, Lecarpentier G, Welch AJ, "Light and temperature distribution in laser irradiated tissue: the influence of anisotropic scattering and refractive index," Appl. Opt.1989;28(12):2230-2237.
5. Chung H, Dai T, Sharma SK, Huang YY, Carroll JD, Hamblin MR. The nuts and bolts of low-level laser (light) therapy. Annals of Biomedical Engineering. 2012;40(2):516-533.
6. Posten W, Wrone DA, Dover JS, Arndt KA, Silapunt S, Alam M. Low-level laser therapy for wound healing: mechanism and efficacy. Dermatologic Surgery. 2005;31(3):334-40.
7. Zein R, Selting W, Hamblin MR. Review of light parameters and photobiomodulation efficacy: dive into complexity. Journal of biomedical optics. 2018;23(12):1-17.
8. M. A. Hadis, S. A. Zainal, M. J. Holder, J. D. Carroll, P. R. Cooper, M. R. Milward, and W. M. Palin. The dark art of light measurement: accurate radiometry for low-level light therapy. Lasers in Medical Science. 2016; 31(4):789-809.

9. de FreitasLF, M. R. Hamblin. Proposed mechanisms of photobiomodulation or low- level light therapy. IEEE Journal of Selected Topics in Quantum Electronics. 2016;22(3):348-64.
10. Karu TI. Mitochondrial signaling in mammalian cells activated by red and Near-IR radiation. Photochemistry and Photobiology. 2008;84(5):1091-1099.
11. Scheffler IE. Mitochondria. 2nd edition, New Jersey,USA:Wiley, Hoboken;2008.
12. Raven P, Johnson G, Mason K, Losos J, Duncan T. Biology. 12th edition New York, USA:McGraw-Hill;2017.
13. Amaroli A, Ravera S, Parker S, Panfoli I, Benedicenti A, Benedicenti S. 808- nm laser therapy with a flat-top handpiece photobiomodulates mitochondria activities of paramecium primaurelia (protozoa). Lasers in Medical Science. 2016; 31(4):741-47.
14. Danc´akov´a L, Vasilenko T, Kov´ac I, Jakubcov´a K, Holly´ M, Revajova´ V, Sabol F, Tomori Z, Iversen M, Ga´l P. Bjordal JM. Low-level lase therapy with 810 nm wavelength improves skin wound healing in rats with streptozotocin-induced diabetes. Photomedicine and Laser Surgery. 2014;32(4):198-204.
15. Erickson HP. Size and shape of protein molecules at the nanometer level determined by sedimentation, gel filtration, and electron microscopy. Biological procedures online. 2009;11:32-51.
16. Amaroli A, Ravera S, Parker S, Panfoli I, Benedicenti A, Benedicenti S. An 808-nm diode laser with a flat-top handpiece positively photobiomodulates mitochondria activities. Photomedicine and Laser Surgery. 2016; 34(11):1-8.
17. Fuma S, Murase H, Kuse Y, Tsuruma K, Shimazawa M, Hara H. Photobiomodulation with 670 nm light increased phagocytosis in human retinal pigment epithelial cells. Molecular vision. 2015;21:883-92.

18. Beauvoit B, Kitai T, Chance B. Contribution of the mitochondrial compartment to the optical properties of the rat liver: a theoretical and practical approach. Biophysical Journal. 1994; 67(6):2501-2510.
19. Ravera S, Panfoli I, Aluigi MG, Calzia D, Morelli A. Characterization of myelin sheath F_0F_1-ATP synthase and its regulation by IF_1. Cell Biochemistry and Biophysics. 2011;59(2):63-70.
20. Van Bladel JG. Electromagnetic Fields. 2nd edition. Piscataway, N.J.USA:IEEE Press; 2007.
21. Harrington RF. Time-Harmonic Electromagnetic Fields. New York:McGraw-Hill;1961.
22. Ullah H, Atif M, Firdous S, Mehmood MS, Ikram M, Kurachi C, Grecco C, Nicolodelli G. Bagnato VS. Femtosecond light distribution at skin and liver of rats: analysis for use in optical diagnostics. Laser Physics Letters.2010;7(12):889-898.
23. Morel A. Optical properties of pure water and pure seawater. Optical aspects of oceanography.1974;1(1):1-24.
24. Pegau WS, Gray D, Zaneveld JRV. Absorption and attenuation of visible and near- infrared light in water: dependence on temperature and salinity. Applied optics.1997;36(24):6035- 6046.
25. Poot M, Zhang YZ, Kr¨amer JA, Wells KS, Jones JL, Hanzel DK, Lugade AG, Singer VL, Haugland RP. Analysis of mitochondrial morphology and function with novel fixable fluorescent stains. Journal of Histochemistry & Cytochemistry.1996; 44(12):1363-1372.
26. Jacques SL. Optical properties of biological tissues: a review. Physics in Medicine and Biology 2013;58:R37–R61, 2013.

27. R. Thar and M. Ku¨hl. Propagation of electromagnetic radiation in mitochondria? Journal of Theoretical Biology. 2004;230:261-270.
28. Palmer KF and Williams D. Optical properties of water in the near infrared. Journal of the Optical Society of America. 1974 64(8):1107-1110..
29. Lentes FT, Clement MKT, Neuroth N, Hoffmann HJ, Hayden YT, Hayden JS, Kolberg U, Wolff S. The Properties of Optical Glass, chapter Optical Properties. Berlin; Springer:1998.
30. Doctor Smile wiser. User manual. LI8D0 001.7:UK; 2017